Design And Development Of An Autonomous Radar Receiver For The Detection Of Ultra High Energy Cosmic Rays

By

Samridha Kunwar

Submitted to the graduate degree program in Physics and Astronomy and the Graduate Faculty of the University of Kansas in partial fulfillment of the requirements for the degree of *Doctor of Philosophy*

(Chairperson) David Z. Besson

Christopher Allen

Philip S. Baringer

Douglas McKay

Daniel Tapia Takaki

Date Defended: 20th of February 2015

The Thesis Committee for **Samridha Kunwar**
certifies that this is the approved version of the following thesis:

Design And Development Of An Autonomous Radar Receiver For The Detection Of Ultra High Energy Cosmic Rays

Chairperson David Z. Besson

Date Approved: 23rd of March 2015

Abstract

The detection of ultra-high energy cosmic rays is constrained by their flux, requiring detectors with apertures of hundreds or even thousands of square kilometers and close to one hundred percent duty cycle. The sheer scale that would be required of conventional detectors, to acquire sufficient statistics for energy, composition or anisotropy studies, means that new techniques that reduce manpower and financial resources are continually being sought. In this dissertation, the development of a remote sensing technique based observatory known as bistatic radar, which aims to achieve extensive coverage of the Earth's surface, cf. Telescope Array's 700 km^2 surface detector, is discussed.

Construction of the radar projects transmitter station was completed in the summer of 2013, and remote receiver stations were deployed in June and November of 2014. These stations accomplish radar echo detection using an analog signal chain. Subject to less radio interference, the remote stations add stereoscopic measurement capabilities that theoretically allow unique determination of cosmic ray geometry and core location. An FPGA is used as a distributed data processing node within the project. The FPGA provides triggering logic for data sampled at 200 MSa/s, detecting Cosmic Ray shower echoes chirping at $-1\ to\ -10\ MHz/\mu s$ (depending on the geometry) for several μs. The data acquisition system with low power consumption at a cost that is also comparatively inexpensive is described herein.

I would like to dedicate this dissertation to my loving parents, Dr. Uttam and Sharada Kunwar.

Acknowledgements

And I would like to express my sincerest gratitude to my advisor Dave Besson. Dave, would have you believe that acknowledgements are unnecessary and gratuitous, and while perhaps true, I don't want to leave Kansas without thanking everyone for making graduate school such a wonderful experience. So thanks Dave, it has genuinely been a privilege working for you. Thinking about my time here, I don't think I would have rather been anywhere else despite the initial rough road towards my degree.

I'd also like to thank Ken Ratzlaff and Rob Young, without whom the project would have never gotten off the ground.

Also thanks to Jess and Mark Stockham, Steven Prochyra and Jordan Hanson for numerous insightful discussions but, more importantly for making working in Malott enjoyable, which I will remember with fondness years from now.

My brother Saket Kunwar also needs to be thanked, not just because he'd be angry if I didn't but, I am forever indebted to him for his inspiration and getting me started with my career. 'Dhanyabad Dai'.

Finally, I'd like to thank you the reader for taking the first steps towards enlightenment.

Contents

List of Figures

List of Tables

Glossary

Acronyms / Abbreviations

2MRS	2 Mass Redshift Survey
ADC	Analog-to-Digital Converter
AGN	Active Galactic Nuclei
BRAM	Block Random Access Memory
CAM	Chirp Acquisition Module
CCU	Chirp Calibration Unit
CMB	Cosmic Microwave Background
CMOS	Complementary metal–oxide–semiconductor
CORSIKA	COsmic Ray SImulation for KAskade
DCM	Digital Clock Manager
DDR	Double Data Rate
EAS	Extensive Air Shower
EFIE	Electric Field Integral Equation
FFT	Fast Fourier Transform
FIFO	First In First Out
FPGA	Field Programmable Gate Array
FSM	Finite State Machine

FSRQ	Flat Spectrum Radio Quasar
FWFT	First Word Fall Through
GPIO	General Purpose Input/Output
GPS	Global Positioning System
GRB	Gamma Ray Burst
GZK	Greisen, Kuzmin and Zatespin
HPBW	Half Power Beam Width
IBUFDS	Input BUFfer Differential Signaling
IVT	Current Voltage Temperature
LPDA	Log Periodic Dipole Antenna
LVDS	Low Voltage Differential Signaling
MARIACHI	Mixed Apparatus for Radar Investigation of Atmospheric Cosmic-rays of High Ionization
MOM	Method of Moments
NEC	Numerical Electromagnetics Code
NKG	Nashimura-Kamata-Greisen
PAO	Pierre Auger Observatory
PCM	Phase Change Memory
PLL	Phase Locked Loop
Pmod	Peripheral Module
PPS	Pulse Per Second
PV	Photo-Voltaic
QGSJET	Quark Gluon String with JET
RAM	Random Access Memory

RF	Radio Freqquency
SBC	Single Board Computer
SD	Surface Detector
SHA	Sample Hold Amplifier
SHM	System Health Monitor
SSOP	Small-Shrink-Outline-28-Package
SSR	Solid-State Relay
TA	Telescope Array
TARA	Telescope Array RAdar
TDA	Transient Detector Apparatus
UART	Universal Asynchronous Receiver/Transmitter
UHECR	Ultra-High Energy Cosmic Ray
VCV	Véron-Cetty and Véron
VHDC	Very High Density Cable
VSWR	Voltage Standing Wave Ratio

Chapter 1

Cosmic Rays

The Earth is continuously being struck by particles with kinetic energies ranging from a few MeVs to at least $3 \cdot 10^{20}$ eVs. Over the past several decades there has been a concerted effort in understanding their flux, their arrival energies, composition and origin in the celestial sphere. The answer to these questions along with correlations with known astronomical maps will solve one of the biggest mysteries of the 21st century in understanding the most violent processes in our universe.

The first discovery of cosmic ray particles is attributed to Victor Hess, a passionate balloonist, who undertook ten ascents (five at night) between 1911 and 1913. On these balloons, measurements were made using electroscopes. The potential drop as a function of time, measured approximately every hour, was converted into ion-pairs created in the gas of the electroscope per cubic centimeter per second [12]. Fig. 1.1 shows averaged measurements made from two detectors [13] on board the balloon Böhmen on the 7th of August, 1912.

This ascent was his seventh attempt, for which coal-gas used in previous attempts was replaced with hydrogen, enabling Hess to reach an altitude of 5350 m. At the time, conventional wisdom was that it was the Earth's radioactivity that was responsible for all the measured terrestrial radiation and, as a result, should decline with altitude. Hess's balloon experiments disproved this and demonstrated, that following an initial decrease, there is an increase in ionization as one ascends higher into the atmosphere. Additionally, following measurements on a separate ascent during a quasi-total solar eclipse on the 7th of April, 1912; Hess claimed that not only was the ionization extraterrestrial in nature, but also that the sun was not the only source.

Werner Kolhörster, a German Physicist, with modified temperature and pressure stable electroscopes verified Hess's results in 1914 and was successfully able to measure ionization at up to 9 km altitudes. A decade later, Millikan and Cameron in 1926, using special water resistant electroscopes

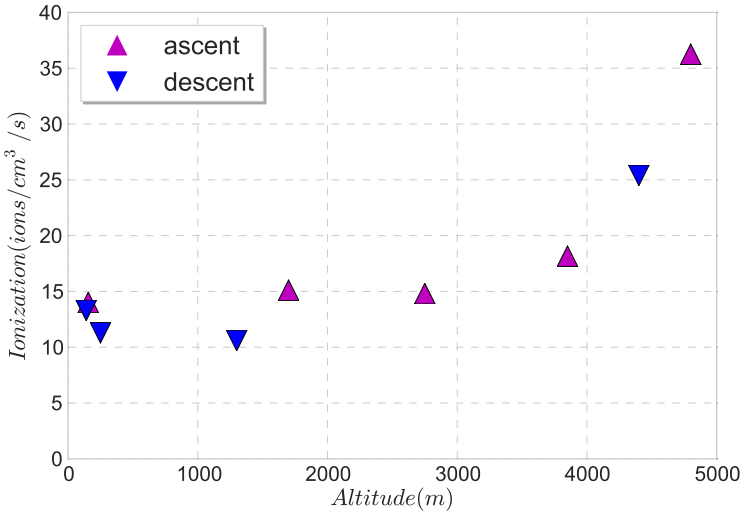

Fig. 1.1 Averages of Ionization measurements made by Hess on August 7th,1912.

made ionization measurements at Muir Lake (alt. 11,800 ft) and Arrowhead Lake (alt. 5,100 ft). They found that the ionization decreased steadily with depth in the water, and the difference in readings between the two lakes at different elevations were "the exact water equivalent of the absorption of the atmosphere" [14]. These results confirmed that the ionization was indeed extraterrestrial in nature and subsequently led to Millikan coining them as *Cosmic Rays*. Initially, these particles were believed to be $\gamma - rays$. However, by 1934, an East - West asymmetry observed in their arrival directions due to deflections caused by the Earth's magnetic field provided evidence that they are predominantly positively charged particles or nuclei.

1.1 Energy Spectrum

Primary cosmic rays - those accelerated at astrophysical sources, including protons, helium, iron and other nuclei synthesized in stars have an energy spectrum that has been studied by a variety of experiments. Fig. 1.2 summarizes these results.

Apart from those associated with solar flares, the flux of such cosmic rays, J(E), below $10^{10}eV$, are modulated by solar magnetic fields. These fields decelerate and partially deflect cosmic rays from the inner solar system. In addition, cosmic ray arrival intensities are also subject to geomagnetic fields.

At higher energies, the flux is non-thermal and follows a *broken power law* for about ten orders of magnitude,

$$J(E) = \frac{d^2\phi(E)}{dEd\Omega} \sim \left(\frac{E}{eV}\right)^{-\gamma} \tag{1.1}$$

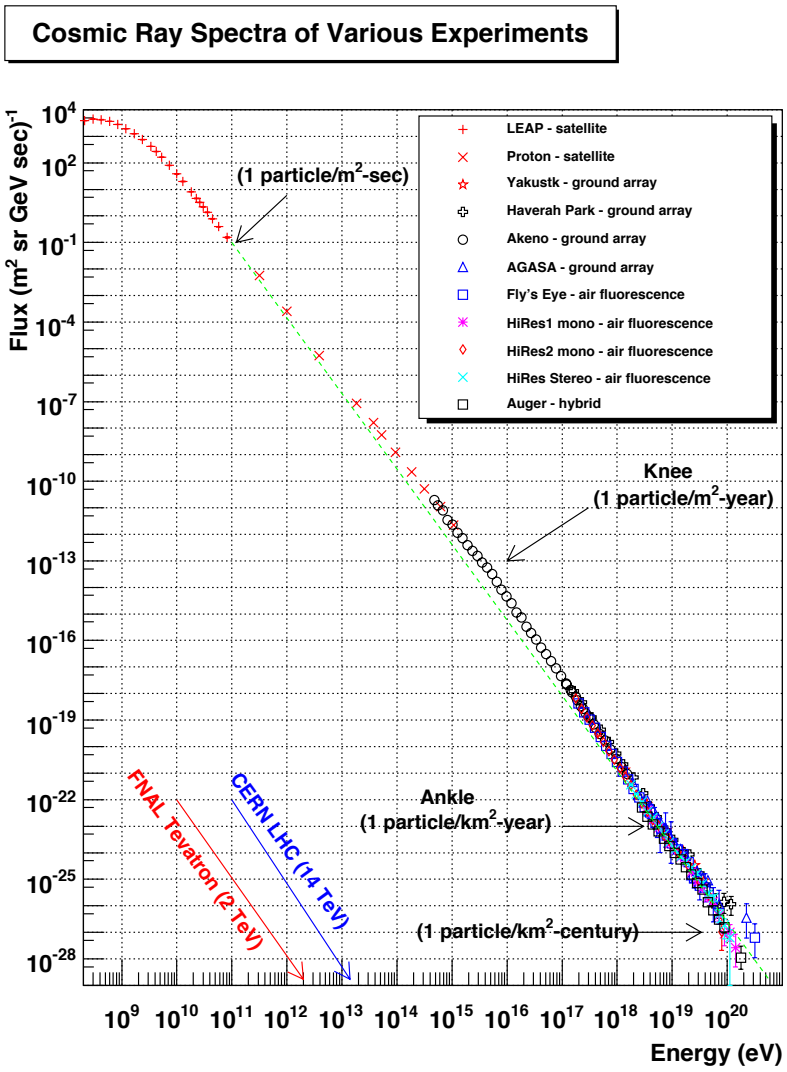

Fig. 1.2 Energy Spectrum from 10^8 to 10^{21} eV. Taken from [1].

where γ is the spectral index. There exist interesting features in this energy spectrum: at $\sim 10^{15.5}$ eV the spectral index changes from 2.7 to ~ 3 and is referred to as the *knee*, at $\sim 10^{18.5}$ eV the spectrum becomes harder again, with γ changing to ~ 2.6 (the *ankle*) and finally the flux steeply decreases above $3 \cdot 10^{19}$eV. The flux drops from 1 $particle/m^2 - year$ at the knee to 1 $particle/km^2 - year$ at the ankle and eventually to 1 $particle/km^2 - century$ towards the end of the observed spectrum.

The change in the spectral index, at the knee, is likely due to sources within the galaxy unable to accelerate cosmic rays to higher energies, cosmic rays escaping our galaxy during diffusive propagation processes or both. Equivalent to the latter, is that the galaxy confines cosmic rays with energies below

the knee and they are unable to leak out (the 'leaky box' model). [15] provides a detailed discussion on the origin of the knee in the cosmic-ray energy spectrum.

The cut-off at high energies can be explained by the interaction of primary cosmic rays with the remnant cosmic microwave background (CMB) radiation. If these cosmic rays are heavier nuclei, they can subsequently photo-disintegrate [16] or pair-produce resulting in an energy loss of the primary. For heavier nuclei like iron [17],

$$\begin{aligned} A + \gamma_{CMB} &\rightarrow (A-1) + N \\ &\rightarrow (A-2) + 2N \\ &\rightarrow A + e^+ + e^- \end{aligned} \tag{1.2}$$

results in a lower observed energy spectrum and lighter nuclei than at the source.

Fig. 1.3 shows possible interactions with the CMB.

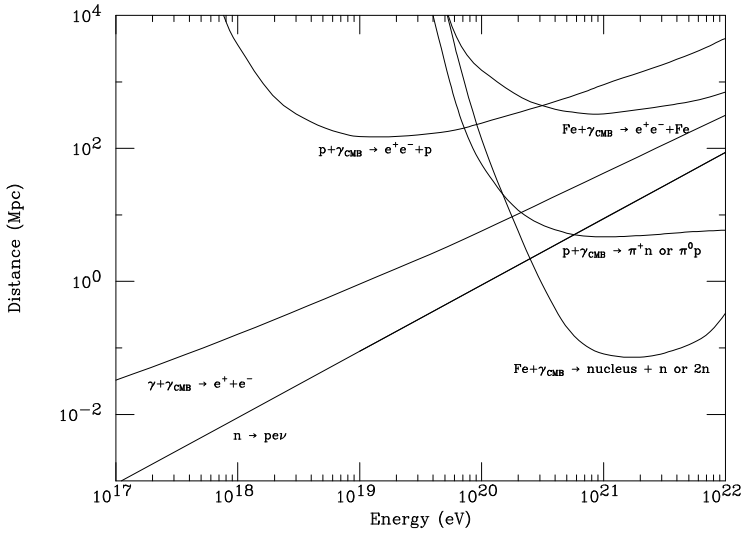

Fig. 1.3 Panorama of interactions of possible cosmic primaries with the CMB. Taken from [2]

For protons, the high energy cut-off of the spectrum was predicted independently by Greisen, Kuzmin and Zatespin in 1966 [18] [19] and is now known as the GZK limit . This limit primarily arises due to the interaction of protons with the cosmic microwave background, producing delta resonances that subsequently decay into nucleons and pions,

$$\begin{aligned} p + \gamma_{CMB} &\rightarrow \Delta^+(1232\,MeV) \rightarrow n + \pi^+ \\ &\rightarrow \Delta^+(1232\,MeV) \rightarrow p + \pi^0 \end{aligned} \tag{1.3}$$

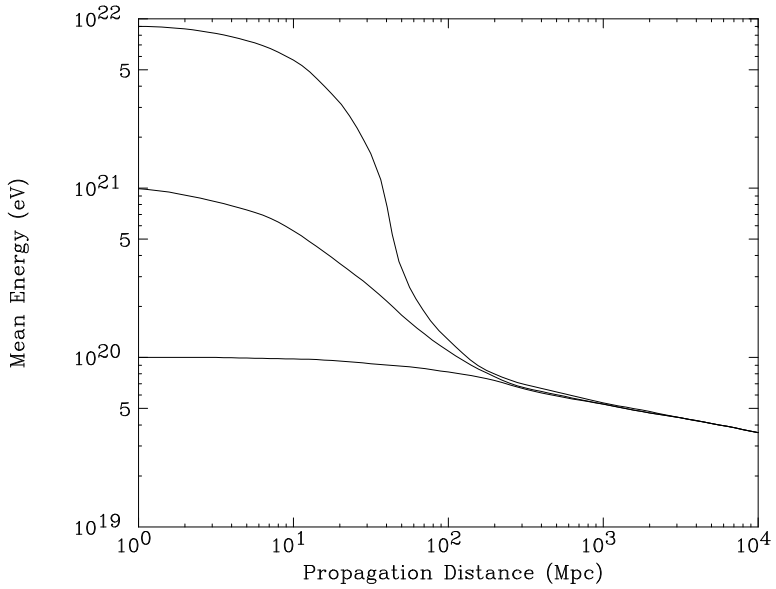

Fig. 1.4 Mean energy of protons as a function of propagation distance through the CMB. Curves are for energy at the source of 10^{22} eV, 10^{21} eV, and 10^{20} eV. Taken from [2]

For a temperature of $\sim 2.73K$, γ_{CMB} has number density $411cm^{-3}$, total energy density $0.26eVcm^{-3}$, and average energy $6.34\times10^{-4}eV$. Following the discussion in [20], the threshold energy for protons interacting with a photon to produce $\pi^{0,+}$ is $\sim 10^{20}eV$. Interactions at smaller energies by a factor of 3 or 4 are possible, as the microwave spectrum extends to higher energies (In addition to its higher-energy thermal tail, the microwave background increases with redshift due to the expansion of the Universe). Given the delta resonance cross-section of $\sim 5\times10^{-28}$ cm^2 and the γ_{CMB} number density, the ultra-high energy proton mean free path is ~ 8 Mpc [21]. Each time a photo-pion interaction occurs, the subsequent proton loses about 20% of its initial energy. Fig. 1.4 shows that after each interaction, as the proton continually loses energy to the microwave background, the energy of the proton eventually falls below the delta resonance threshold. As shown, for observation of trans-GZK protons, sources must be within ~ 100 Mpc (the GZK horizon).

Other interaction modes of cosmic protons with the cosmic microwave background are possible, including pair production,

$$p+\gamma_{CMB}\rightarrow p+e^{+}+e^{-} \tag{1.4}$$

which has a threshold of $E\sim 8\times10^{17}$ eV, and along with redshift propagation loss, is the primary energy loss mechanism for protons that fall below the delta resonance threshold. GZK attenuated protons produce a 'pile-up' while pair production and red shift propagation losses cause the steepening in the spectrum.

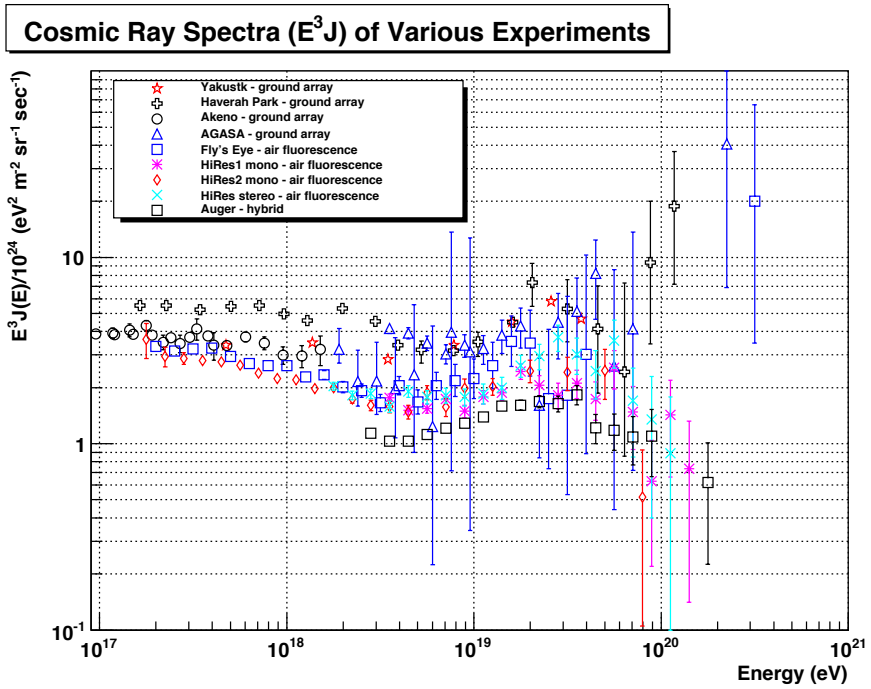

Fig. 1.5 Energy Spectrum from 10^{17} to 10^{21} eV. Taken from [1].

For iron nuclei dominated or mixed composition models, galactic-extragalactic transitions are likely responsible for the ankle to the left of the cosmic ray energy spectrum at an energy of approximately $10^{18.5}$ eV.

Fig. 1.5 shows the pileup and the ankle in the cosmic ray energy spectrum.

1.2 Anisotropies

One of the highest energy particles detected was the Oh-My-God (OMG) particle [22]. With an energy of $\sim 3.2 \pm 0.9 \times 10^{20}$ eV, the particle was detected in 1991 by the Fly's Eye Detector in western Utah. However, the source of such Ultra High Energy Cosmic Rays (UHECR) are still under discussion. It is widely accepted that local galactic sources are unlikely to be cosmic accelerators producing $> 10^{19}$ eV particles, as the galactic magnetic field would not be able to confine these particles. Observations also show that these cosmic rays have a relatively isotropic distribution and aren't concentrated in the galactic plane [5].

As the sources are likely to be extragalactic, deflections caused by galactic and intergalactic magnetic fields complicate obtaining directional information. The amount of deflection δ experienced by any charged particle of charge q and energy ε traveling through a magnetic field B for a distance L is

proportional to [23],

$$\delta \propto \frac{qBL}{\varepsilon}, \tag{1.5}$$

but, if such deflections are small, then it may be possible to determine the source location in the UHECR sky. [24] provides a more detailed discussion regarding mapping deflections of extragalactic UHECR's.

If trans-GZK protons and light nuclei like iron have powerful astrophysical sources, then due to the inhomogeneity of these sources within the GZK horizon in our local universe, they should have minimal deflections and are expected to exhibit an anisotropic arrival distribution. Therefore, it is of interest to correlate the UHECR sky with a catalog of known energetic sources.

The recent discussion regarding anisotropies in the UHECR sky began with the Pierre Auger Observatory (PAO) in 2007. They made correlations with the arrival directions of $> 55\ EeV$ events with the VCV(Véron-Cetty and Véron 2006) Catalog of Active Galactic Nuclei(AGN) [25]. Fig. 1.6 shows the "most likely value of the fraction of correlated events, plotted with black dots, as a function of the total number of time-ordered events (the events used in exploratory scans excluded)" [3]. Here $33 \pm 5\%$ of events are correlating cosmic rays, compared with 21% expected for an isotropic hypothesis. The most updated fraction of these correlating cosmic rays is $28.1^{+3.8\%}_{-3.6\%}$ for $> 53\ EeV$. The energy threshold was revised after accounting for "measurements of the fluorescence yield, a better estimate of the invisible energy, a deeper understanding of the detector, and an improved event reconstruction" [4] resulting in a modified correlation fraction.

Fig. 1.7 shows the Auger sky map with ten years of data from January 1st, 2004 to March 31st, 2014 for $\geqslant 52 EeV$ arrival directions. Here circles are drawn around all of the 2 Mass Redshift Survey (2MRS) objects within 90 Mpc. Each circle has radius 9°, which is the value for which the cross-correlation has maximum significance [4]. They reported no statistically significant evidence of correlation in UHECR distribution.

In 2014, the Telescope Array (TA) analyzed five years of Surface Detector (SD) data for cosmic rays with energies $> 57\ EeV$. Summing events over 20° radii circles [5] ("an angular scale comparable to the clustering length of AGN's within 85 Mpc" [26]), TA found deviations from isotropy, as shown in Fig. 1.8. There were, however, no clearly identifiable sources reported. The TA suggested that, if the hot spot is indeed real, then it could be due to the "closest galaxy group, galaxy filaments connecting us with the Virgo Cluster" or both [5]. Alternatively, "if cosmic rays are heavy nuclei, then they may have originated in the supergalactic plane containing the Ursa Major cluster and then been deflected by galactic and intergalactic fields" [5].

While both experiments suggest anisotropy in the distribution of UHECRs, more statistics are necessary for confirmation.

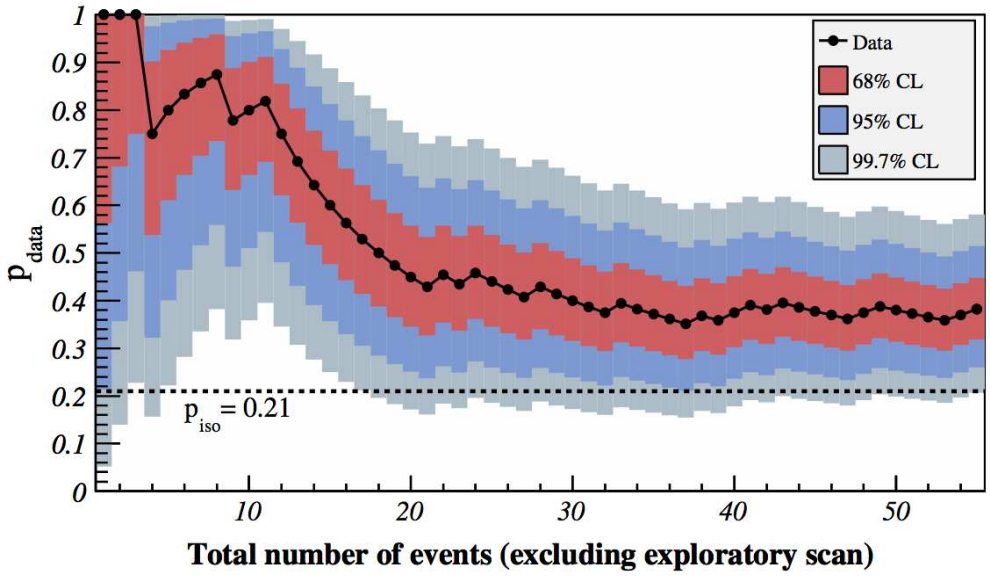

Fig. 1.6 Fraction of events correlating with AGNs as a function of the cumulative number of events by the Auger Observatory. The dotted line shows the expected correlating fraction for isotropic cosmic rays. Taken from [3].

1.3 Composition

In addition to the energy spectrum and anisotropy, the composition of cosmic rays is another important factor in identifying the origins of UHECR. The composition of cosmic rays with energy $\leq 10^{16} eV$ can be measured directly with space-based experiments [27] equipped with spectrometers and calorimeters. However, for higher energy cosmic rays, the small flux means that indirect detection techniques are necessary.

Indirect measurement of the composition of cosmic rays is achieved by measuring the depth of shower maximum (X_{max}) as the primary cosmic ray interacts with the atmosphere to produce secondary particles [17]. Sec. 2.1 provides a detailed discussion of proton-initiated Extensive Air Showers. While the penetration of the primary in the atmosphere increases with energy for all nuclei, heavy vs. light nuclei also vary in penetration, and it is this characteristic that enables composition measurements. In addition, fluctuations in X_{max} and the number of secondary muons may be used in the determination of the primary's composition. These indirect measurements, rather than on an event-by-event basis, are done statistically by a comparison of measured and simulated distributions [28].

Shower observations suggest light primaries dominate at the knee and change to heavier primaries up to $\sim 10^{17}$ eV [27]. A reversal follows with lighter nuclei up to $\sim 10^{18} eV$. The PAO finds that

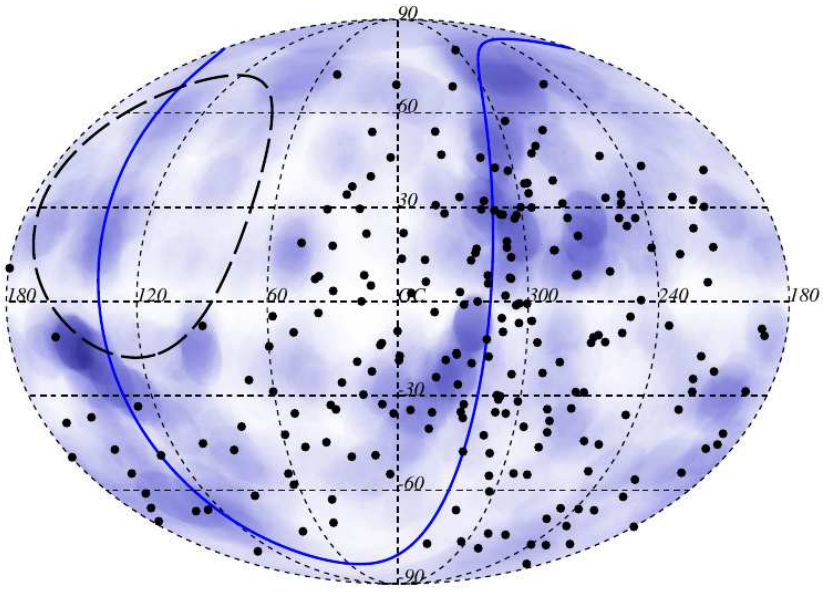

Fig. 1.7 Pierre Auger Observatory sky map plotted using 9° radius-circles drawn around known 2MRS objects within 90 Mpc. The dashed line is the field-of-view limit for the Auger Observatory (for $\theta \leq 80^{\circ}$) and the blue solid line corresponds to the Super-Galactic Plane. Taken from [4].

the spectrum is dominated by light nuclei from $10^{18} eV$ to $10^{18.5} eV$ [29] after which a heavier nuclear component becomes significant [30]. By contrast, the TA can explain their data over this entire energy range without a heavy nuclear admixture [31], leading to a discrepancy in these energy regimes between the two observatories.

1.4 Candidate Sources

While the source of such *UHECRs* has not been pinpointed, there are various candidate sources that are best described by the Hillas plot in Fig. 1.9, that may provide a window into understanding the most violent processes in the universe. In this Figure, the sources above the top (red) line indicate those sources that can accelerate protons to energies up to 10^{21} eV, while those above the bottom (green) line can accelerate heavier iron nuclei up to 10^{20} eV.

The Hillas criterion upon which Fig. 1.9 is based places a limit on the maximum energy of a particle of electric charge q, leaving the source with magnetic field B and radius R_s:

$$\varepsilon_{max} = qBR_s \tag{1.6}$$

This constraint is obtained by demanding that the Larmor radius [6], $R_L = \varepsilon/qB$ is contained within

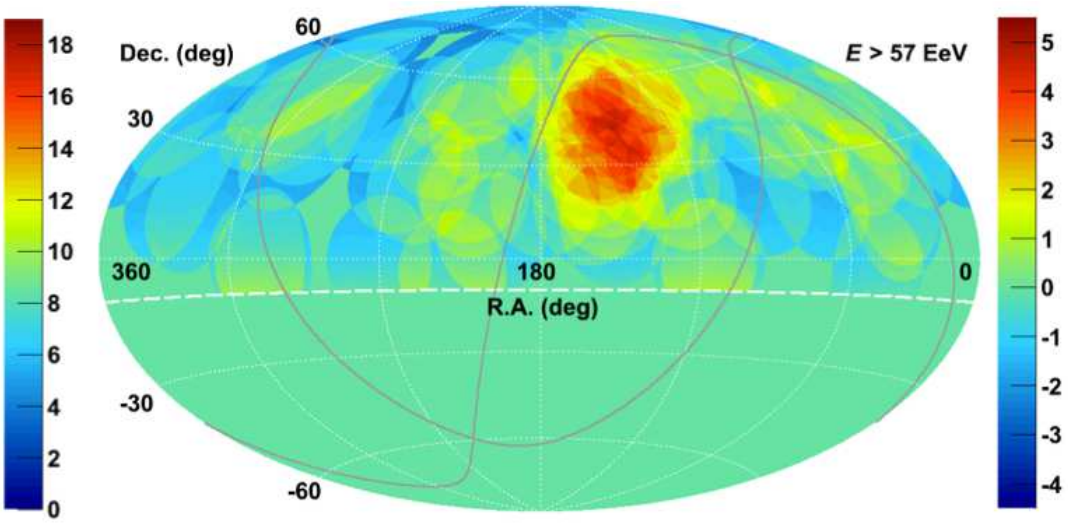

Fig. 1.8 Telescope Array significance map plotted using 20° radius-circles. Both the significance of the hotspot, as well as the number of events observed, are indicated by the color coding. Taken from [5].

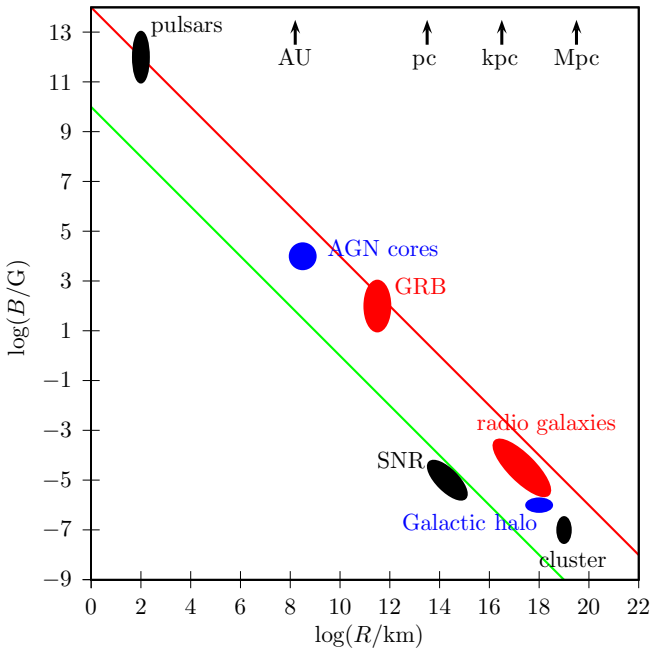

Fig. 1.9 Hillas Plot. Sources above the top (red) line can accelerate protons up to 10^{21} *eV* and sources above the bottom (green) can accelerate iron up to 10^{20} *eV*. Taken from [6].

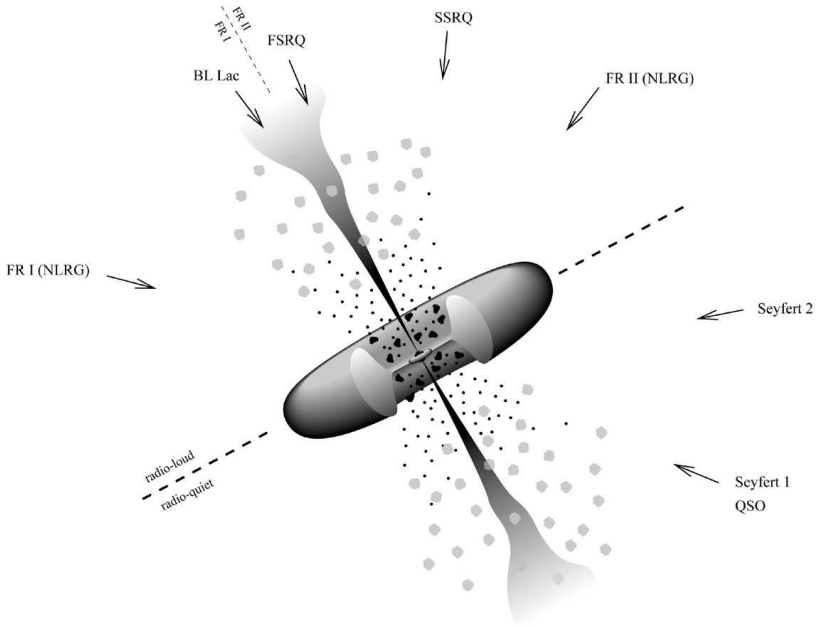

Fig. 1.10 Unified scheme of AGN. Taken from [6].

the accelerator of size R_s [6],

$$R_L = \varepsilon/qB \leq R_s \tag{1.7}$$

Conceptually, to produce the highest energy particles, small accelerators will need to have large magnetic fields to trap charged particles in the acceleration region or, vice-versa, a cosmic accelerator with a small magnetic field requires an immense acceleration region of the order of Mpc.

Possible candidates for UHECR origin include (a) Gravitational Accretion Shocks where dark matter accretion can cause shocks around large-scale structures in the Universe, (b) Gamma Ray Bursts (GRB) where multiple shock regions can form potential zones of acceleration, (c) Neutron Stars that have extremely strong dipole fields of order $10^{-15}G$ [27] and finally, the most discussed source: (d) Active Galactic Nuclei (AGN).

Active Galaxies have a total luminosity exceeding the thermal emission of the individual stars comprising the galaxy due to accretion of supermassive black holes located at their center. The type of AGN observed is dependent on the observing angle, stage of activity and evolution in time [6], as shown in Fig. 1.10. Amongst these AGN's, Blazars have relativistic jets pointing towards Earth and are considered strong candidates as UHECR sources [32]. These Blazars are either Fanaroff-Riley I galaxies and their associated BL Lac objects or Fanaroff-Riley II galaxies and their associated Flat Spectrum Radio Quasars (FSRQ) .

Understanding the energy, composition and anisotropy of cosmic rays will provide answers to some

of the most intriguing questions in our Universe. The next chapter discusses physics of cosmic ray interactions and their detection using a novel radar technique.

Chapter 2

Radar Detection of Cosmic Rays

In this chapter, we discuss the properties of Extensive Air Showers (EAS) and the technique of detection by radio interrogation.

2.1 Extensive Air Showers (EAS)

Cosmic rays with energies per nucleon in excess of 10^{14} eV [33] create cascades of particles with electromagnetic and hadronic components in the atmosphere, known as Extensive Air Showers (EAS). The development of the shower can be defined by the first interaction in the atmosphere. The interaction of a primary proton with an absorber nucleus A can be represented as,

$$p + A \rightarrow p + X + \pi^{0,\pm} + K^{0,\pm}, \tag{2.1}$$

where X is the fragmented nucleus. Several particles such as K, Λ, η, ... are produced. However, the pions carry away roughly half of the energy (dependent on interaction elasticity) and the remainder by the remnant cosmic ray, which continues to interact. The entire shower development can then be described in terms of the behavior of the pions produced in the first few interactions.

Neutral pions (π^0) with a rest lifetime of $\sim 10^{-16}$s have the decay modes,

$$\pi^0 \rightarrow \gamma\gamma,\ \pi^0 \rightarrow \gamma e^+ e^-,\ and\ \pi^0 \rightarrow e^+ e^- e^+ e^-, \tag{2.2}$$

where the two-photon mode dominates. These photons go on to produce e^+e^- pairs that then emit bremsstrahlung photons after traveling some distance. When

$$-\frac{dE}{dx}|_{bremsstrahlung} = -\frac{dE}{dx}|_{ionization}, \tag{2.3}$$

the electron is said to be at its critical energy ($\sim 84\ MeV$ in air) and the shower evolution at that point described as the shower maximum.

Primary cosmic ray energy affects the decay time and interaction length of the secondary charged pions ($\pi^{\pm}$). These pions can interact to initiate subsequent pion showers or can decay to produce muons through their most common decay mode,

$$\pi^+ \rightarrow \mu^+ + \nu_\mu \ and \ \pi^- \rightarrow \mu^- + \bar{\nu_\mu} \tag{2.4}$$

2.1.1 Longitudinal Shower Development

The Gaiser-Hillas functional form [34] has proven to be useful in fitting the measured and simulated air shower development with various hadronic models like QGSJET (Quark Gluon String with JET) and QGSJETII [35]. The form is given by,

$$N(X) = N_{max}(\frac{X - X_0}{X_{max} - X_0})^{\frac{X_{max}-X_0}{\lambda}} e^{\frac{X_0 - X}{\lambda}}, \tag{2.5}$$

where N_{max} is the maximum number of charged particles, X_{max} is the atmospheric depth where the maximum occurs, X_0 is the atmospheric depth of the first interaction and λ is a fit parameter.

The cascade of these secondary particles produced in the atmosphere have been investigated using Monte Carlo Simulations such as CORSIKA 6.50 (COsmic Ray SImulation for KAskade) [36] with the QGSJET II hadronic interaction subroutine.

Figs. 2.1 and Fig. 2.2 show CORSIKA simulation of the longitudinal distribution of the number of charged particles and energy deposition, respectively. Shown is a $\sim 10^{18} eV$ proton-initiated shower at a zenith angle of $60.4 \pm 0.3^{\circ}$, using a realistic curved Earth surface model. Shower maximum is at $\sim 400 g/cm^2$.

Fig. 2.3 shows a comparison of the number of shower electrons for showers initiated by $10^{18} eV$, $10^{19} eV$, and $10^{20} eV$ cosmic ray protons at different shower depths.

Several hundred simulations were run for proton energies $10^{18} \leq E \leq 10^{20.5}$, showing the relationship between depth at shower maximum and zenith angle of the arriving primary proton. The number of electrons produced at shower max does not vary significantly with the incoming angle of the primary proton (see Fig. 2.4).

2.1.2 Lateral Shower Development

As the secondary particles have transverse momentum with respect to the shower axis, the lateral shower profile for the electromagnetic particles is approximated by the Nishimura-Kamata-Greisen (NKG)

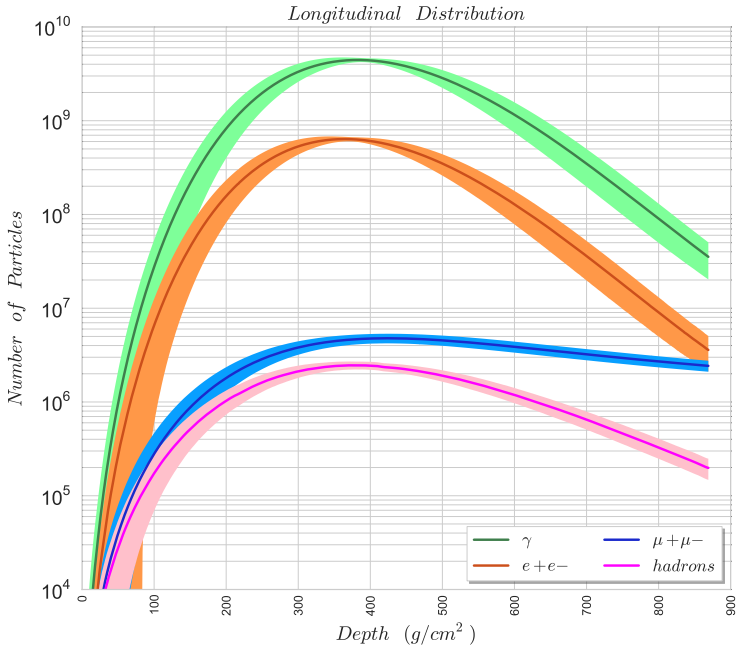

Fig. 2.1 Longitudinal Distribution of particles in a $\sim 10^{18} eV$ proton-initiated shower with an incoming zenith angle of $60.4 \pm 0.3^{\circ}$ in 870 Vertical Steps of $1 g/cm^2$.

function,

$$\rho(r) = \frac{N(s)}{{r_m}^2 {s_m}^2} \frac{(r/r_m s_m)^{s-2}(1+r/r_m s_m)^{s-4.5}}{2\pi\beta(s, 4.5-2s)} \tag{2.6}$$

where $\rho(r)$ is the charged particle density at a distance r to the shower axis in particles per unit area, and N(s) is the total number of charged particles at shower age s ($s = \frac{3}{1+2X_{max}/X}$ such that s = 1 at X_{max}).

The Moliere radius is given by

$$r_m = 70(\frac{\rho_0}{\rho})\, m, \tag{2.7}$$

where ρ is the density of the air at the altitude under consideration, and ρ_0 is the density at sea level.

Fig. 2.5 shows the lateral distribution of electrons at various primary energies incident at $\sim 60^{\circ}$. It is essential to note that these are shower electrons as opposed to ionization electrons that contribute to the plasma frequency discussed in the next section.

2.2 EAS Plasma

Electrons and ions close to the shower core form a plasma that on average can be assumed to be electrically neutral. Such a plasma has excitation modes that are longitudinal or transverse. We now discuss

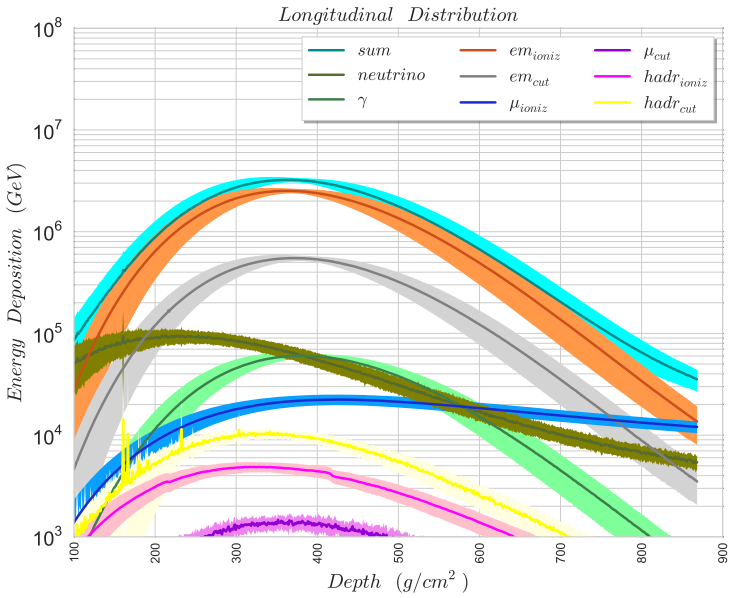

Fig. 2.2 Longitudinal Distribution of the energy content in different particle species for a $\sim 10^{18} eV$ proton-initiated shower with an incoming zenith angle of $60.4 \pm 0.3^{\circ}$ in 870 Vertical Steps of $1 g/cm^2$.

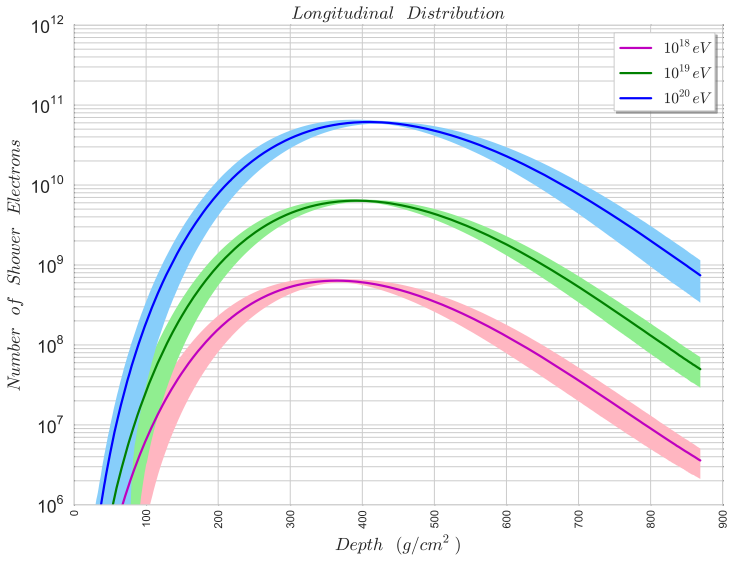

Fig. 2.3 Number of shower electrons at varying depth. Blue: $\sim 10^{20}$eV, Green: $\sim 10^{19}$eV and Magenta: $\sim 10^{18}$eV primaries. All Zenith angles are $\sim 60.4 \pm 0.3^{\circ}$.

the formation and excitation of the plasma. In the discussion that follows, the mass of protons is as-

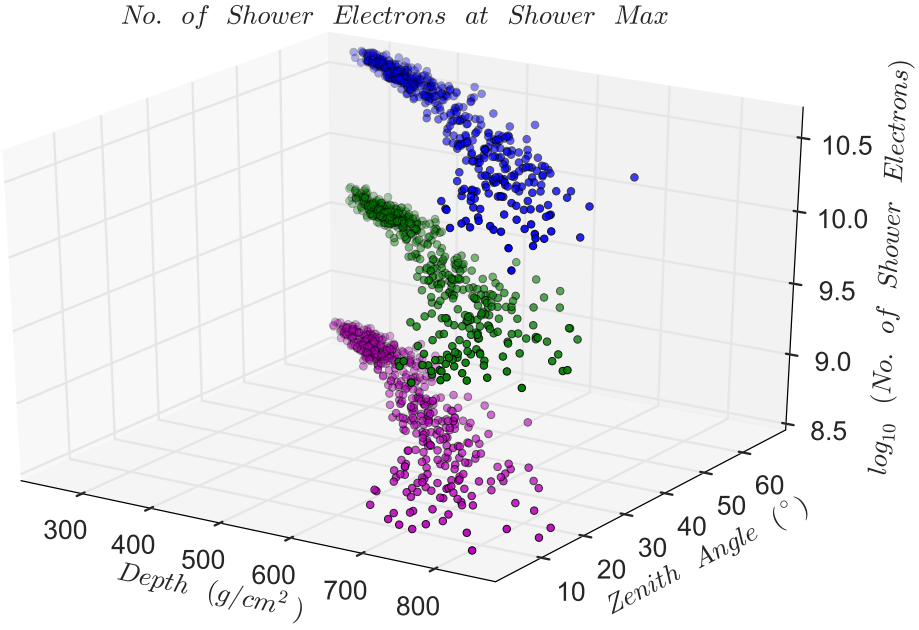

Fig. 2.4 Number of shower electrons at Shower Max at varying energies and zenith angle. Blue: $\sim 10^{20}$eV, Green: $\sim 10^{19}$eV and Magenta: $\sim 10^{18}$ eV primaries.

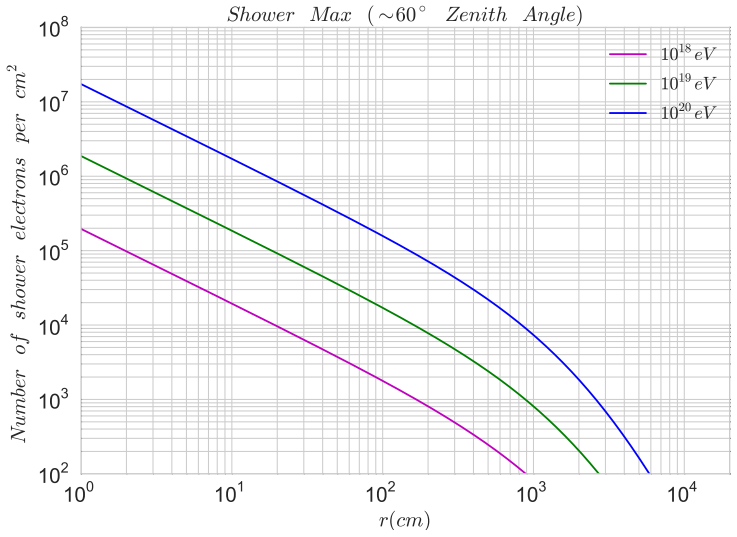

Fig. 2.5 Lateral Distribution of shower electrons for primary proton-initiated shower of 10^{18}, 10^{19} and 10^{20} eV incident at $\sim 60°$.

sumed to be infinite compared to that of electrons.

2.2.1 Plasma Frequency

Conceptually, if atomic electrons are displaced by some distance Δx, as shown in Fig. 2.6, regions of positive and negative charge due to the ions and electrons are, respectively, created.

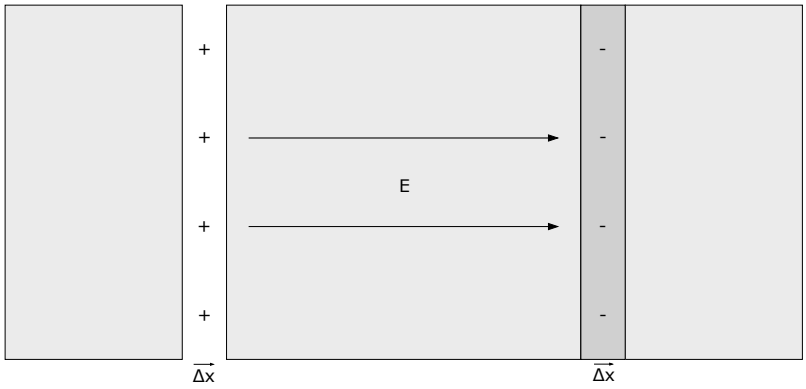

Fig. 2.6 Longitudinal oscillations in a plasma.

The longitudinal electric field in this intervening region is

$$E = -\frac{n_e e \Delta x}{\varepsilon_0}, \tag{2.8}$$

and the force restoring the electrons to their original position is then,

$$F = eE = -\frac{n_e e^2 \Delta x}{\varepsilon_0} = m_e \frac{d^2 \Delta x}{dt^2}, \tag{2.9}$$

which is the equation of a simple harmonic oscillator such that the electrons oscillate coherently in the longitudinal direction with the frequency,

$$\omega^2{}_p = \frac{n_e e^2}{\varepsilon_0 m_e} \tag{2.10}$$

Additionally, as the transverse fields are translationally invariant, the transverse canonical momentum of a particle in the field is conserved such that we have the dispersion relation [37],

$$\omega^2 - k^2 c^2 = \omega^2{}_p \tag{2.11}$$

where k is the propagation constant.

For a wave with a frequency above the plasma frequency ($\omega > \omega_p$), the propagation constant k is real. The wave propagates through the plasma with a phase velocity, $v_\phi = \omega/k > c$, as shown in Fig. 2.7. The individual electrons scatter independently according to the Thompson cross-section,

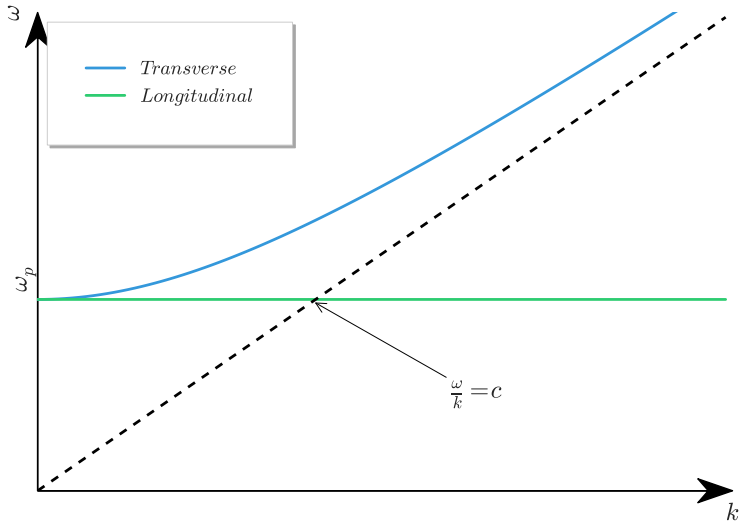

Fig. 2.7 Dispersion relation for waves in a plasma.

$$\sigma_T = \frac{8\pi}{3}\left(\frac{e^2}{m_e c^2}\right)^2 = 6.69 \times 10^{-29}\ m^2, \tag{2.12}$$

When $\omega < \omega_p$, the propagation constant is imaginary (i.e., $k < 0$), and the wave is evanescent with no energy transmitted through the plasma. The plasma rather reflects the wave.

Fig. 2.8 shows the plasma frequency at various primary energies incident at $\sim 60^\circ$ as determined from CORSIKA simulations. Ionization electrons are calculated by measuring the ratio of the energy deposited in the atmosphere and the mean energy per ion pair production of 33.8 eV [38].

Fig. 2.9 shows the plasma frequency for a $10^{19} eV$ primary incident at different zenith angles and various radii at shower maximum.

2.2.2 Plasma Lifetime

Various factors contribute to the lifetime of plasmas, such as diffusion through the ambient air, attachment, and recombination of electrons [39].

At lower EAS shower max altitudes, the ambipolar diffusion constant D_i is given by,

$$D_i \propto T_i \nu_i^{-1}, \tag{2.13}$$

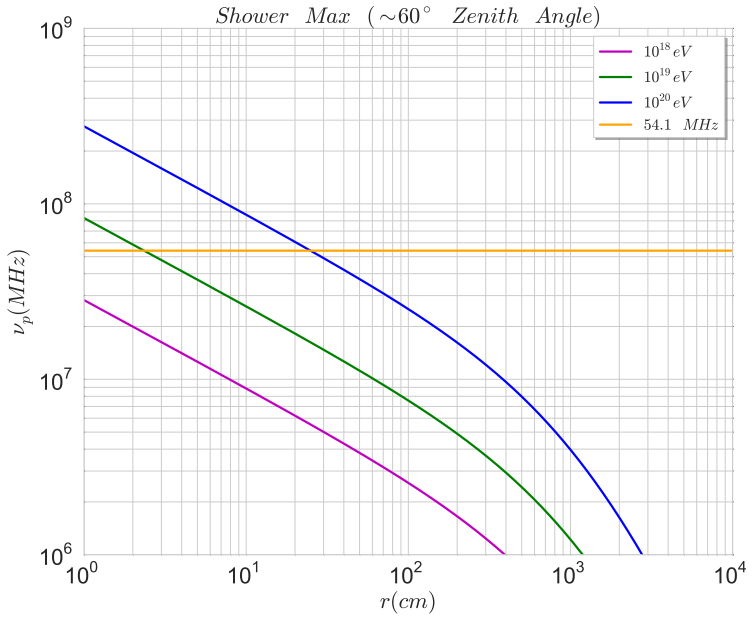

Fig. 2.8 Plasma Frequency for primary proton initiated shower of 10^{18}, 10^{19} and 10^{20} eV incident at $\sim 60^{\circ}$. Also shown is a 54.1 MHz reference line, corresponding to our experimental sounding frequency.

where T_i, ν_i are the kinetic temperature and collisional frequency, respectively. The ambipolar constant has been found to be $\sim 5\ cm^2 s^{-1}$ [39] at EAS altitudes due to higher collisional frequency as compared to meteor shower altitudes at $\sim 80\ to\ 120\ km$. Assuming that the diffusion of EAS showers are similar to that of meteor ionization, where for the underdense regime, the power decays exponentially with a time constant, $\tau_m = \lambda^2/32\pi^2 D_i$, then diffusion alone would lead to a lifetime of $\simeq 200\ s$ for a frequency of 54 MHz. Additionally, it has also been shown that for plasmas due to lightning strikes, (which have higher ionization densities by several orders of magnitude than EAS) at $\sim 10\ km$ and 11 cm wavelength the time constant is 240 ms. For these reasons, diffusion is expected to have minimal effect on the lifetime of EAS plasmas. Similarly, recombination times of electrons and ions in the troposphere are expected to be several minutes [39] [40] and so likely even less significant than diffusion.

Attachment is the primary factor affecting EAS plasma lifetime [41]. These processes are

Two Body Attachment:

$$e^- + O_2 \rightarrow O^- + O, \tag{2.14}$$

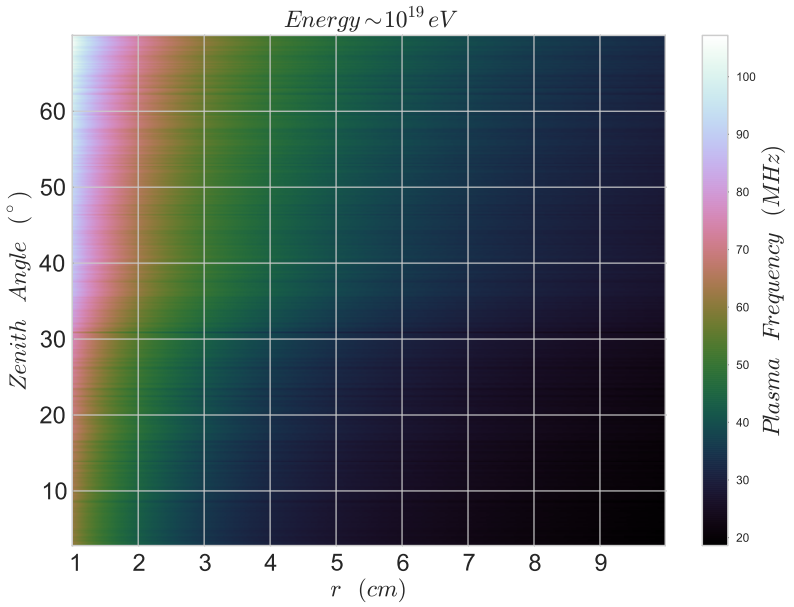

Fig. 2.9 Plasma frequency for a $10^{19} eV$ primary proton-initiated shower at various zenith angles and radii at shower maximum.

Three Body Attachment:

$$\begin{aligned} e^- + O_2 &\rightleftharpoons O_2^{-*}, \\ O_2^{-*} + O_2 &\rightarrow O_2^- + O_2 + energy. \end{aligned} \tag{2.15}$$

At low altitudes, the three-body attachment dominates the de-ionization process [40] due to its quadrature dependence on oxygen concentration. At higher altitudes, as the concentration of oxygen diminishes, two-body attachment becomes more important in the de-ionization process. For calculating the plasma lifetime at EAS altitudes, three-body attachment is the most significant process.

The three-body attachment rate is dependent on the particle density of the atmospheric elements involved and given by [42],

$$\frac{\partial N_e}{\partial t} = -k_{att1} N_e N_m^2 [O_2]^2 - k_{att2} N_e N_m^2 [O_2][N_2], \tag{2.16}$$

where N_e is the electron number density, N_m is the total number density of atmospheric molecules (Nitrogen, Oxygen, Carbon-Dioxide and trace gases), $[O_2]$ is the fraction of Oxygen and $[N_2]$ the fraction of Nitrogen in the atmosphere. These parameters are, $[O_2] = 0.209476$, $[N_2] = 0.78084$, $k_{att1} = 2 \cdot 10^{-30} cm^6 s^{-1}$, and $k_{att2} = 8 \cdot 10^{-32} cm^6 s^{-1}$.

The lifetime of a plasma at sea level is found to be $\sim 15\ ns$ and at 10 km to be $\sim 130\ ns$ [42] as

shown in Fig. 2.10.

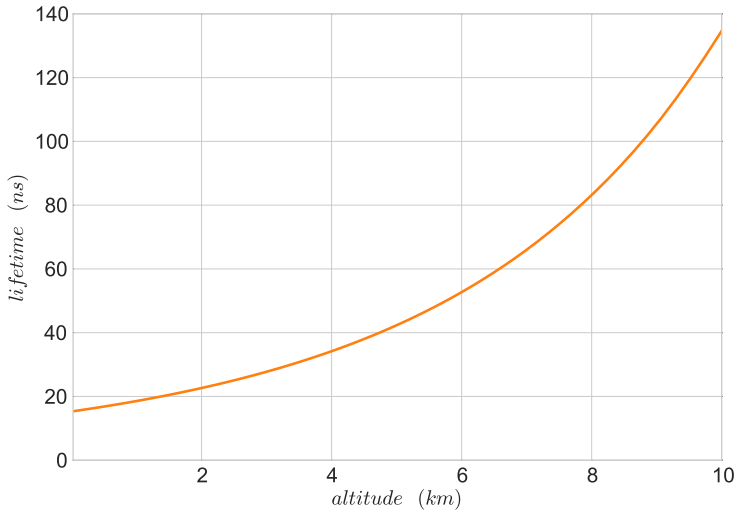

Fig. 2.10 The lifetime of plasma in the atmosphere at standard temperature and pressure due to the attachment process discussed in the text.

2.3 Radar Detection

2.3.1 Radar Detection of Ionization Trails

The development of the ionization trail induced by cosmic rays is believed to be analogous to that of micro-meteors that form similar ionization columns. As meteoroids penetrate the Earth's atmosphere, gradual ablation results in a cylindrically ionized channel along their path. Radar detection of these meteor plasma columns have been observed for trails between altitudes of 70 and 120 km, with most observed between 80 and 105 km [43].

Typically the smallest detectable meteors have a mass of $10^{-6}g$ and dimensions of 10^{-3} *to* $10^{-2}m$. At typical velocities of $\sim 4-5\cdot 10^{4}m/s$, they have kinetic energy of $\sim 1J$, most of which is dissipated to ionization. However, as discussed earlier, in an EAS, the lateral distribution of particles spreads out as the shower progresses and propagates at relativistic speeds. Subsequently, air showers result in an ionization column with a different initial distribution than that of a meteor.

In 1941, Blackett and Lovell [44] were the first to propose cosmic rays as an explanation of anomalies observed in atmospheric radar data. They suggested a point cluster approximation, with n ions

within a Fresnel length, L_f, of the ionized column,

$$L_f = \sqrt{\lambda R}, \tag{2.17}$$

where λ is the transmitter wavelength and R the distance from the transmitter to the ionized column. In this approximation, the maximum electronic ions per cm is,

$$n = \frac{1}{2} 10^{-7} pE \tag{2.18}$$

where E is the incident energy and p the pressure in atmospheric units. Consequently, in an equivalent point cluster, the total number of electrons is given by,

$$N = nL_f = \frac{1}{2} 10^{-7} pE\sqrt{\lambda R} \tag{2.19}$$

They suggested that via their model, reflections observed at altitudes as low as 10 km for $E \geq 10^{15} eV$ were possibly from such cosmic ray ionization trails. However, no definitive observations were ever reported.

In later discussions, it was suggested that the point cluster method would not lead to coherent scattering due to the spread of shower electrons in the cascade process. In addition, and more importantly attenuation is caused by the scattering of the oscillating electrons from neutral molecules that interfere with the coherence oscillation of the plasma. This decrease in scattered energy is given by [45] and claimed to reduce the detectable cosmic ray energy by as much as 30 dB [38],

$$\frac{1}{1 + (\frac{\nu_c}{\pi \nu_0})^2}, \tag{2.20}$$

where ν_c is the collision frequency and ν_0 the plasma frequency.

It has now been shown that the low-energy threshold initially suggested by Blackett and Lovell is unlikely, and an energy threshold of $E \sim 10^{19} eV$ is more realistic.

While dampening can cause substantial signal attenuation, its effect may be mitigated by using a bistatic configuration (see Fig. 2.11). In this case, the radar cross-section (RCS) is of order $4\pi A^2/\lambda^2$ higher than that of the monostatic radar [38]. Here λ is the electromagnetic wave wavelength, and A is the target objects cross-sectional area.

While the radar cross section, σ_{EAS} is unknown, the bistatic radar equation yields,

$$\frac{P_R}{P_T} = \frac{G_T}{4\pi R_T^2} \sigma_{EAS} \frac{G_R}{4\pi R_R^2} \frac{\lambda^2}{4\pi}, \tag{2.21}$$

where P_T and P_R are the transmitted and received power, G_T and G_R the transmitter and receiver antenna

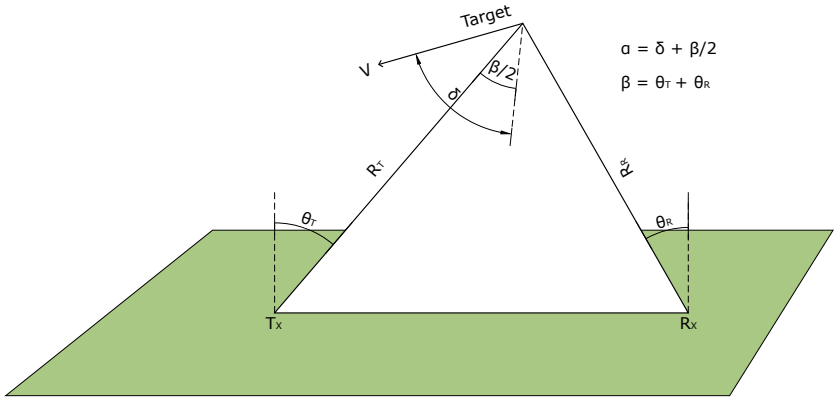

Fig. 2.11 Bi - static Radar Configuration.

gains, R_T and R_R the distance to the ionization trail from the transmitter and receiver respectively, λ the wavelength of the transmitted signal and σ the radar cross-section (RCS).

As the over-dense regime is likely to be the most significant contributor for radio reflection of EAS, and since $r_c << \lambda$ (Rayleigh regime), where λ is the radar wavelength, the shower can be approximated as a 'thin wire', where the RCS is given by,

$$\sigma_{EAS} = \frac{\pi L^2 sin^2\theta [\frac{sin(\frac{2\pi L}{\lambda} cos\theta)}{\frac{2\pi L}{\lambda} cos}]^2}{(\frac{\pi}{2})^2 + (ln\frac{\lambda}{\gamma\pi r_c sin\theta})^2} cos^4\phi \tag{2.22}$$

with L the length of the wire, r_c the radius of the wire, $\gamma = 1.78$, θ the angle between the wire and the direction of incidence, and ϕ the angle between the polarization direction and the plane defined by the wire and the direction of incidence [46].

Fig. 2.12 shows the RCS for 10^{19} and 10^{20} eV showers at varying zenith angles and a constant θ = 45° assuming a vertically polarized incident signal, as calculated using CORSIKA simulations.

In addition, at the receiver, the noise power is given by $P_N = K_B T_s B$, where K_B is Boltzmann's constant, T_s the system noise temperature and B is the noise bandwidth. The received signal-to-noise ratio at the receiver is then,

$$S/N = \frac{k}{R_R^2 R_T^2} \tag{2.23}$$

where,

$$k = \frac{P_T G_T \sigma_{EAS} G_R \lambda^2}{(4\pi)^3 K_B T_s B} \tag{2.24}$$

Assuming, P_T = 40 KW, G_T = 22 dBi, G_R = 12 dBi , λ = 5.545 m, σ_{EAS} = 400 cm^2 , B = 24 MHz, T_s = 300 K and taking the separation between the Transmitter and Receiver to be 40 km, Fig. 2.13 shows

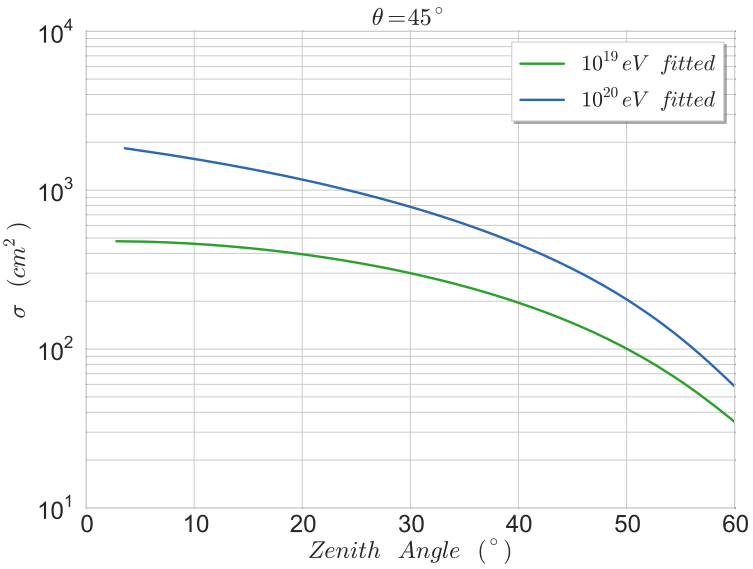

Fig. 2.12 RCS for 10^{19} and 10^{20} eV showers at varying zenith angles and a constant $\theta = 45°$.

the isocontour lines for the signal-to-noise ratio in the bi-static plane in this particularly optimistic case without considering attenuation due to collisional dampening. Here the cross-section refers to a physical cross-section of $\sim 2\ cm \times 200\ cm$, or roughly the dimensions of the over-dense regime. The effective area is limited by the beamwidth of the transmitter and receiver antennas.

This bi-static configuration results in a Doppler shift,

$$f = \frac{1}{\lambda}\frac{d}{dt}[R_T + R_R] \tag{2.25}$$

where R_T and R_R are the line of sight from the transmitter and receiver to the target respectively and λ the wavelength of the transmitted signal. While the target moves near the speed of light, the distances R_T and R_R evolve slowly over time.

This can be expressed as,

$$f = 2 f_0 cos\delta cos\beta/2 \tag{2.26}$$

where f_0 is the frequency of the transmitted signal, β the bistatic angle and δ the angle between the direction along which the target is moving and the bisector of the bistatic angle.

As the transmitting frequency is constant and since the path lengths are time-dependent the received signal is a Doppler like signal (chirp). The rate of change in frequency (chirp rate) is subsequently given by,

$$\kappa = \frac{\partial f}{\partial t} = -f_0 c[\frac{1}{R_T} + \frac{1}{R_R}]sin\alpha \tag{2.27}$$

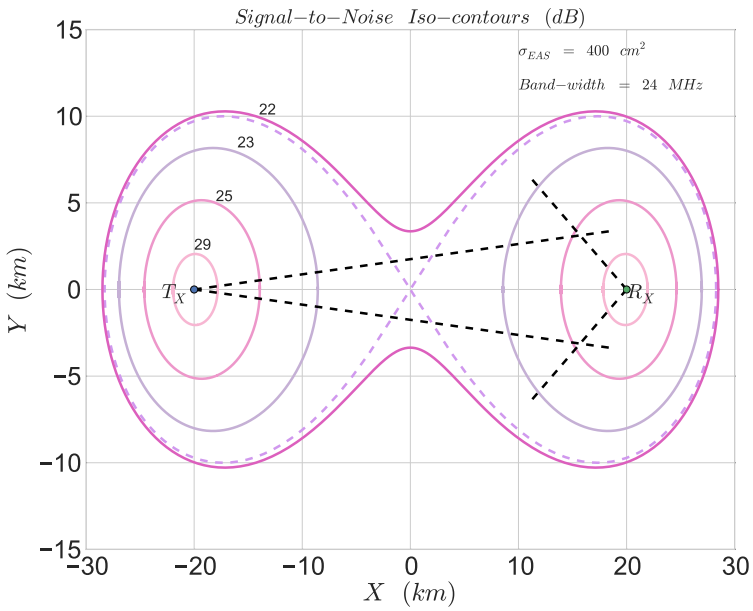

Fig. 2.13 Signal-to-Noise iso-contours for P_T = 40 KW, G_T = 22 dBi, G_R = 12 dBi , λ = 5.545 m, σ_{EAS} = 400 cm^2, B = 24 MHz, T_s = 300 K and separation between Transmitter and Receiver 40 km. The dashed purple line is the Lemniscate of Bernoulli (figure 8-like curve) at $\sim$ 22.1 dB and the black dashed lines are the transmitter and receiver horizontal beamwidths of 10° and 72° respectively.

where $\alpha = \delta + \beta/2$, i.e., the angle between the line of sight between the receiver and the target and the direction of the target.

Fig. 2.14 shows the dependence of the chirp rates between the transmitter and receiver as a function of the horizontal distance from the receiver and the angle α.

2.3.2 Radar Detection of Relativistic Ionization Discs

Recent discussions have addressed the feasibility of radar detection of the relativistic shower front [7], [47] and [48]. In this case, the shower front is treated as a disc rather than a cylinder. The side of the disc has a smaller cross-section than the front; consequently the primary contribution to the scattered signal is considered to be from this shower front as shown in Fig. 2.15.

Here a transmitter (T) illuminates the shower front and is scattered from an element of the plasma in the shower front and received at the receiver (R). The geometry of the radar system is determined by the distances from the shower core to the transmitter (d_T) and to the receiver (d_R), together with their azimuth angles (ϕ_T and ϕ_R) and the altitude of the transmitter (h_T) [7].

Given such a geometry, and since the shower front is continuously being created and destroyed, the interference from the reflected signal from different stages of the shower results in a frequency up-shift.

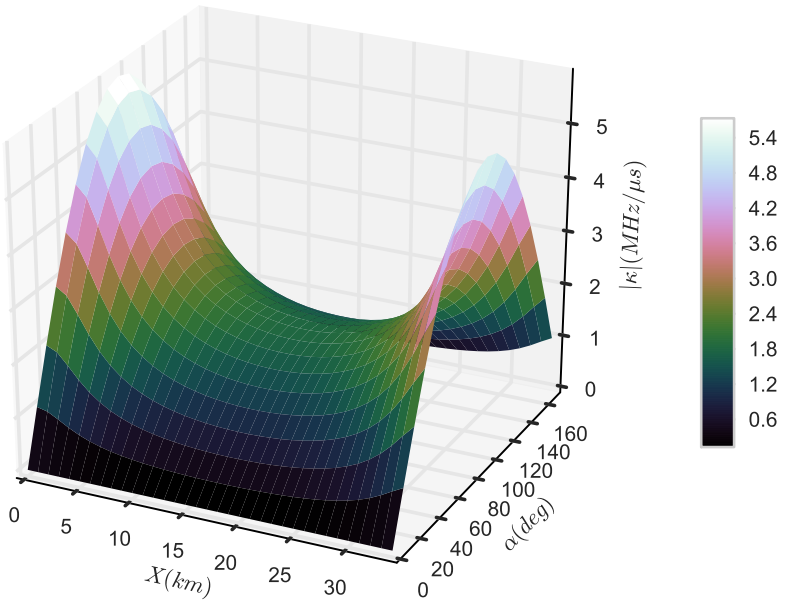

Fig. 2.14 Bistatic Radar Chirp Rates.

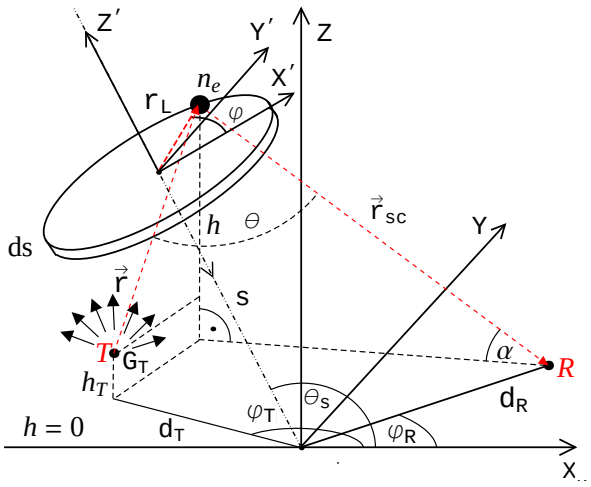

Fig. 2.15 Schematic diagram representing the considered radar system and the reflection from a plasma disk produced by a shower in the atmosphere. Taken from [7]

2.4 Bistatic Radar UHECR Experiments

A handful of attempts have been made to use a bi-static radar configuration to detect the forward scatter of radio waves from UHECR induced air showers.

2.4.1 Mixed Apparatus for Radar Investigation of Atmospheric Cosmic-rays of High Ionization (MARIACHI)

Located in Long Island, United States, MARIACHI consisted of 4 radar stations designed to detect radio signals transmitted by local TV stations and reflected off of cosmic ray showers [8]. In addition, 12 mini conventional scintillator detectors enabled coincidence measurements between radar and scintillator detector triggers. Fig. 2.16 illustrates the schematic of this experiment.

The scintillation detector stations were located at high schools, with each detector comprising four scintillators, each of $0.25m^2$, in classroom corners along with a counter in one of these corners. A Field Programmable Gate Array provided logic enabling the triggering of a cosmic ray event and a Global Positioning System with 100 ns timing accuracy provided an event time-stamp. Orthogonal Inverted VEE dipole antennas provided directional information for radar echo candidate events, and data was subsequently read out using PCR 1000 radio receivers.

2.4.2 TARA

The Telescope Array Radar (TARA) project is similar to the MARIACHI experiment but uses a dedicated transmitter at 54.1 MHz as the radar source. In this bistatic configuration, the transmitter emits the sounding signal, and a distant radar receiver detects radar echoes (chirp). TARA operates in conjunction with a set of conventional cosmic ray detectors in a quiet noise environment at the Telescope Array in Millard County, Utah (www.telescopearray.org/tara/).

Fig. 2.17 shows the layout of the TARA experiment, together with the Telescope Array's fluorescence and surface array detectors.

The TARA receiver operates in Long Ridge, UT (39-14.560 N 113-05.291 W). The receiver antenna is a dual polarized Log Periodic Dipole Antenna designed to match the expected radar echo in the passband from 50 to 80 MHz. Details of the receiver antenna can be found in Chap. 3 and specifics of the radar detector are given in Chap. 4.

The Transmitting facility is just outside the city limits of Hinckley, UT ($39^\circ\ 200'\ 19.824"\ N$, $112^\circ 420'\ 3.24"\ W$). The station comprises a phased high-gain Yagi antenna array and the transmitter.

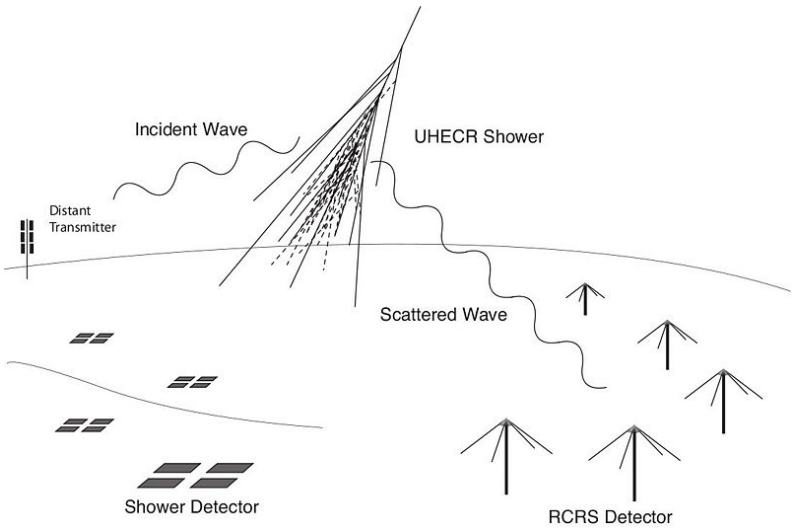

Fig. 2.16 The MARIACHI experiment. Shower scintillation detectors and Radar Cosmic Ray Scattering (RCRS) stations are pictured. Taken from [8].

Transmitter

In June 2009, conventional television programming transitioned from analog to digital in the United States and subsequently vacated the analog TV channel 2 band. TARA received a 20 KW transmitter from KUTV Salt Lake City and obtained a second one from KTVN Reno. TARA re-purposed this transmitter equipment and currently broadcasts continuous wave signals as WF2XZZ at 54.1 MHz, just above the amateur radio band ending at 54 MHz.

Fig. 2.18 shows a functional block diagram of the TARA transmitter.

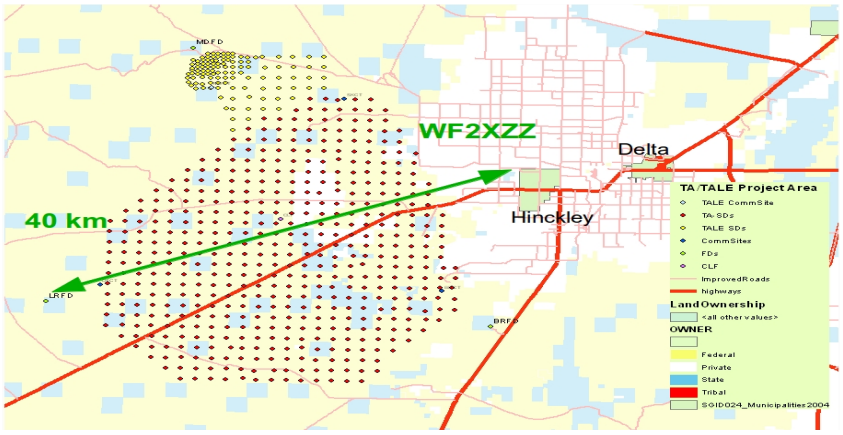

Fig. 2.17 The TARA experiment. Pictured are shower scintillation detectors and fluorescence detector co-located with the radar echo station. Taken from [9]

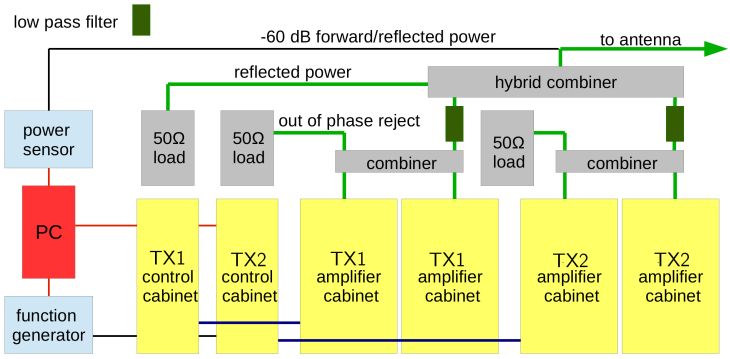

Fig. 2.18 Schematic of the transmitter hardware configuration. Taken from [9]

Transmitting Antenna

The TARA transmitting antenna array consists of 8 narrow-band Yagi antennas, designed and manufactured by M2 Antenna Systems, Inc. Each Yagi, constructed of aluminum, is capable of handling 10 kW of continuous RF power and consists of 5 elements per antenna: a driven element, a reflector, and three director elements. The elements are mounted on a 21.6' long and 2" diameter boom. All elements are constructed of aluminum tubing of 3/4" outer diameter. Each element, except for the driven element, is constructed of two equal sections that are joined at the boom via 7/8" outer diameter sleeve elements. Tab. 2.1 shows the dimensions of these elements and the spacing along the boom.

A balanced t-match is fed from a 4:1 coaxial balun that transforms the unbalanced 50 Ω input to the

Element	Length (in)	Position (in)
Reflector	107.625	-44.375
Driven	100.500	0.000
Director 1	99.500	51.125
Director 2	97.250	131.625
Director 3	97.00	193.625

Table 2.1 Length and relative boom position of antenna elements of the TARA Yagi Antennas. All elements have a outer diameter of $3/4''$.

balanced 200 Ω used to drive the antenna. A 50 Ω 7/8" coaxial waveguide connects the balun to four port power dividers. Further details on the transmitter power delivery can be found in [9].

The eight yagis are phased such that the forward gain is $\sim$ 22 dBi and the front to back ratio is $\sim$ 18 dB. Fig. 2.19 show measured points overlaid on an NEC model [10] for the radiation pattern of the array in the XY and YZ-plane, respectively.

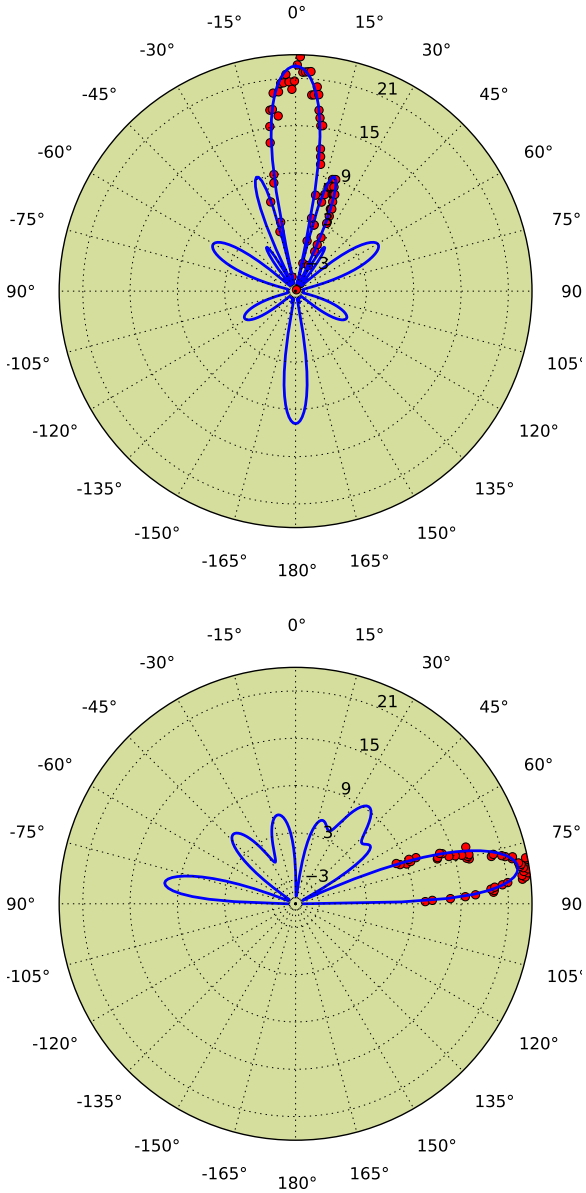

Fig. 2.19 Simulated horizontal (top) and vertical (bottom) radiation pattern of a horizontally polarized TARA phased YAGI Array, shown in blue. Red points represent field data taken using a dedicated receiver antenna. Agreement between simulation and data is observed to be excellent. Taken from [9].

Chapter 3

Log Periodic Dipole Antenna

In this chapter, we discuss the TARA Log Periodic Dipole Antenna's (LPDA's) used to capture EeV cosmic ray radar reflections.

3.1 Theory of Operation

The TARA LPDA's consist of a sequence of parallel linear dipoles close together. The lengths (L_n's) and spacings (R_n's) of these dipoles logarithmically increase, as defined by the inverse of the geometric ratio τ [49],

$$\frac{1}{\tau} = \frac{L_2}{L_1} = \frac{L_{n+1}}{L_n} = \frac{R_2}{R_1} = \frac{R_{n+1}}{R_n} \tag{3.1}$$

with the spacing constant σ,

$$\sigma = \frac{R_{n+1} - Rn}{L_{n+1}} \tag{3.2}$$

These constants determine the frequencies of operation for the LPDA: for TARA these are $\tau \sim 0.82$ and $\sigma \sim 0.54$.

Successive dipoles are connected alternately to opposite sides of a transmission line with the feed point at the end with the shorter elements. Fig. 3.1 shows an equivalent schematic of the receiver LPDA. Tab. 3.1 gives the lengths and positions of the antenna elements on the boom from the front edge to the back. All elements are constructed of aluminum tubing of $1/4''$ outer diameter (d).

Straight lines joining the antenna elements meet at a point called the virtual apex, forming an angle 2α, characteristic of antennas whose pattern and impedance is practically independent of frequency in the band of operation. The angle α, the geometric ratio τ, and the scaling constant, σ are related by,

$$\sigma = \frac{1-\tau}{4tan\alpha} \tag{3.3}$$

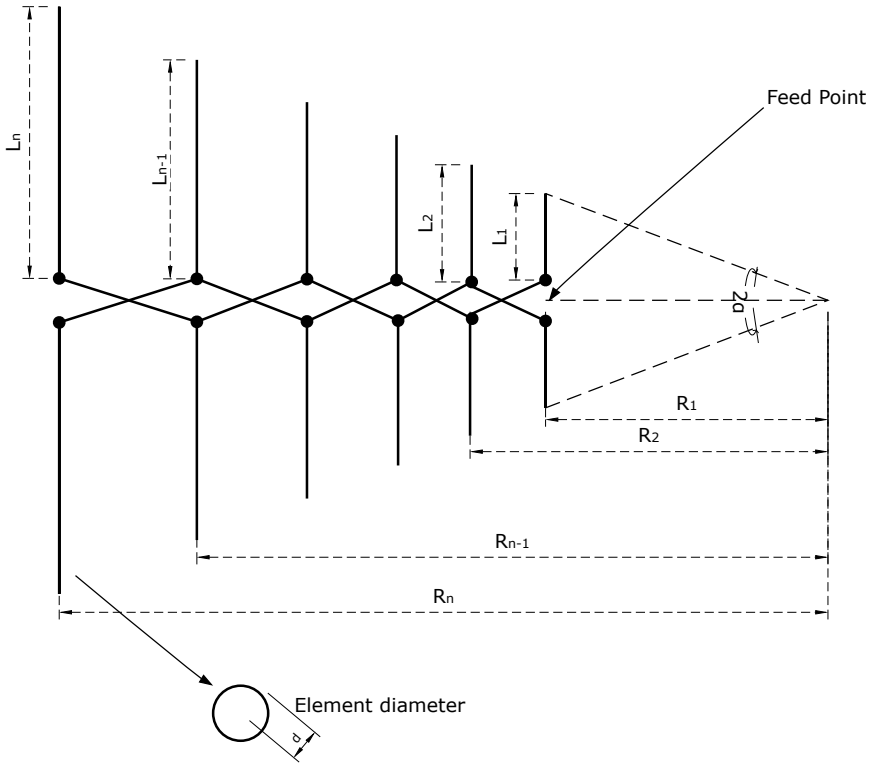

Fig. 3.1 TARA Log Periodic Dipole Antenna (LPDA) equivalent schematic. Virtual Apex angle, α, of $\sim 4.8^{\circ}$.

As an electric field is incident on the antenna, near-resonant length elements of the exciting frequency form the active region of the antenna and can be described as being some number of wavelengths from the virtual apex. As the excitation frequency changes, the active region consequently changes but remains the same number of wavelengths from this virtual apex (See Fig. 3.2). That is,

$$\frac{R_i}{\lambda_i} = const., \qquad i = 1....n. \tag{3.4}$$

As successive dipole elements are connected 180 degrees out of phase, relative to the active region, the closely spaced shorter elements ($< \lambda/2$) have negligible current and provides capacitive impedance. The larger spaced and longer elements ($> \lambda/2$) have small currents and the phase reversal provides inductive impedance.

Element	Length (in)	Position (in)
1	21.875	3.625
2	26.625	18.0625
3	32.5	35.625
4	39.625	57.0
5	48.3125	83.125
6	58.3125	115

Table 3.1 Length and relative boom position of antenna elements of the TARA Log Periodic Dipole Antennas. All elements have a diameter of $1/4''$.

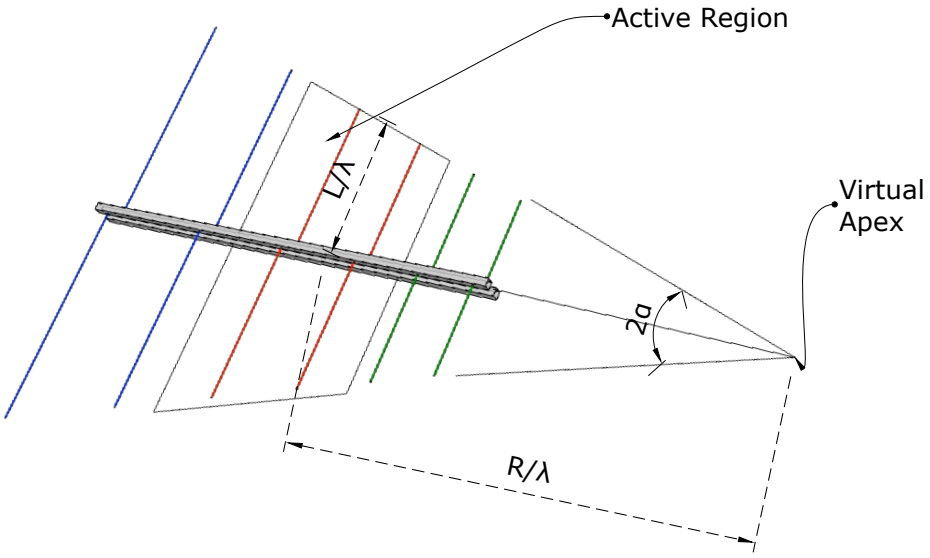

Fig. 3.2 TARA LPDA showing the active region (red), inductive elements(blue) and capacitive elements (green) in response to an incident excitation frequency, as a consequence of phasing.

3.2 Antenna Simulations with NEC

Several parameters characterize an antenna: Antenna geometry, operating frequency, and the environment, particularly the type of ground. To get information on characteristics like directionality one must solve the electric field integral equation (EFIE),

$$\vec{\varepsilon}(\vec{r}) = -\imath\omega\mu \int_V \vec{G}(\vec{r},\vec{r'})\vec{j}(\vec{r'})d\vec{r'} \tag{3.5}$$

where $\vec{j}(\vec{r'})$ is the current density located in the volume defined by the antenna geometry, $\mu = \mu_0\mu_r$ the permeability, and $\vec{G}(\vec{r},\vec{r'})$ is the dyadic homogeneous Green's function. [50] provides a detailed treatment.

Numerical Electromagnetic Code (NEC) [10] is a simulation tool that employs the Method Of Moments (MOM) to solve this EFIE numerically.

Equation 3.5 appears similar to the generalized form,

$$L(I) = E \tag{3.6}$$

where L is a linear operator, E is the excitation source (electric field), and I is an unknown function (current).

In MOM, I is first expanded into a sum of N weighted basis functions,

$$I \approx \sum_{n=1}^{N} a_n I_n \tag{3.7}$$

where a_n are unknown weighting coefficients, and since L is a linear operator, one can write,

$$\sum_{n=1}^{N} a_n L(I_n) \approx E \tag{3.8}$$

The basis function (wire segment) in NEC is represented by,

$$a_n I_n = A_n + B_n sink(s - s_n) + C_n cosk(s - s_n) \qquad with\ |s - s_n| < l_n/2 \tag{3.9}$$

where s is the position along the n^{th} segment with center s_n and length l_n. NEC then solves for the 3N coefficients in equation 3.9 by applying boundary-conditions between segment junctions and at the ends. A set of basis functions sum to give the overall current, as shown for a four-segment wire, e.g., in Fig. 3.3.

NEC (TARA uses both NEC-2 and NEC-4) requires that the length of wire segments should not exceed $1/10^{th}$ of the wavelength of operation to ensure accuracy. Tab. 3.2 gives the number of wire segments used for each wire and the corresponding length per wire segment.

Element	Segs	Length (in)
1	11	0.33
2	11	1.64
3	11	3.24
4	11	5.18
5	13	6.40
6	15	7.67

Table 3.2 Number of wire segments for each wire and the corresponding length per segment.

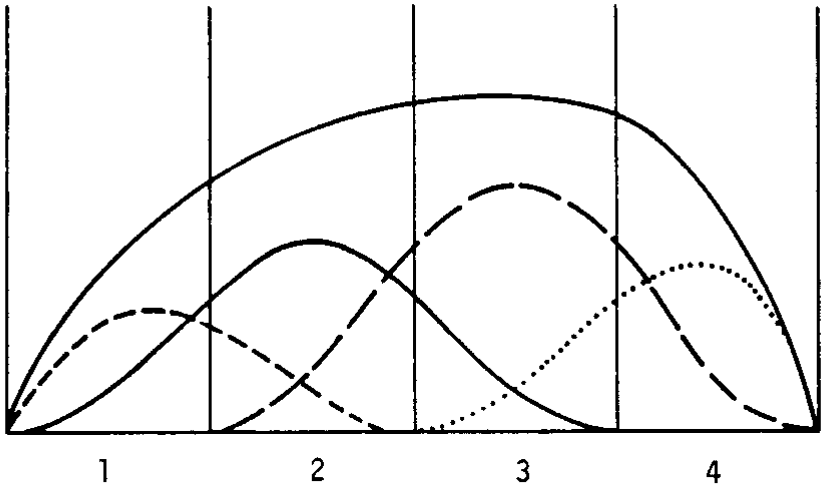

Fig. 3.3 Current Basis Functions and their sum on a four wire segment. Taken from Ref. [10]

3.3 Antenna Characterization

Frequency-independent performance requires that the antenna appear electrically the same to the exciting wave at all frequencies. TARA expects cosmic rays in the 50 to 80 MHz band, and correspondingly the antenna has the minimum number of elements required in their respective active regions for response over the desired passband. The length of the LPDA elements constrains the maximum and minimum possible frequencies.

$$f_{min} \approx \frac{c}{4 \cdot l_{max}} \approx 50MHz \qquad and \qquad f_{max} \approx \frac{c}{4 \cdot l_{min}} \approx 135MHz \tag{3.10}$$

The impedance of the antenna to a 50 Ω transmission line was measured in an anechoic chamber and simulated using NEC4. The voltage standing wave ratio (VSWR) in terms of the magnitude of the complex reflection coefficient (S_{11}) is given by,

$$VSWR = \frac{1+|s_{11}|}{1-|s_{11}|}, \tag{3.11}$$

and is shown as a function of frequency in Fig. 3.4. A VSWR of 3.0 implies that 75% signal power is transmitted from the antenna to the environment at a given frequency.

At time t, the electric field arriving at the antenna from some direction (θ, ϕ) is a transverse two-component vector given by,

$$\vec{E}(t) = \vec{e_\theta} E_\theta(t) + \vec{e_\phi} E_\phi(t) \tag{3.12}$$

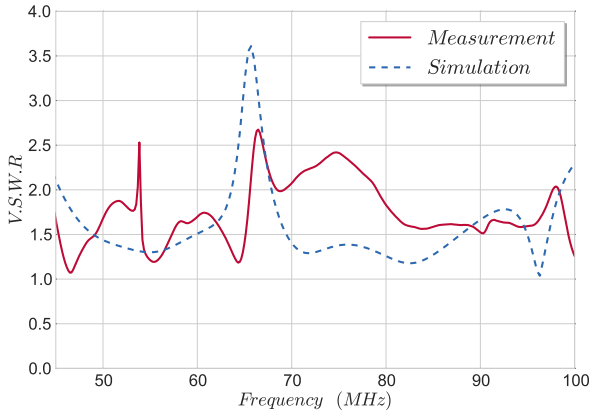

Fig. 3.4 Overlay of SWR of a horizontally polarized TARA LPDA as measured in the KU anechoic chamber compared with NEC simulation.

where θ and ϕ denote independent polarizations (the radiation electric field is only transverse and for this reason has no component E_r). Fig. 3.5 depicts the coordinate system. The field can be linearly, circularly or elliptically polarized.

Of particular interest at some time t is the electric field in the antenna's far field relative to that of some isotropic antenna and as a function of angular space. The antenna power measured in dBi (decibels w.r.t isotropic) is described as,

$$P_i(\theta,\phi) = 10log_{10}\frac{S(\theta,\phi)}{S(\theta,\phi)_i} \tag{3.13}$$

where,

$$S(\theta,\phi) = [E_\theta^2(\theta,\phi) + E_\phi^2(\theta,\phi)]/Z_0 \tag{3.14}$$

is the Poynting Vector of an isotropic antenna in its far field and $Z_0 \sim 377\Omega$ the intrinsic impedance of free space.

Fig. 3.6 shows measured points overlaid on a NEC model for the radiation pattern of the antenna in the XY-plane. Transmission coefficient (S_{21}) measurement give a measure of the total transmitted power of a wave relative to an incident wave. These measurements were made using two identical horizontally polarized LPDA's at a separation of 5λ at the carrier frequency of 54.1 MHz. As the measurements were relative, not absolute, a uniform scale factor was determined by minimizing χ^2 between the model and data.

Lowering a horizontally polarized dipole antenna from some height, again at the carrier frequency, and measuring the received power at a horizontally polarized LPDA on the ground enabled confirmation of the radiation pattern in the YZ-plane. As previously, a χ^2 minimization between measurement and simulation was performed. (See Fig. 3.7)

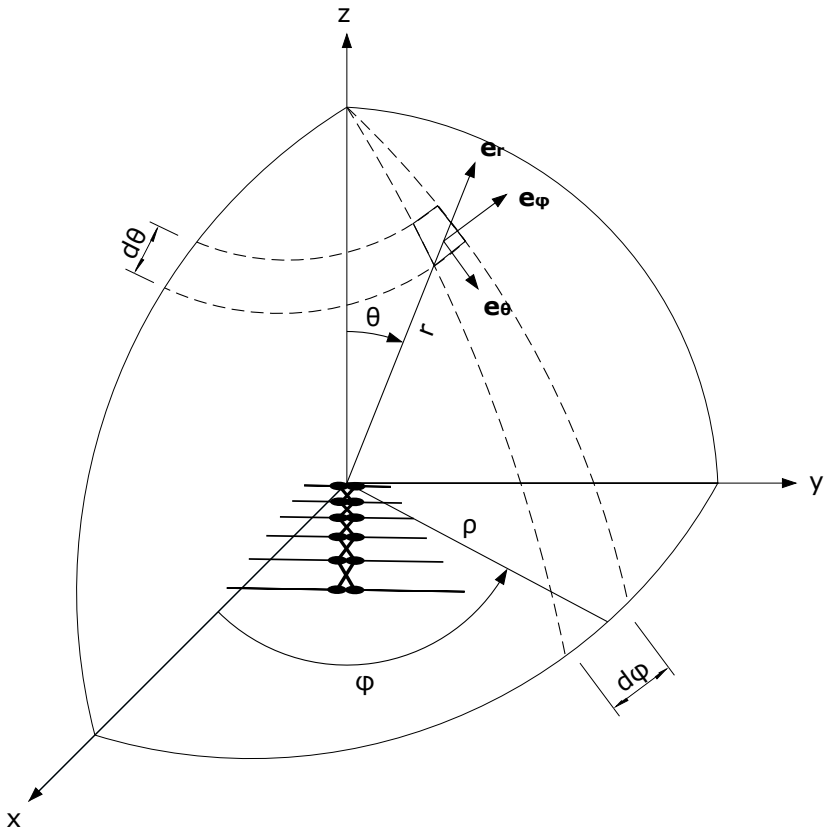

Fig. 3.5 Spherical Coordinate System used for defining antenna geometry.

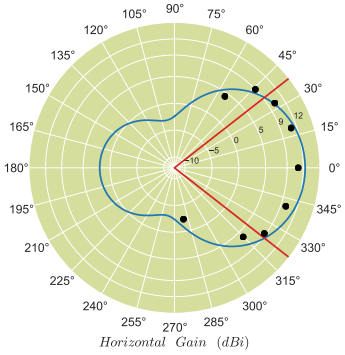

Fig. 3.6 Radiation pattern in the XY-plane of a horizontally polarized TARA LPDA at the transmitter sounding frequency of 54.1 MHz. Beamwidths (3 dB below peak gain) are shown with red lines. Black points show field measurements.

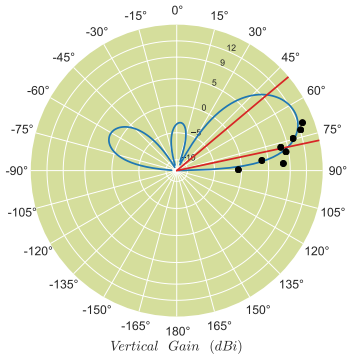

Fig. 3.7 Radiation pattern in the YZ-plane of a horizontally polarized TARA LPDA at the transmitter sounding frequency of 54.1 MHz. Beamwidths (3 dB below peak gain) are shown with red lines. Black points show field measurements.

In the case of the radiation pattern plot in the YZ-plane, a ground plane effect is seen due to the superposition of the direct wave on the antenna and that of the wave reflected from the ground.

For a vertically polarized antenna, the radiation pattern is expected to be similar but switched in the E(XZ) and H(YZ) planes.

A property associated with the radiation pattern is the half-power beamwidth, ϕ_{HPBW} and θ_{HPBW} in the antenna E and H planes respectively, defined as the points where the power decreases by 3 dB. The relationship between the half-power beamwidths and power is given by,

$$\theta_{HPBW}\,\phi_{HPBW} \cong \Omega_A = \int_{\phi=0}^{\phi=2\pi} \int_{\theta=0}^{\theta=\pi} P_i(\theta,\phi) sin\theta d\theta d\phi, \tag{3.15}$$

where Ω_A is the beam area, defined as the solid angle through which most of the power radiates.

Fig. 3.8 and Fig. 3.9 show the horizontal half-power beamwidth and the front-to-back ratio of the antenna measured in the KU anechoic chamber.

3.4 Effective Height

The relationship between the terminal voltage at the antenna feeds and the incident electric field [51] is given by,

$$V = \vec{h} \cdot \vec{E} = hEcos\theta, \tag{3.16}$$

where h is the effective height and θ the angle between the electric field polarization and the dipole.

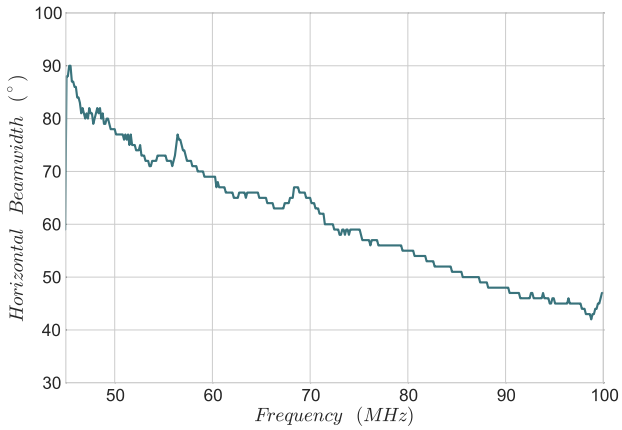

Fig. 3.8 Beamwidth of a horizontally polarized TARA LPDA, as measured in the KU anechoic chamber.

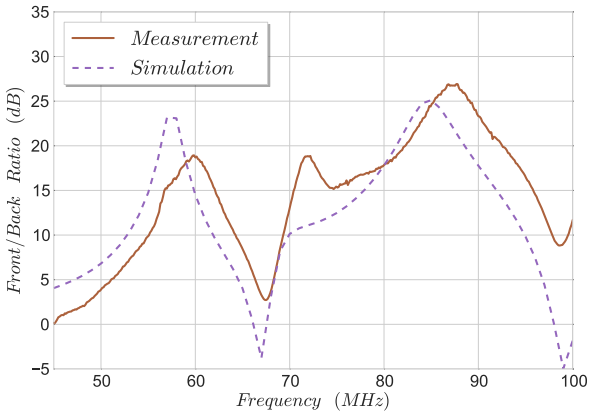

Fig. 3.9 Front-to-Back ratio of a horizontally polarized TARA LPDA, as measured in the KU anechoic chamber and an overlay of NEC simulation. The discrepancy is likely due to differences in the height of the antenna while taking the measurement ($\sim 6ft.$) vs. simulation ($12ft.$).

A detailed discussion of the effective height is presented in [52] and is given by (see Fig. 3.10),

$$h(f) = 2 \times \sqrt{\frac{G}{4\pi} \frac{c^2}{f^2} \frac{Z}{Z_0}} \tag{3.17}$$

where G is the unit-less gain, c the speed of light, f the frequency, Z the impedance at the antenna terminals and Z_0 the impedance of free space.

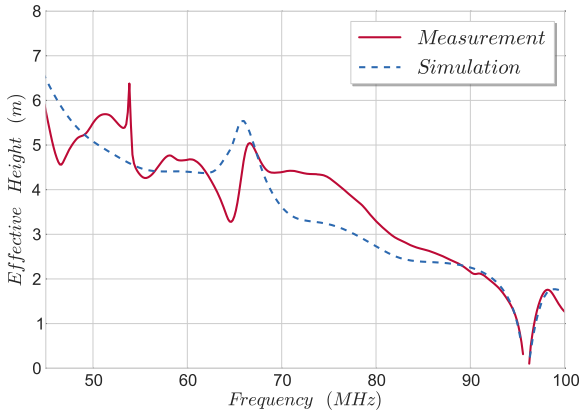

Fig. 3.10 Effective Height of the TARA LPDA.

3.5 Galactic Floor

In any RF receiver system, sensitivity is limited by the combination of external noise entering through the antenna and internal noise from various sources like low-noise amplifiers and other resistive losses from filters, cables, and couplers. The sky, earth, and antenna resistive loss generate noise entering the antenna. Diffuse radio noise from the galactic plane is non-polarized and is the dominant noise source in the TARA frequency band.

After accounting for the amplifier and instrumental gains and losses, the observed noise background can be compared with the irreducible galactic noise background [53] across the passband. Specifically, toward the South Galactic Plane the spectrum of specific intensity in units of $Wm^{-2}Hz^{-1}sr^{-1}$ is given by,

$$I_\nu = I_g \nu^{-0.52} \frac{1 - exp[-\tau(\nu)]}{\tau(\nu)} + I_{eg} \nu^{-0.80} exp[-\tau(\nu)], \tag{3.18}$$

where ν is in MHz, the two terms I_g and I_{eg} correspond to galactic and extragalactic contributions

respectively and $\tau(\nu)$ is the opacity in the polar direction. The parameter values are

$$I_g = 2.48 \times 10^{-20}, I_{eg} = 1.06 \times 10^{-20}, \tau(\nu) = 5.0\nu^{-2.1}. \tag{3.19}$$

The apparent brightness temperature, T_b (figure 3.11), is then related by the Rayleigh-Jeans Law:

$$kT_b = I_\nu c^2/2\nu^2. \tag{3.20}$$

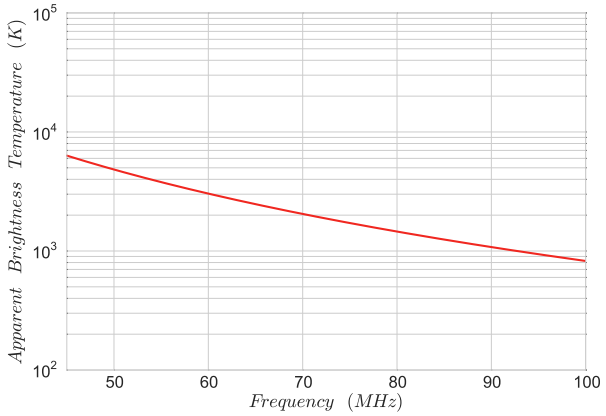

Fig. 3.11 Apparent brightness temperature of the sky.

The system noise was first measured using the LPDA, 100ft of LMR-400 cable, a front end module comprising a 61 dB amplifier (MITEQ AU - 1525), FM notch filter (Mini-Circuits NBSP - 108+), a high pass and low pass filter and a HP 54542C oscilloscope sampling at 250 MSa/s with 32768 samples being taken in so-called snapshots every 30 seconds. See Fig. 3.12.

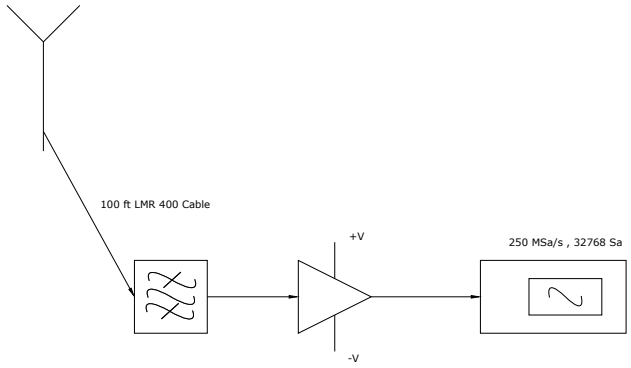

Fig. 3.12 An experimental setup to measure average system noise. Snapshots were taken every 30 seconds for 1 week.

The average measured system noise is calibrated by removing the effects of individual components in the receiver RF chain from the average snapshot spectra to determine the absolute received power. Without any scaling, the corrected received power compares well with the Galactic expectation [54] (see Fig. 3.14). Principal components, for which adjustments are made, include filters and amplifiers measured via the transmission coefficient, and also the transmission line using the manufacturer's attenuation per unit-length data (Fig. 3.13). Transmission line attenuation is found via,

$$Attenuation(dB)/100ft = c\cdot\sqrt{(F[MHz])} + (0.000260)\cdot F[MHz] \tag{3.21}$$

where the constant $c = 0.075550$ for LMR - 600 and $c = 0.122290$ for LMR - 400 cable.

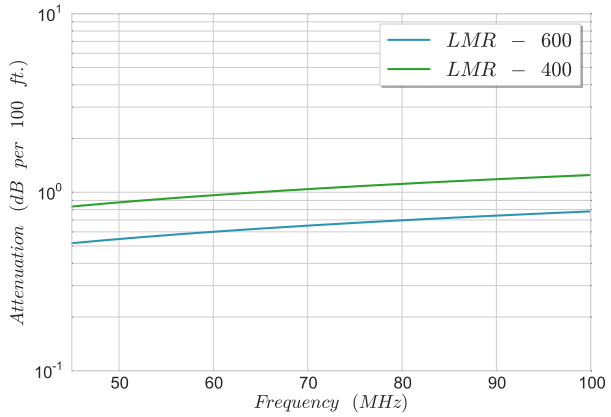

Fig. 3.13 Attenuation in dB per 100 ft of the LMR - 600 and LMR - 400 transmission lines.

Anthropogenic noise sources are transient and noise is absent in the measurement band due to the receiver site's remote location. In this frequency region, galactic noise dominates thermal and other noise sources.

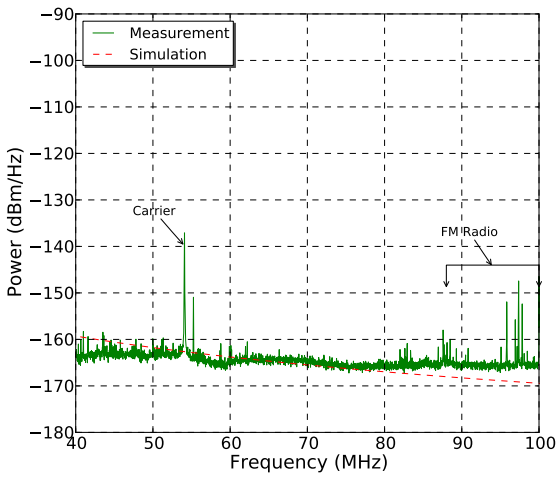

Fig. 3.14 Average receiver system noise floor (green) Power Spectral Density (PSD) in dBm/Hz superimposed with a fit to the known galactic background noise (red dashed line). System attenuation, filters, and amplifiers were accounted for in calculating the absolute received power.

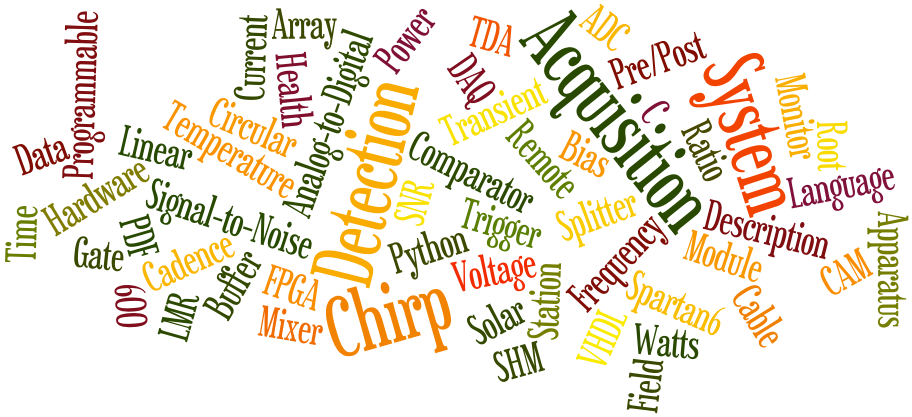

Chapter 4

Cosmic Ray Detector

In order to detect cosmic ray chirps while also adding stereoscopic measurement capabilities in a radio-quiet environment, receiver stations have been developed. These remote stations have a mostly analog data acquisition system that has low power consumption and at a cost that is comparatively inexpensive. This chapter includes discussions on the triggering logic, powering, and the communication system and some specific details of hardware components.

4.1 Station Structure

The station is designed to detect chirp echoes that have low signal-to-noise ratios. A dual-polarized LPDA (Chapter 3) feeds the two station channel inputs. The station consists of four basic components: the Mixer Module, Chirp Acquisition Module (CAM), Transient Detector Apparatus (TDA), Current Voltage Temperature (IVT) Board and the System Health Monitor (SHM). Fig. 4.1 shows these components that are powered via solar panels, while a GHz transceiver provides communications with the Longridge fluorescence detector station, which houses Internet communications. A discussion of these components, as well as the powering and communications systems follow.

4.2 Mixer Module

The signal of interest is a chirp signal that has duration T_c seconds, a changing Amplitude A(t) with start phase ϕ_0, start frequency f_0, stop frequency f_1 and chirp rate κ Hz/s. Both up and down chirps are treated identically in the detector. Fig. 4.2 is an example of the signal of interest. Assuming that it is

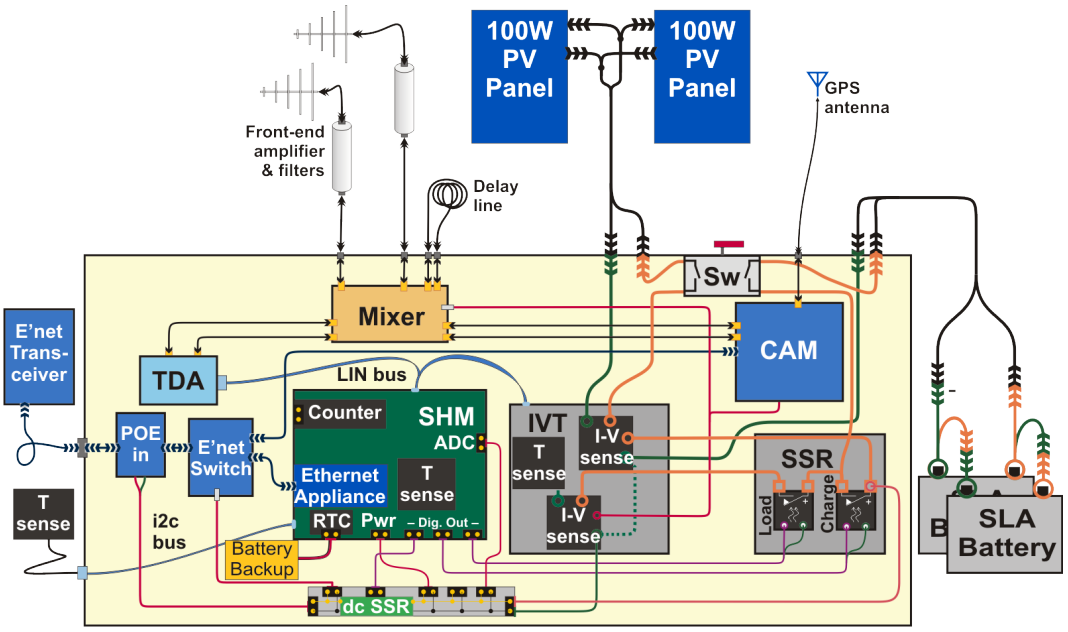

Fig. 4.1 Construction schematic showing the different Components of the TARA detector. *Courtesy Kenneth Ratzlaff, Instrumentation Design Lab, KU.*

centered around time t = 0, such a chirp signal can be written as,

$$s(t) = A(t)sin(\phi_0 + 2\pi f_0 t + \pi\kappa t^2) \tag{4.1}$$

To detect the presence of the signal s(t) without prior knowledge of the chirp rate κ, the signal is first down-converted to a monotone. To achieve this, the signal is mixed with a delayed copy of itself, i.e $s(t) \bigotimes s(t-\tau)$ [55], as depicted in the radar block diagram in Fig. 4.3.

For an incident chirp signal, the non-linear components in the mixer result in a product term that yields a monotone at a beat frequency

$$f = \kappa\tau, \tag{4.2}$$

where τ is the delay time. This delay is created with LMR-600 cable, which introduces negligible losses. This is illustrated in Fig. 4.4, where a -10 MHz/μs chirp is down-converted to a 1 MHz monotone (100 ft of LMR-600 cable was used here).

Signal "de-chirping" is done in the mixer module consisting of Radio Frequency (RF) components as shown in Fig. 4.5. This mixer module receives both antenna channels.

The mixer module components for channel 1 are: a splitter (ZMSC-4-1-BR, Mini-Circuits), mixer (ZX05-1L-S+, Mini-Circuits), filter (SLP-1.9+, Mini-Circuits), amplifier (ZFL-500LN+B, Mini-Circuits) and bias tee (ZFBT-4RG-FT, Mini-Circuits). In addition to copies of the incoming signal used in de-

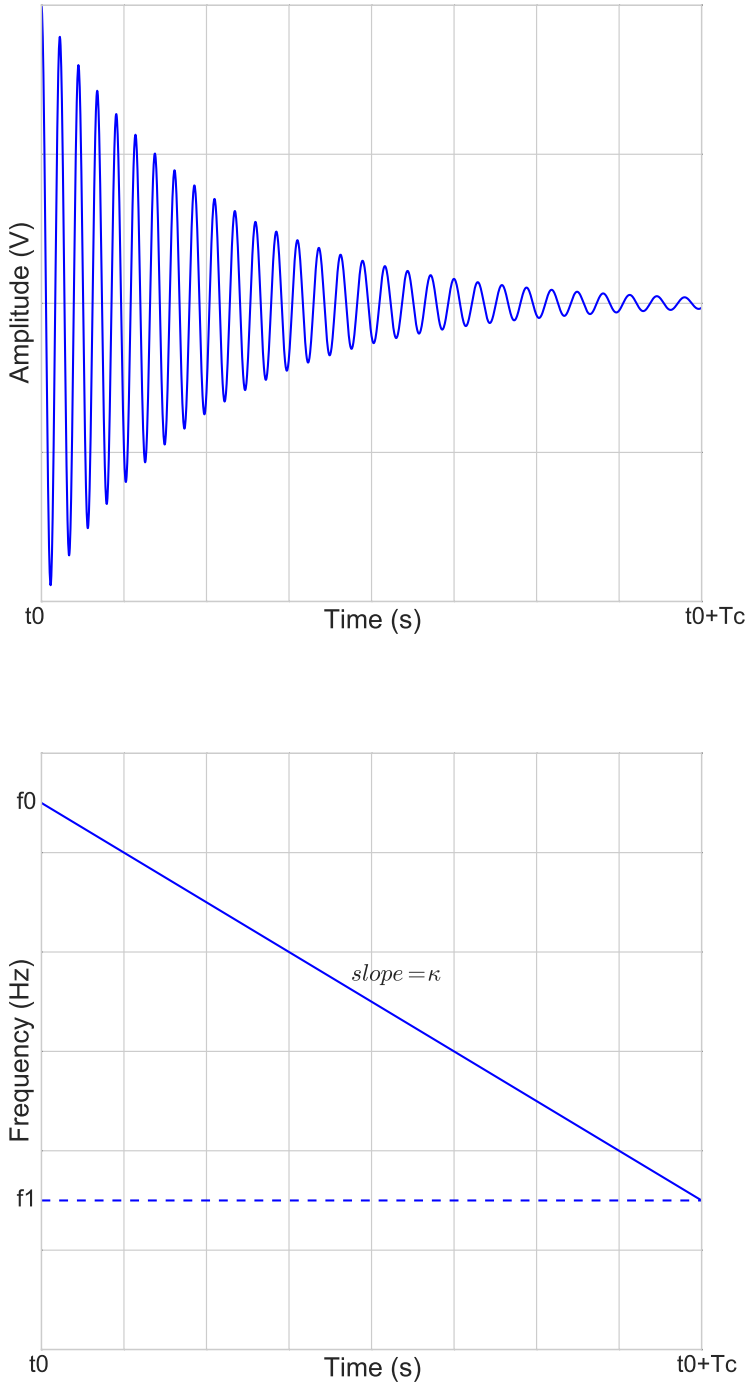

Fig. 4.2 A linear down-chirp in the time domain (top) and frequency-time domain (bottom).

Fig. 4.3 Radar block diagram showing the down-conversion process along with the filtering and enveloping process.

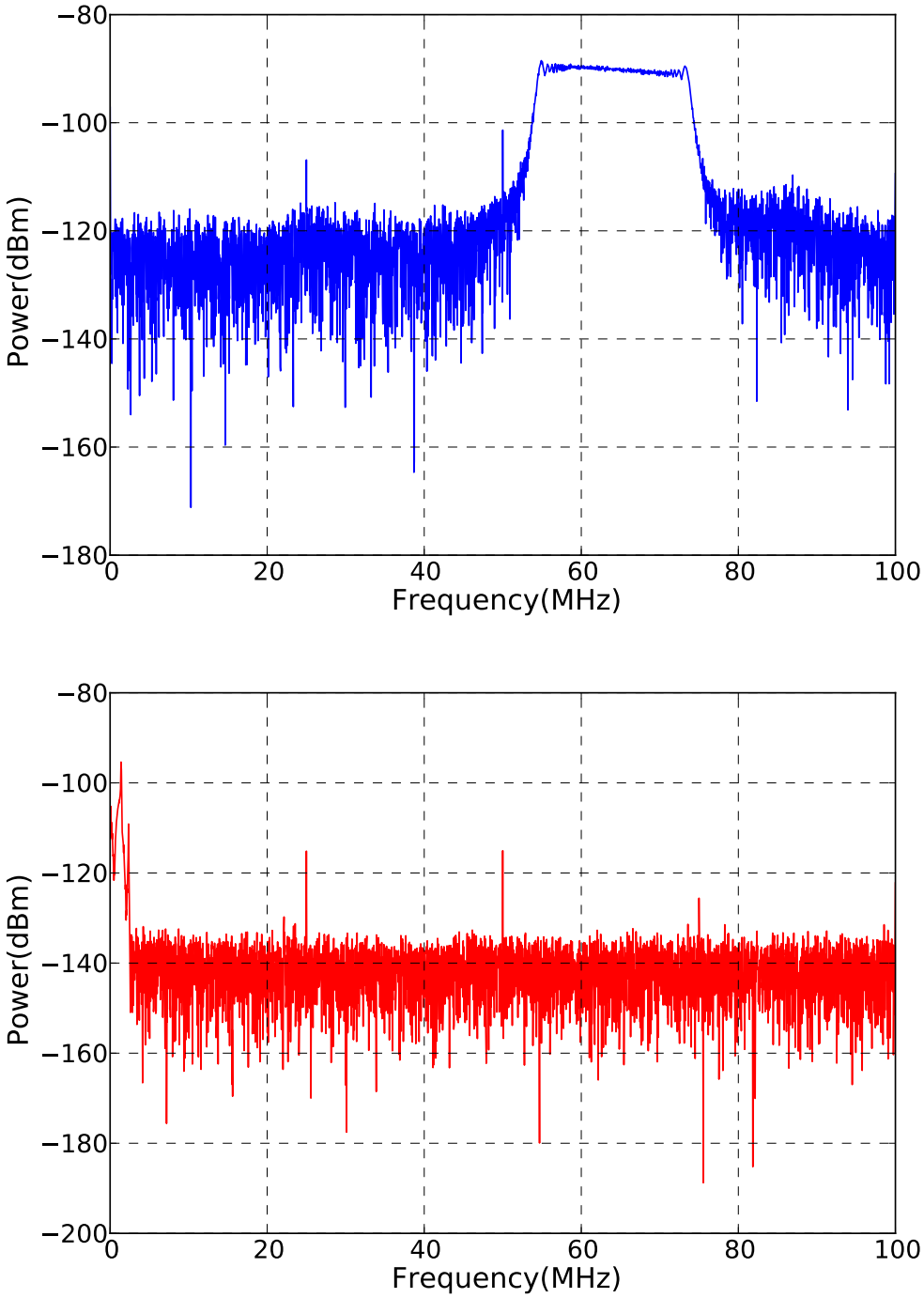

Fig. 4.4 Top: Power spectrum of a -10 MHz/μs chirp created by a signal generator, prior to mixing. Bottom: power spectrum of a 1 MHz monotone signal after signal mixing and passing through a low pass filter. The chirp is evident as the left-most peak in this distribution. The 24 MHz peak and the 48 MHz harmonic is likely due to a Serial Peripheral Interface(SPI).

chirping, additional copies are sent to a TDA and a High-Speed ADC.

For Channel 2, the mixer module consists only of a bias tee (ZFBT-4RG-FT, Mini-Circuits) leading into a TDA.

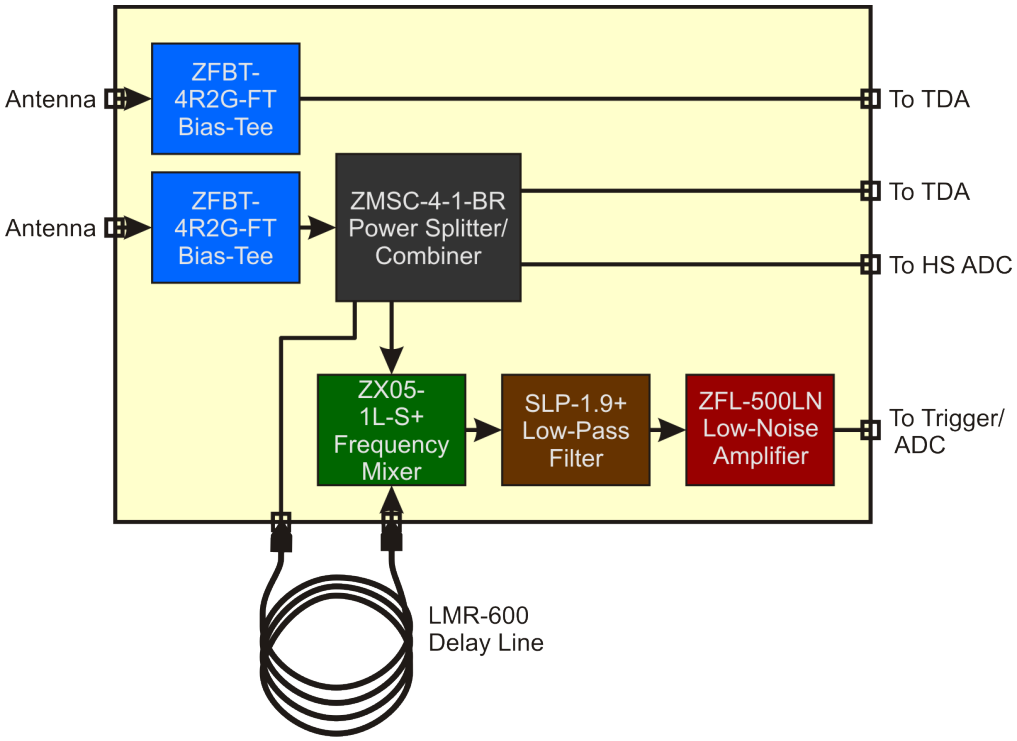

Fig. 4.5 Block diagram showing the different components of the mixer module. *Courtesy Kenneth Ratzlaff, Instrumentation Design Lab, KU.*

4.3 Triggering Mechanism

The expected value of chirp rates from EAS echoes are typically between -10 to -1 MHz/μs [9] (see Chapter 2). Consequently, with 95 ns delay, the down-converted signal has a frequency between $\sim$100 kHz and 1 MHz. To trigger, the mixed signal is split into multiple copies. Each copy is then passed through a bandpass filter and an envelope detector. Different frequency bands are then compared by majority logic in a Field Programmable Gate Array (FPGA) , requiring no more than two bands to form a trigger in order to suppress impulsive noise. Each of the frequency banded outputs corresponds to a separate range of chirp rates.

To illustrate the triggering mechanism, in the oscilloscope-based example in Fig. 4.6, after mixing and filtering, the signal is passed through a power detector (8471D; Agilent, Inc.). Here, a chirp with

0 dB SNR at a rate of -1 MHz/μs is first band-pass filtered (41–100 MHz) and then amplified by 20 dB. Next, the signal is mixed and low-pass filtered (DC-1.9 MHz) and then passed through the Agilent power detector.

4.4 Chirp Acquisition Module (CAM)

The CAM is an embedded system with a modular design that provides hardware and software integration for chirp detection. It consists of five basic parts: Trigger Board, High-Speed Board, FPGA, Global Positioning System (GPS) and a Single Board Computer (SBC) as shown in Fig. 4.7. A description of each of these subsystems follows.

4.4.1 Trigger Board

Fig. 4.8 shows a general layout of the Triggering board.

The input to the trigger board is an SMA female connection. The input signal is first split into four copies, and then each passed through a bandpass filter followed by an envelope detector (see Fig. A.2). The bandpass filters are Butterworth Pi filters with passbands as given in Table. 4.1 and Bode plot in Fig. 4.9.

Channel	3dB Low Pass Cut Off (KHz)	3dB High Pass Cut Off (KHz)	3dB Band-Width (KHz)
A	344	18	326
B	570	240	330
C	864	549	315
D	1117	818	308

Table 4.1 Passband of the Butterworth Pi Filters and the corresponding Channels.

The envelope detector consists of a rectifying diode followed by an RC combination that allows the output waveform to follow the envelope of the signal [56]. Fig. 4.10 shows a simulated 50 KHz sine wave signal passed through an envelope detector. The Figure illustrates the subsequent response in the four different signal paths.

Next, the four channels are passed into the ADC (AD80066) [57], operating from a 5V supply. The ADC is packaged in a Small-Shrink-Outline-28-Package (SSOP-28 package) [57] and nominally consumes 490 mW. It runs in the Sample and Hold Amplifier (SHA) mode with the 16-bit output multiplexed into 8-bit words and accessed in two read cycles clocking at 3MHz per channel. Fig. 4.11 shows the read operation timing diagram.

The ADC register is programmed via the Serial Peripheral Interface (SPI) Bus at 24MHz as shown in the timing diagram in Fig. 4.12.

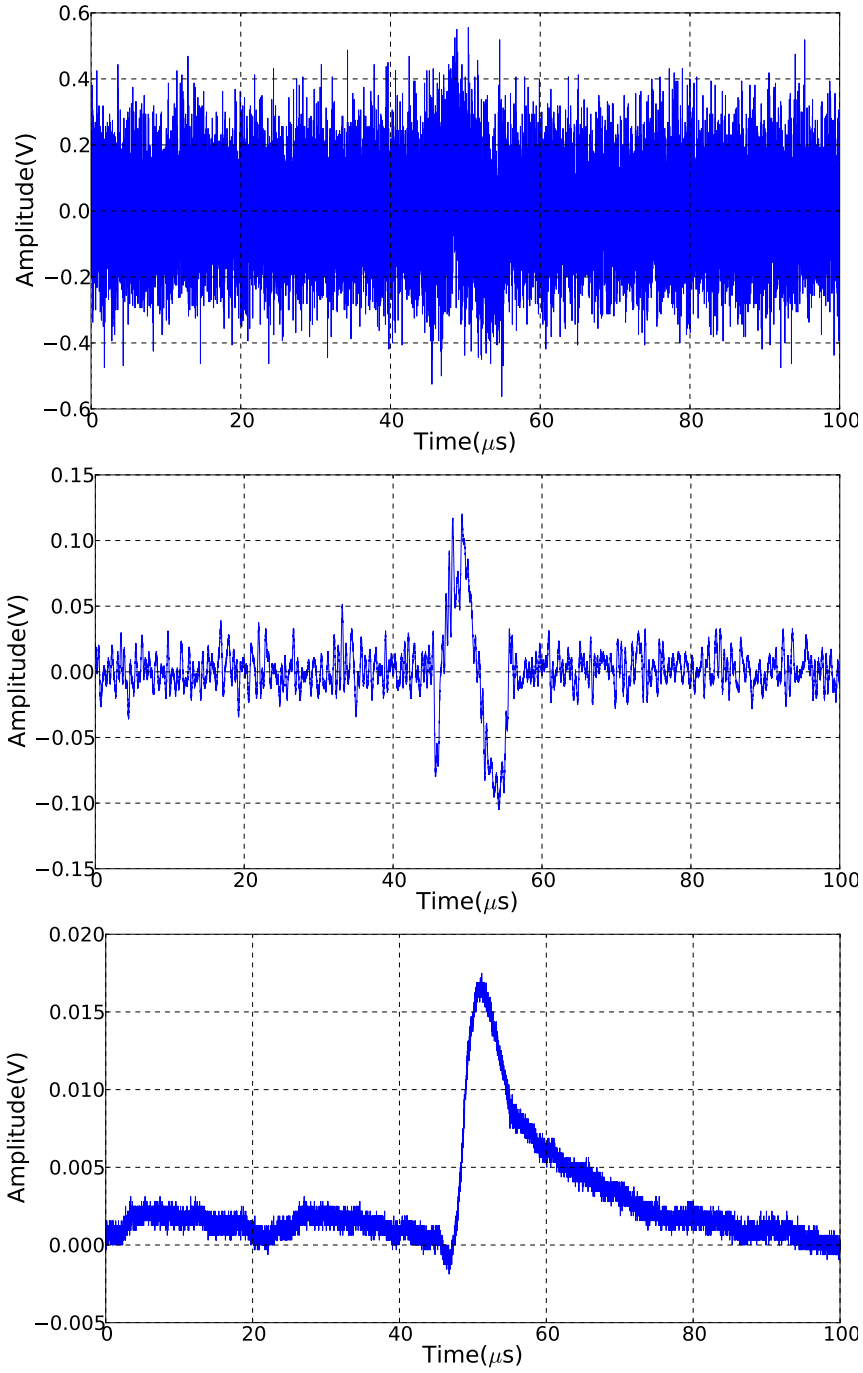

Fig. 4.6 Top: 0 dB SNR and 1 MHz/μs chirp embedded in noise prior to "de-chirping". Second from top: The monotone signal after input chirp is mixed with delayed copy of itself and passed through a low-pass filter. Bottom: Monotone passed through the Agilent 8471D power detector.

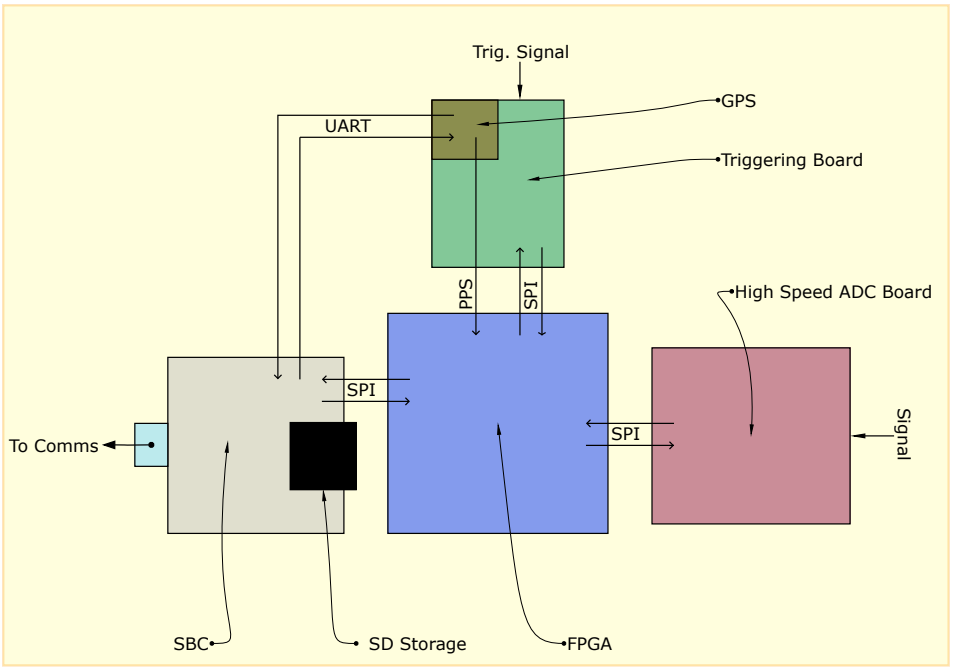

Fig. 4.7 Elements of the CAM unit showing the communications protocols.

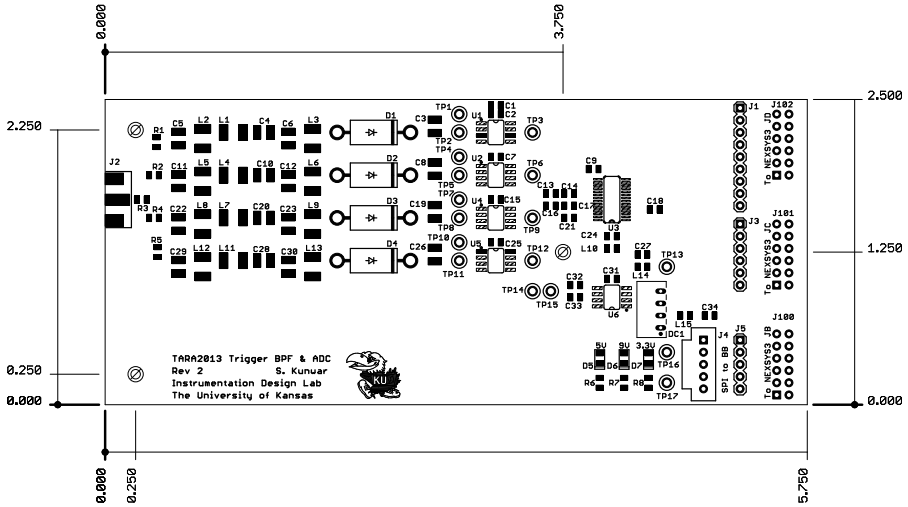

Fig. 4.8 Trigger Board Schematics. *Courtesy Rob Young, Instrumentation Design Lab, KU.*

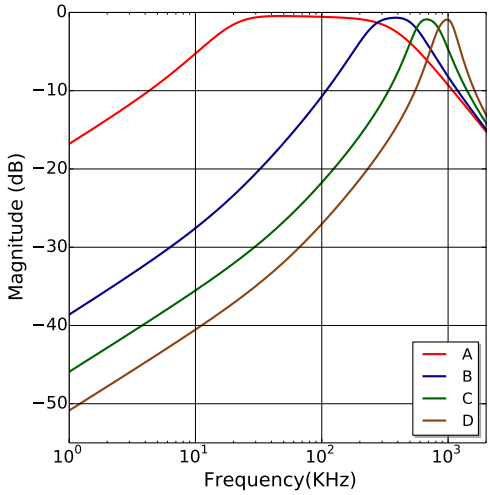

Fig. 4.9 Bode plot for the four bandpass filters.

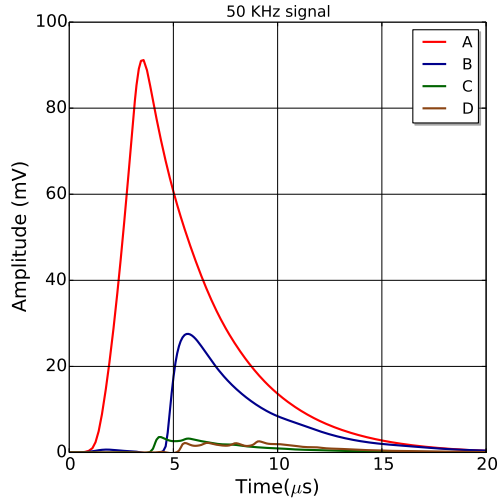

Fig. 4.10 A 50 KHz sine wave signal response from the envelope detector in each signal path.

The data are transferred via the FPGA Peripheral module (Pmod) interface for triggering (see Sec. 4.4.3).

The GPS module (i-Lotus M12M) is commercially available and mounted on the Triggering Board as well. Fig. A.3 shows the connections between the FPGA, SBC, and the GPS and Triggering Board.

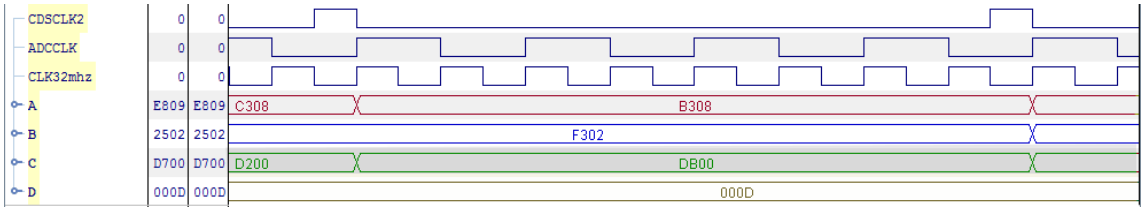

Fig. 4.11 Read operation timing for the Analog Devices AD80066 ADC. 16 bits are multiplexed as two 8-bit words at 3 MHz per channel.

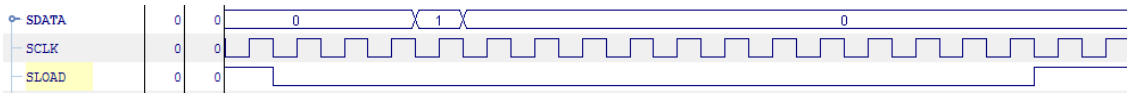

Fig. 4.12 SPI Timing for the Analog Devices AD80066 ADC. SCLK is the 24MHz transfer rate clock; 16 bits are transferred while valid programming i.e while SLOAD is pulled low.

4.4.2 High-Speed Board

The TARA High-Speed Board is a commercially available AD9634 Evaluation Board [58]. The board consists of a 12-bit ADC sampling up to 250 MHz, with a total power consumption of 360mW. The ADC clocks at 200 MHz and uses a 1.8V SPI port at 24 MHz for register programming and read-back (see Fig 4.13).

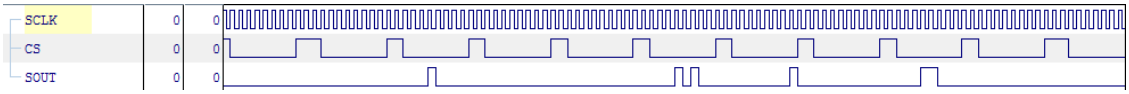

Fig. 4.13 SPI Timing for the Analog Devices AD9634 ADC. SCLK is the 24MHz transfer rate clock; 8 bits are transferred while valid programming, i.e. while SLOAD is pulled low.

Differential signaling provides superior common-mode noise rejection. 12-bit words are transferred using a custom adapter (Fig. A.4) between the Evaluation Board's Low Voltage Differential Signaling (LVDS) parallel output port and the Very High Density Cable (VHDC) on the FPGA. In the next section, we discuss the timing details.

4.4.3 FPGA

The CAM uses the Xilinx Spartan 6 FPGA based Nexsys 3 digital system board [11].

To configure the FPGA, the configuration file saved with a '.mcs' extension is first stored in a non-volatile parallel Phase Change Memory (PCM) device. This is then transferred to the FPGA on power up via the BPI-UP port. On the development board, this is one of the four possible configuration modes and is achieved by removing all connections on the J8 jumper [11] (See Fig. 4.14)

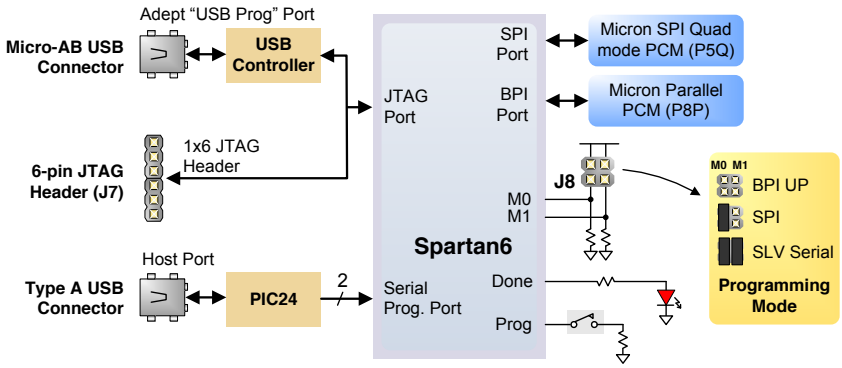

Fig. 4.14 Spartan 6 Programming via BPI port (BPI prom 28F128P30). Taken from [11].

The Nexys3 board includes a single 100MHz Complementary metal–oxide–semiconductor (CMOS) oscillator connected to pin V10 [11](V10 is the GCLK0 input in bank 2). Phase Locked Loop (PLL) , and Digital Clock Manager (DCM) features on the board can be used to synthesize other frequencies. The DCM is configured to produce two 48 MHz clocks (see Fig. 4.15).

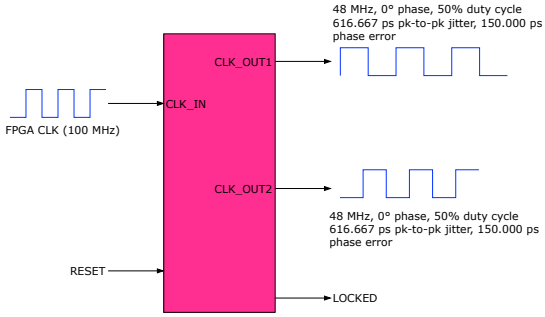

Fig. 4.15 Nexsys 3 board's 100 MHz CMOS oscillator and two 48 MHz clocks synthesized in the FPGA.

These are then further sub-divided to synthesize clocks for transfer and synchronization between peripheral boards and other functions, as shown in Fig. 4.16 and Fig. 4.17.

The triggering board connects to the FPGA development board via the Pmod connector. These are 2x6 right-angle, 100-mil female connectors that mate with standard 2x6 pin headers [11]. Each set of 12-pin connector comprise eight logic signals and a pair of 3.3V VCC and ground signals (4.18) [11]. Fig A.3 shows the connections.

Words from the triggering board are de-serialized from the parallel input ports in the FPGA via the implementation of a Finite State Machine (FSM). Once shifted in, a comparator is implemented, and

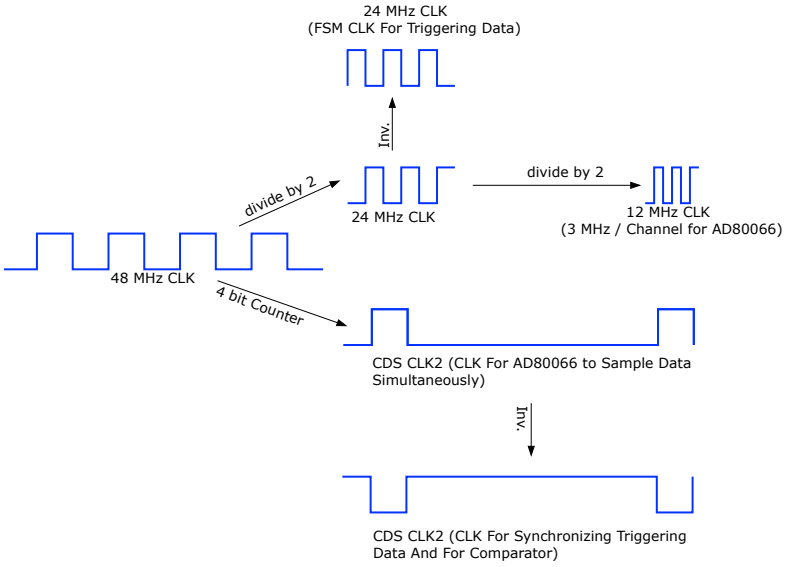

Fig. 4.16 Schematic illustrating synthesis of secondary triggering clocks from a 48 MHz clock.

Fig. 4.17 Synthesis of registry configuration and data transfer clocks from the 48 MHz clock.

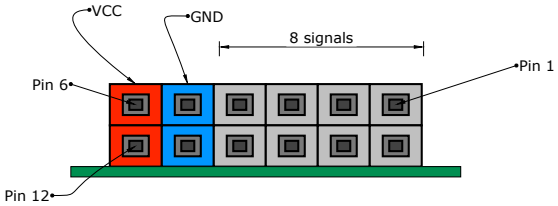

Fig. 4.18 Pmod connector with eight logic signals, two grounds and two 3.3V VCC per Pmod.

each channel triggers only if at least one of the following conditions are satisfied,

$$A > C \; and \; A > D \tag{4.3}$$

$$B > D \; and \; (B > A \; or \; B > C) \tag{4.4}$$

$$C > A \; and \; (C > B \; or \; C > D) \tag{4.5}$$

A	B	C	D	$(((\neg A) \wedge (\neg B)) \oplus ((\neg C) \wedge (\neg D))) \oplus ((B \wedge C) \oplus (\neg((B \wedge C) \vert (A \vee D))))$
0	0	0	0	0
0	0	0	1	1
0	0	1	0	1
0	0	1	1	1
0	1	0	0	1
0	1	0	1	0
0	1	1	0	1
0	1	1	1	0
1	0	0	0	1
1	0	0	1	0
1	0	1	0	0
1	0	1	1	0
1	1	0	0	1
1	1	0	1	0
1	1	1	0	0
1	1	1	1	0

Table 4.2 Truth Table for the four input channel triggering (see Fig. 4.9).

$$D > A \; and \; D > B \tag{4.6}$$

along with the Threshold condition,

$$A > Threshold \; or \; B > Threshold \; or \; C > Threshold \; or \; D > Threshold \tag{4.7}$$

which is imposed both for redundancy and also to ensure that no more than two channels initiate an event trigger. All four channels are assessed as given in the truth table in Tab. 4.2 and shown in Fig. 4.19.

A snapshot trigger used to measure ambient noise is also implemented on 0xFF clock cycles of the GPS Pulse Per Second (PPS) clock. A trigger can, for this reason, be registered either on a snapshot trigger or an event trigger based on the four channel comparator, as shown in Fig 4.20.

To support LVDS signaling, signals to the VHDC connector are routed as matched pairs with the corresponding fpga pins located in I/O bank0. These are powered at 2.5V [11]. There are twenty matched pairs of data signals, twenty ground signals, and eight power signals on the VHDC connector [11] (see Fig. 4.21).

The 200 MHz differential clock outputs from the High-Speed Board are brought into the FPGA and used in frequency synthesis. The DCM is configured to produce two clocks at 200 MHz from these input clocks (see Fig. 4.22).

The AD9634 ADC sends even/odd bits on the rising/falling edge of the sampling clock. A Double

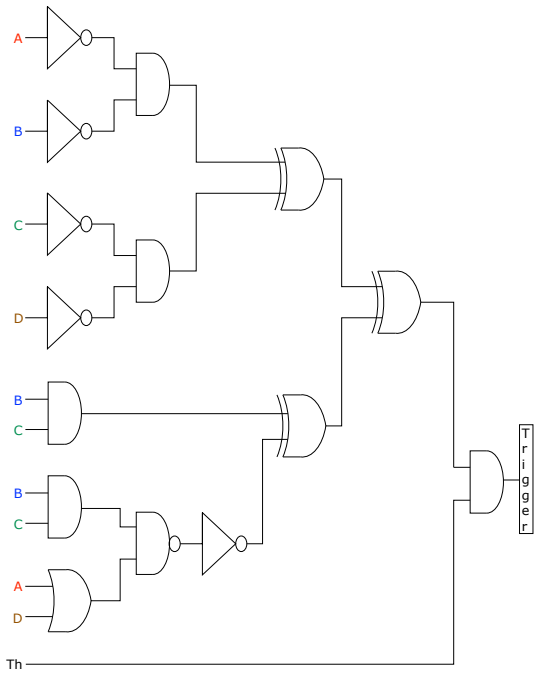

Fig. 4.19 Event triggering logic for the four input signals (A,B,C,D) and Threshold (Th).

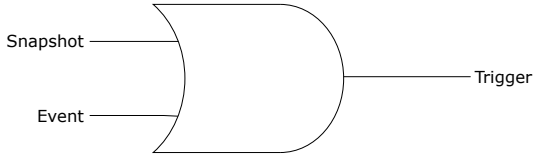

Fig. 4.20 Triggering logic for a comparator based event and a GPS PPS based snapshot trigger

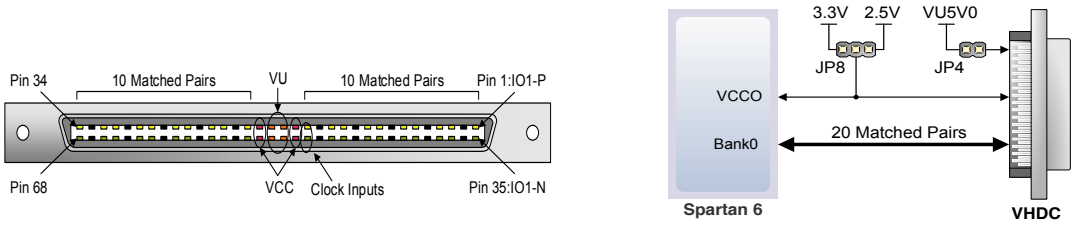

Fig. 4.21 Right: All FPGA pins routed to the VHDC connector are located in FPGA I/O bank0. Left: 40 data signals, 20 ground signals, and 8 power signals are found on the VHDC connector. Taken from [11].

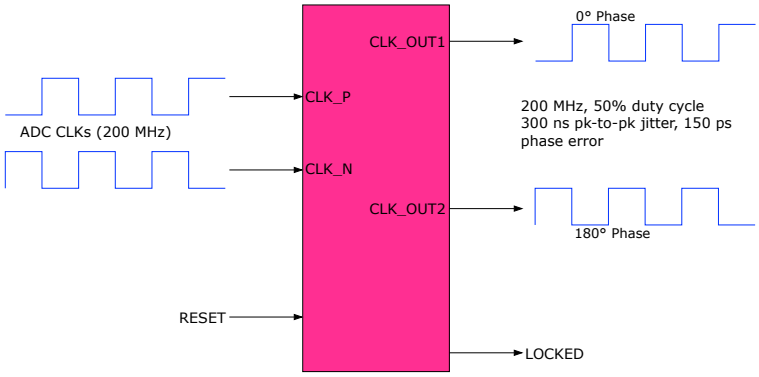

Fig. 4.22 High-Speed Board's 200 MHz differential clocks and subsequent FPGA synthesis of 200 MHz clocks.

Data Rate (DDR) interface [59] is used between the FPGA and the ADC, as illustrated in Fig. 4.23.

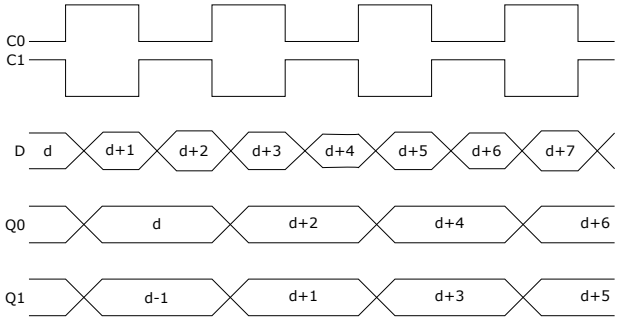

Fig. 4.23 Input Double Data Rate (IDDR2) is implemented to set even/odd bits on the clock rising/falling edge.

The bits are aligned per the C0 non-inverted clock, synthesized by use of an extra flip-flop as in Fig. 4.24.

Input BUFfer Differential Signaling (IBUFDS) is a differential I/O primitive [59] that is instantiated for the signals from the ADC and have two pins for the P and N channels of the differential signal (see Fig. 4.25).

Bits are then serialized via an FSM and then stored in a circular buffer. The buffer has Random Access Memory (RAM) depth of $2^{13}(8192)$ words and width of 16 bits. The actual width is 12 bits but padded with four bits (bits 0,7,8,15 are redundant). Buffer read/write operations are at 200 MSa/s. The Xilinx Block Memory Generator Wizard [60] generates the writing, reading and memory resources, where one 9K Block RAM (BRAM) and seven 18K BRAMs are used (see Fig. 4.26).

Once a trigger is received, the 16-bit words of $2^{13}(8192)$ bit depth are written into a First In First

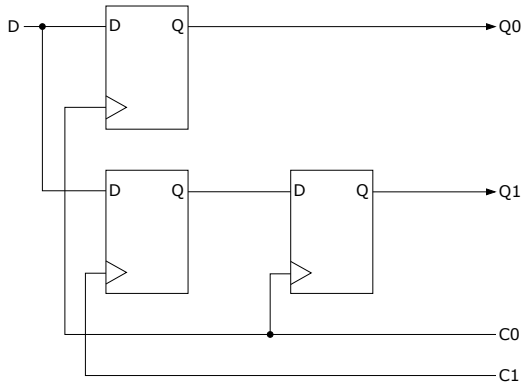

Fig. 4.24 IDDR2 when DDR alignment is C0.

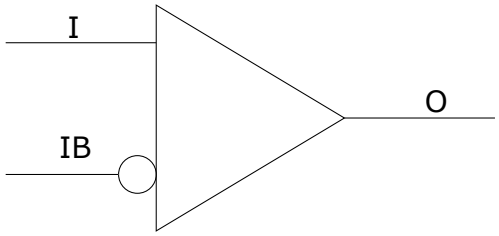

Fig. 4.25 Differential Input Buffer Primitive.

Out (FIFO) buffer at 200 MSa/s. The SBC reads the 8-bit words of $2^{14}(16384)$ bit depth at 8 MSa/s (SPI clock), i.e. it has a non-symmetric aspect ratio. The Xilinx FIFO Generator Wizard [61] instantiates the writing, reading and memory resources, where eight 18K BRAMs and First Word Fall Through (FWFT) are used (see Fig. 4.27).

Fig. 4.28 depicts the circular buffer to FIFO process.

In addition to the signal captured by the FPGA from the High-Speed Board, the Triggering information is also saved and forms the header of the data (see Fig 4.29). The header replaces the first 8 bits of raw data and subsequently invalidates the next 8 bits.

The SBC (Raspberry Pi rev 2.) sets the triggering threshold with transactions initiated using a different chip select line than the one activated once an interrupt is initiated on the FPGA side. This interrupt initiates when the FIFO buffer is full. However, due to latencies arising due to the crossing of clock domains in the FIFO, three synchronous D flip-flops as shown in Fig. 4.30 are instantiated after the assertion of full on the FIFO. An FSM controls the transfer logic between the FPGA and SBC.

In all transfers to/from the SBC(Master) and FPGA(Slave), an SPI clock at 8 MHz is used (see Fig. 4.31).

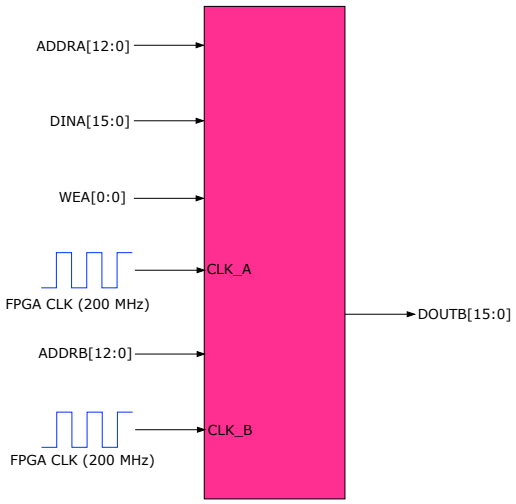

Fig. 4.26 Block Memory Signals.

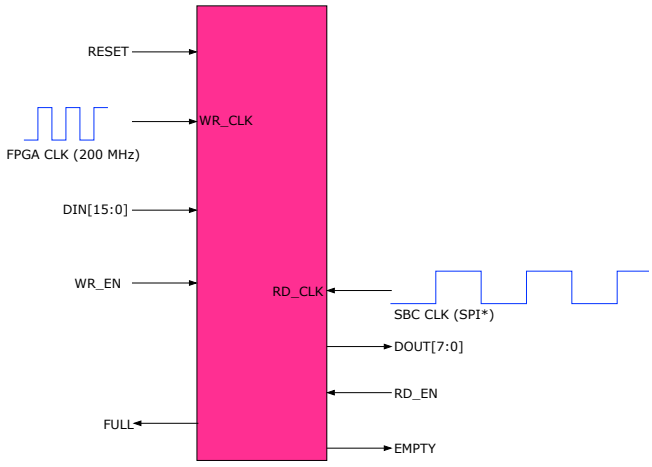

Fig. 4.27 FIFO Signals.

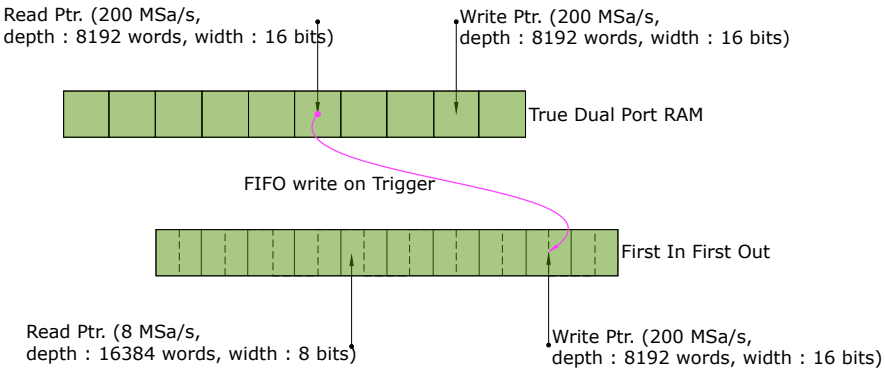

Fig. 4.28 Simple Dual Port RAM and FIFO Implementation

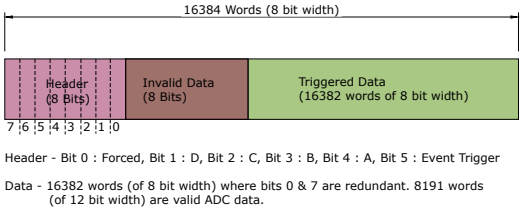

Fig. 4.29 Triggering Information and ADC Data.

4.4.4 GPS

The GPS unit (i-Lotus M12M) [62] is mounted on the Triggering Board for stability and power (see Fig A.3). A Universal Asynchronous Receiver/Transmitter (UART) is used to transfer data from/to the SBC. The GPS PPS is used as a counter to obtain snapshot triggers as described earlier in Sec. 4.4.3. Fig. 4.32 shows the Functional Block diagram of the GPS to SBC and FPGA connections.

Timing information is periodically queried from the GPS unit and used to update the time on the SBC.

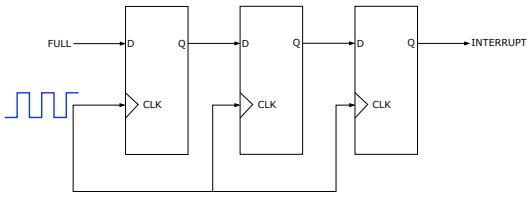

Fig. 4.30 Implementation of D Flip Flop to assert an Interrupt signal.

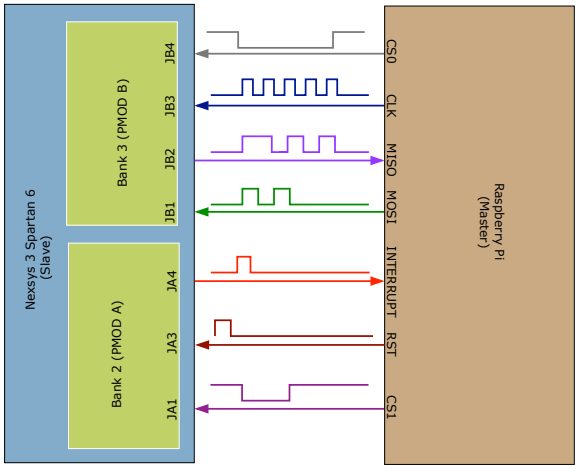

Fig. 4.31 FPGA - SBC Interface

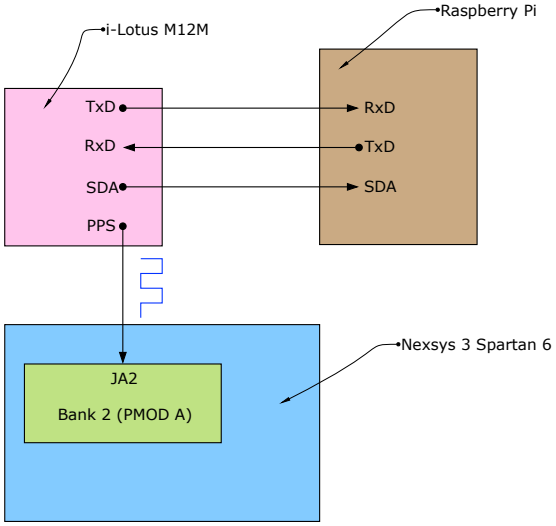

Fig. 4.32 GPS to FPGA and SBC Interface.

4.4.5 Single Board Computer (SBC)

The Single Board Computer used in the CAM is the commercially available Raspberry Pi Model B Rev. 2 (RPi - B Rev 2). The RPi has the Broadcom BCM2835 SoC (System on Chip) that includes the ARM1176JZF-S 700 MHz processor, VideoCore IV GPU, 512 MB RAM and access to other I/O peripherals, and a separate three port USB Hub [63] (see Fig 4.33).

The RPi has a 26 (2×13) pin 2.54 mm expansion header with 8 General Purpose Input/Output (GPIO) pins. It also has dedicated peripherals such as SPI, UART along with 3.3V, 5V and GND

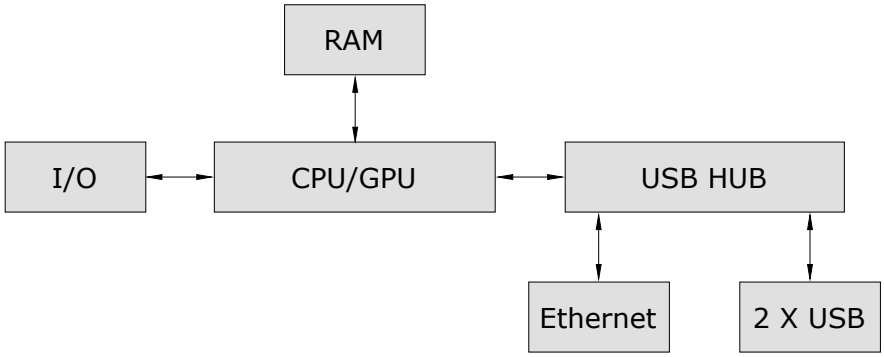

Fig. 4.33 Functional Block Diagram of the Raspberry Pi Model B Rev. 2

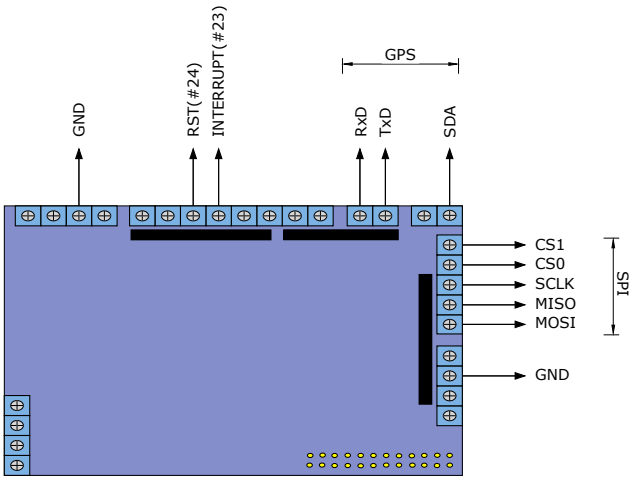

Fig. 4.34 Adafruit Prototyping Pi Plate showing the corresponding GPIO pins to FPGA and GPS

supply lines.

The board consists of a 32 GB SD card to which data are stored and also where a minimal Raspbian Wheezy (118 MB image) is compiled with hard float support (3.6.11+ hardfp kernel). WiringPi written in C for the BCM2835 provides access to the GPIO. The Adafruit Prototyping Pi Plate provides convenient pin access to connect with the FPGA and GPS (see Fig. 4.34).

4.5 System Monitoring and Powering

In addition to the CAM, the Remote Station comprises several components to power the station and monitor environmental variables. These components are the TDA Board, IVT Board, and the SHM. In the Summer of 2013, a prototype station comprising just these components had been deployed to

acquire environmental and powering information. In the current station, modifications were made, and the system was updated to integrate the CAM. A detailed description of the current powering and operational systems follow.

4.5.1 TDA

The TDA continuously monitors ambient noise at the site by counting threshold-crossings. The thresholds are set with Digital-to-Analog Converters that are remotely controlled through the System Health Monitor (SHM). The measurement period, usually 10 seconds, is also controlled by the SHM. Fig. 4.35 shows a functional block diagram of the TDA. The TDA communicates via the Local Interconnect Network (LIN) bus, designed with the robustness needed for automobile environments.

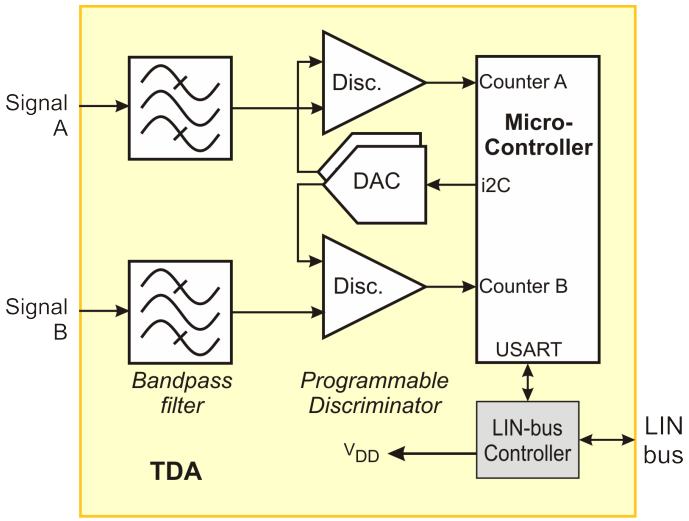

Fig. 4.35 Transient Detector Apparatus (TDA). *Courtesy Kenneth Ratzlaff, Instrumentation Design Lab, KU.*

4.5.2 IVT Board

The IVT board provides power measurements to monitor the Photo-Voltaic (PV) battery-charging system. Voltage and current are measured for both the PV power input and the Load power output (Fig. 4.36). On the board, a temperature sensor is located to enable correction for the current sensors. Heavy screw lugs accommodate the heavy cables that are required for currents that typically reach 10 Amps. As was the case for the TDA, a micro-controller provides analog-to-digital conversion, averages over the measurement period and communicates with the SHM over the LIN bus.

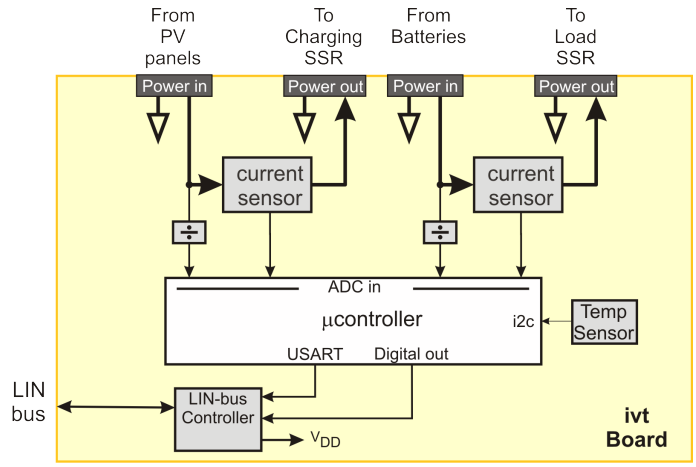

Fig. 4.36 Current Voltage Temperature (IVT) Board. *Courtesy Kenneth Ratzlaff, Instrumentation Design Lab, KU.*

4.5.3 SHM

The SHM has the functions of reporting on the environmental and operational status of the system and of controlling the charging of the batteries (Fig. 4.37). The SHM gathers ambient noise data from the TDA and power data from the IVT over a period that is programmable from 5 seconds to at least 10 minutes. Similarly, it measures the battery voltage using the ADC on the micro-controller. A real-time clock with battery backup provides a time-stamp for each measurement cycle.

The SHM also controls the charging of the battery. A high-current solid-state relay (SSR) can switch PV current off when the battery reaches capacity, and another SSR is used to turn the load off if the battery voltage is too low. As illustrated in Fig. 4.38, hysteresis levels minimize oscillations. The thresholds are remotely programmable. If, however, the voltage level becomes too low, the communications channel also shuts down until the battery becomes sufficiently charged.

Data are stored on board using an SD card and are also sent to a communication channel. An Ethernet appliance provides both raw TCP connection and a website. The data are streamed via the raw TCP port, and the website provides a data display and interactive control of operational variables including the battery charging thresholds, the TDA thresholds, the measurement period, and calibration values.

4.6 Chirp Calibration Unit (CCU)

In order to calibrate the remote stations independently, a Chirp Calibration Unit has been deployed in the field. Fig. 4.39 shows this unit that comprises a 'fat - dipole', an Arduino with a monostable 555

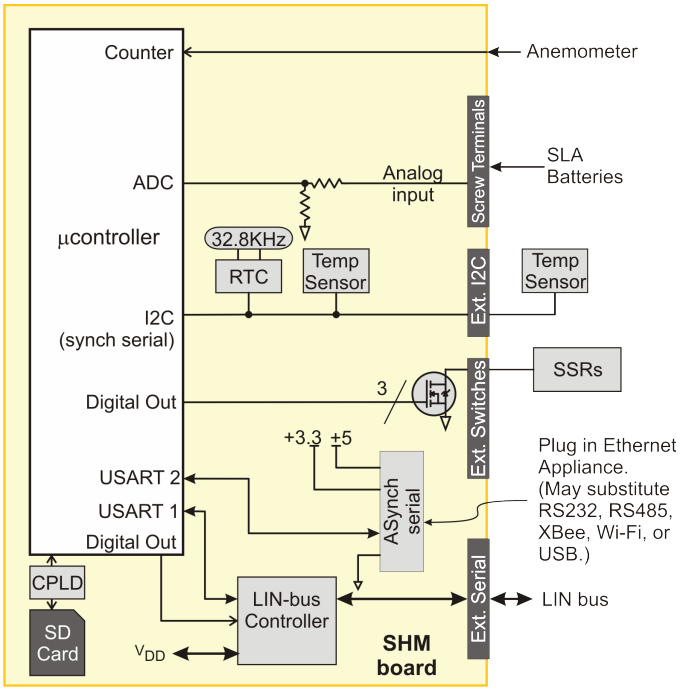

Fig. 4.37 System Health Monitor (SHM). *Courtesy Kenneth Ratzlaff, Instrumentation Design Lab, KU.*

circuit, and a signal generator (SF1020). The output of the control circuit controls an SSR, which in turn then triggers the signal generator. Fig. A.5 shows the control circuit for the chirp generator.

The dipole is tuned to a frequency of 70 MHz, however, in order to transmit a broadband chirp-like signal the radius of the dipole was optimized to transmit efficiently up to 50 MHz. Stable chirps at 1 PPS, spanning 80 to 50 MHz and of a 20 μs duration every 2 hours for 10 seconds, i.e., ten chirp signals, are produced.

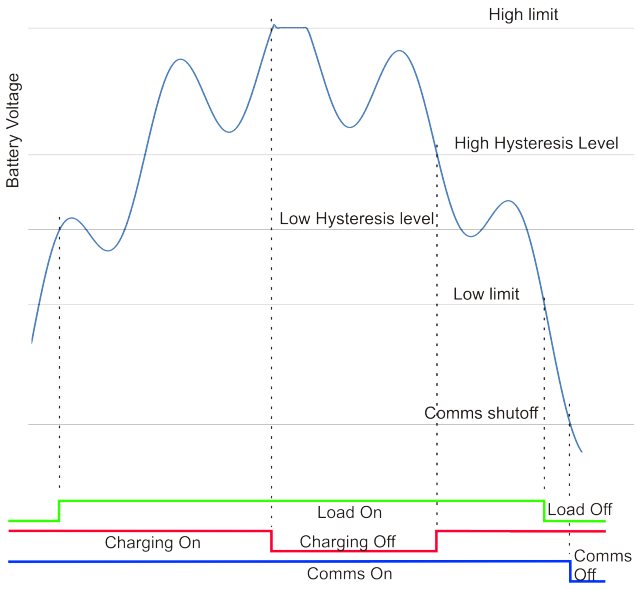

Fig. 4.38 Threshold Settings on the System Health Monitor (SHM).

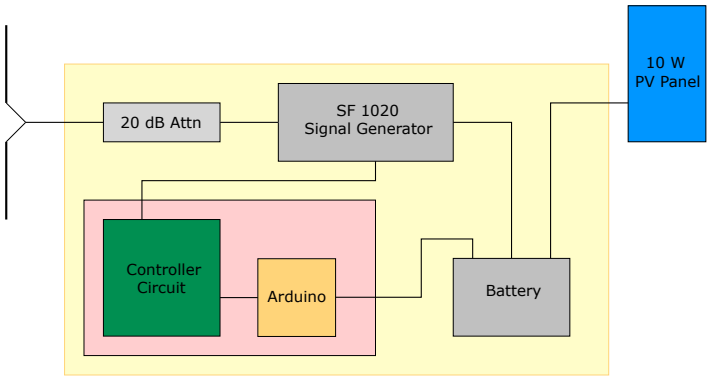

Fig. 4.39 Schematic of the Chirp Calibration Unit (CCU) *Courtesy Steven Prohira, Dept. of Physics and Astronomy, KU.*

Chapter 5

TARA Remote Station Detection of UHECR's

In this chapter, we discuss measurements taken using the Telescope Array Radar Remote Stations.

5.1 Snapshot Triggers

It is essential to understand the environment into which an observable cosmic ray may be embedded. As mentioned previously, this was accomplished using snapshot triggers with the station prototype, deployed in 2013. Snapshot triggers are taken every 255 seconds to sample the ambient noise at the remote station location. These triggers are instantiated after 255 continuous pulses from the GPS clock pulsing at 1 PPS. Since these snapshot triggers are unassociated with actual high-amplitude backgrounds, they offer the opportunity to probe otherwise weak, but constant radio-frequency signals, such as that of the Milky Way.

As the Earth rotates, the location of the Galactic center relative to the antenna heading (78° East of North) changes, leading to a smooth variation in the measured noise floor. This variation is depicted in Fig. 5.1, where both a fit to the measured signal centered at 70 MHz over a 5 MHz wide band is superimposed along with the expected modulation by the Galactic Center on the measured signal at 70 MHz. We observe an apparent correlation in the phase of the known Galactic motion with bore-sight of the receiver antennas, indicating good sensitivity to otherwise-weak signals. The measurements made were taken from the horizontally polarized channel during the period from the 1^{st} to the 14^{th} of December, 2014.

The behavior is seen at other frequencies as shown in Fig. 5.2. Here the relative angle is the difference between the azimuthal angle of the galactic center and the heading of the TARA LPDA.

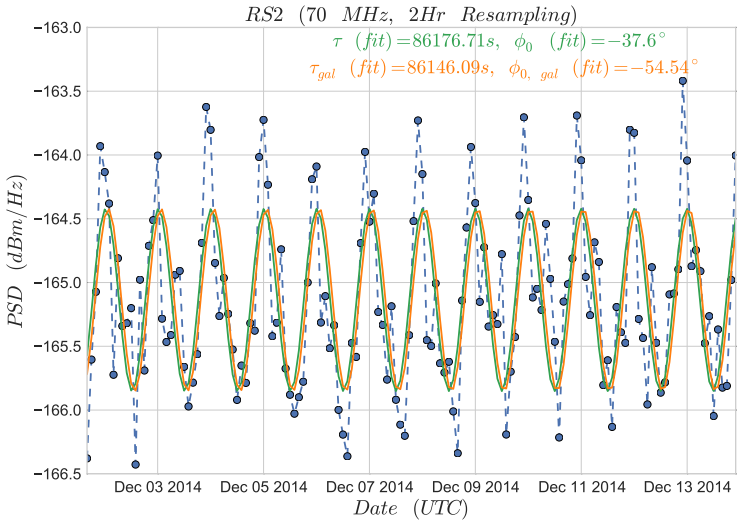

Fig. 5.1 Modulation of the RS2 antenna at 70 MHz. The green line is a least squares fit to the measured power while the orange line is a least squares fit to the expected modulation due to the galactic center, chosen to be Sagittarius A*. The measurements were taken from the horizontally polarized channel.

The measured noise level of Remote Station 2 superimposed on the expected Galactic noise floor is shown in Fig. 5.3. The measurement again confirms that the Remote Stations are functioning well enough to observe a high-energy cosmic ray if our putative radar model is correct.

5.2 Expected Event Rate

To quantify our expected signal event rate using the technique of radar reflections, an extensive library of CORSIKA simulated showers were generated to calculate the lengths and radii of plasma. These were estimated based on the energy deposited by the showers and the subsequent ionization electron density in Chapter 2. Determining the RCS of a thin wire at various angles and obtaining the received power from the bi-static radar equation using numerous locations within the baseline provides a distribution of RCS vs. received chirp power. Given the TARA geometry and detector design the efficiency for $\geq 10^{19}\ eV$ has been calculated to be $\sim 10\%$ based on the cumulative distribution function shown in Fig. 5.4. Here a cut was made at 0 dB SNR based on the received signal power relative to the receiver noise floor.

Fig. 5.5 shows the expected integrated event rate for the TARA Remote Station volume from 10 to 100 EeV. Here, we take $dN/dE/dt/d\Omega$ from the Telescope Array measurements and take into account the efficiency of the detector and the flux of UHECR.

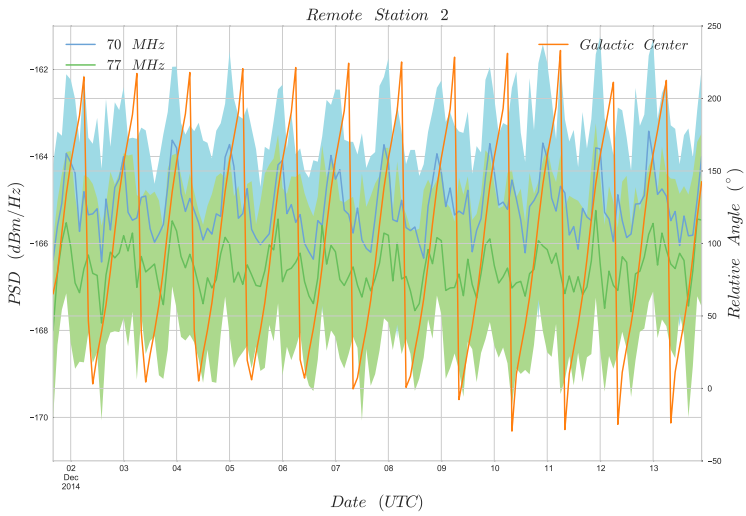

Fig. 5.2 Modulation of the RS2 antenna at 70 MHz and 77 MHz. The orange line is a least squares fit to the expected modulation due to the galactic center, chosen to be Sagittarius A*. The measurements were taken from the horizontally polarized channel.

5.3 Calibration Events

The Chirp Calibration Unit (CCU) generates ten chirps every 2 hours. These chirps span from 80 to 50 MHz in 20 μs for an average slope of 1.5 $MHz/\mu s$. The calibration unit was placed $\sim$ 140 ft from the two remote stations and subsequently used to trigger them. Fig. 5.6 shows the spectrogram of such a chirp.

During the period from 20^{th} to the 24^{th} of January, 2015, both force-triggered and self-triggered events were collected by the CAM. The CAM tags an event as either a force-triggered or self-triggered event based on the header information received. The events during this period classified as such are shown in the SNR vs. Chirp-rate plot in Fig. 5.7.

The SNR here is the ratio of the maximum signal power of an event to the RMS of noise collected in the last 10μs of the event, so as to prevent signal contamination. The chirp rate is calculated using the "de-chirping" algorithm described earlier, namely by taking the product of the signal with a delayed copy of itself. The delay was chosen to be 1 μs, and the bin with the maximum signal power below 20 $MHz/\mu s$ was selected to obtain the chirp rate for the event. The CCU triggered events are clearly identifiable as a $\sim$ 1.48 $MHz/\mu s$ line in the plot ranging from a SNR of $\sim$ 25 to 30 dB. However, the forced triggered data also has comparable SNR due to interference from the Transmitter signal at 54.1 MHz. Applying a 5th order Butterworth bandpass filter (58 - 82 MHz) as shown in Fig. 5.8 mitigates the problem, clearly indicating the need for further carrier attenuation at 54.1 MHz as part of future upgrades.

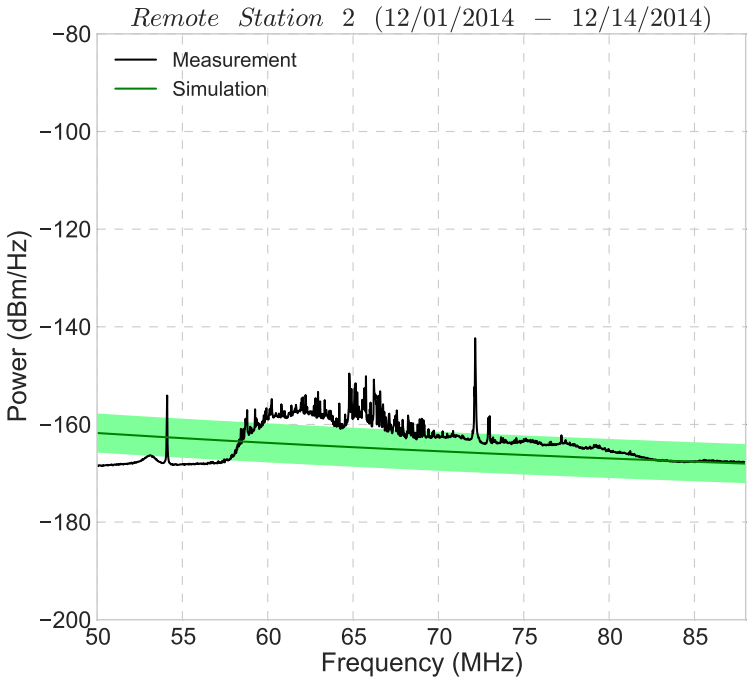

Fig. 5.3 The measured noise floor of the TARA LPDA using the Remote Station 2 DAQ, with the expected noise floor superimposed (primarily galactic at these energies). The measurements made were taken from the horizontally polarized channel.

5.4 Constraints on the Radar Cross Section

In the case, that there are no cosmic ray detections, we have investigated our numerical sensitivity to the radar cross-section. The efficiency of the TARA detector can be folded into the known TA flux of UHECR such that, for a 90% C.L, the upper limit on the Radar Cross Section (σ_{limit}) can be obtained from $\sigma_{limit} = \sigma_{pred} \times \frac{Events\ Observed}{Events\ Expected}$, where σ_{pred} is the expected RCS, *Events Observed* are the number of cosmic ray events detected by the Remote Station and *Events Expected* are the number of events expected accounting for detector inefficiencies. Fig. 5.9 shows the RCS limit assuming a particular number of events detected for a live time of 1 year.

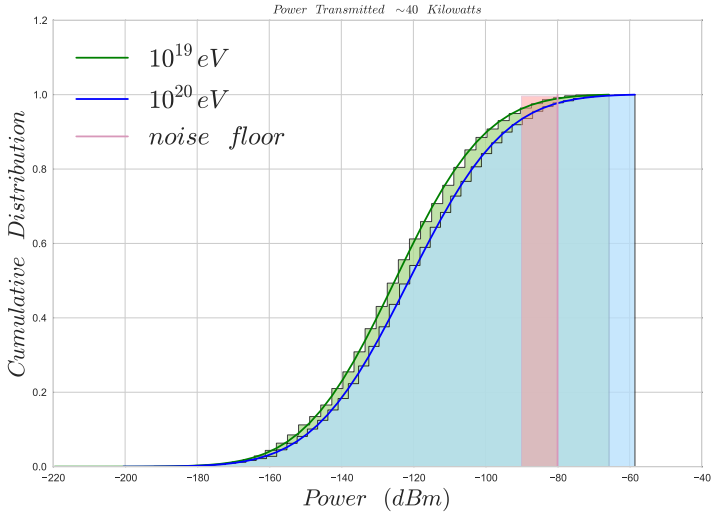

Fig. 5.4 The cumulative distribution function for the TARA remote station receivers for an ensemble of Monte Carlo CORSIKA-simulated events at 10^{19} *eV* (green) and 10^{20} *eV* (blue). The pink band indicates a bandwidth of 24 MHz up to 200 MHz. Cuts at 0 dB SNR are made on the received signal relative to the receiver noise floor, assuming this is our future operational threshold.

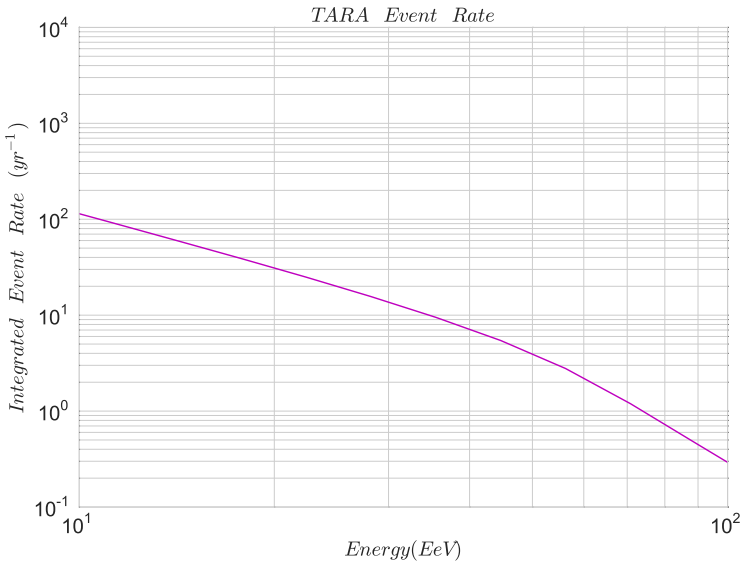

Fig. 5.5 The expected integrated TARA remote station event rate based on the procedure described in the text.

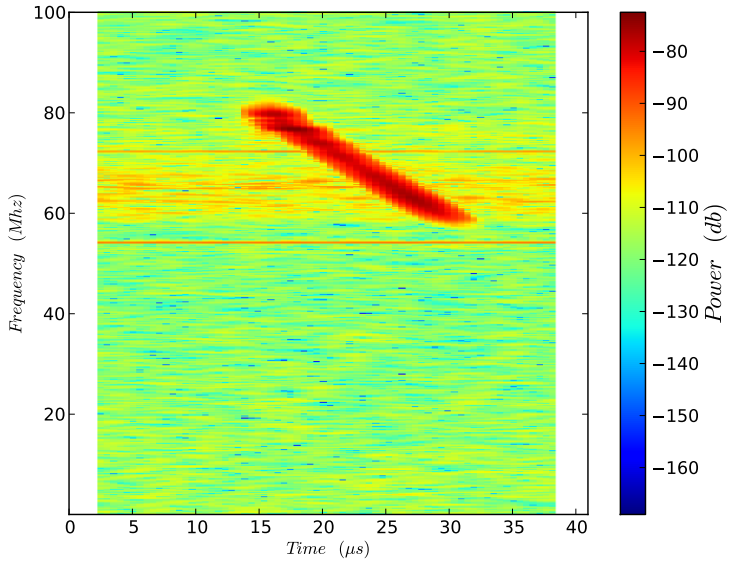

Fig. 5.6 Remote Station triggered chirp (data). Calibration chirp sent from CCU in the field.

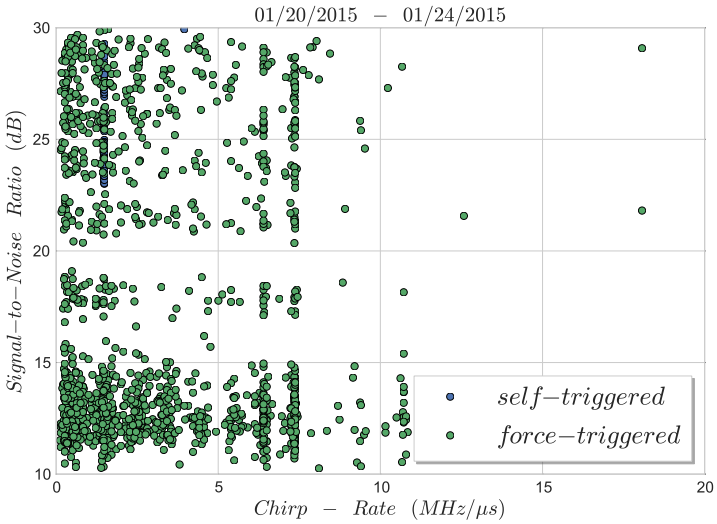

Fig. 5.7 Self and force-triggered events during the period from 20^{th} to the 24^{th} of January, 2015 for RS2, prior to software-filtering contamination by the carrier at 54.1 MHz.

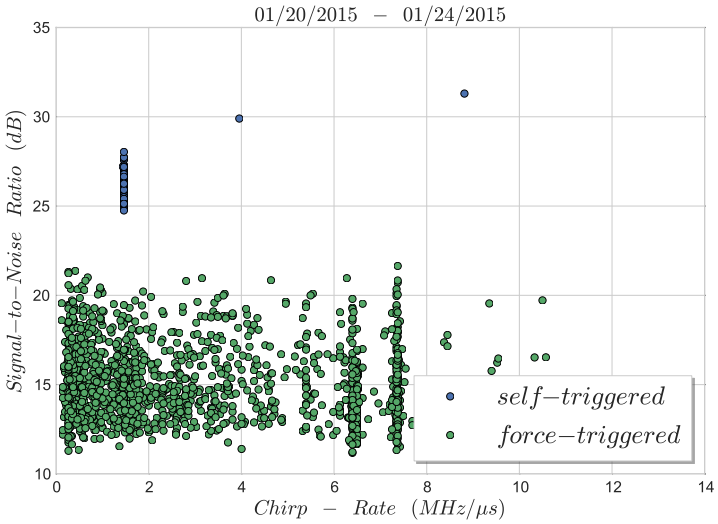

Fig. 5.8 Self and Force-triggered events during the period from the 20^{th} to the 24^{th} of January, 2015 for RS2 after passing through a 5th order Butterworth bandpass filter (58 to 82 MHZ) to suppress out-of-band noise.

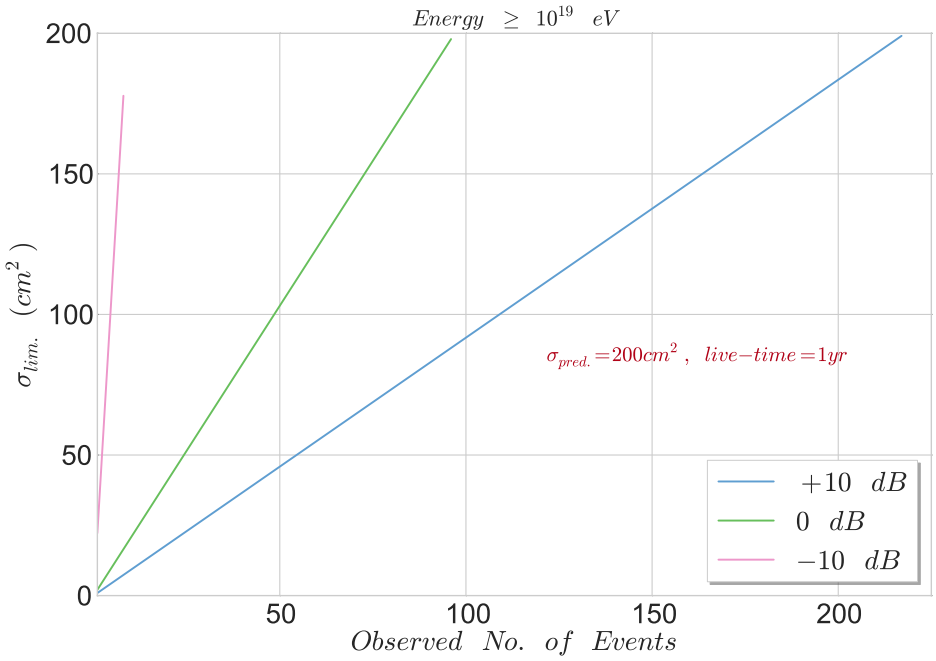

Fig. 5.9 The Radar Cross Section limit given a certain number of observed events.

Chapter 6 Conclusion

Conclusion

The Telescope Array RAdar (TARA) detector is an ambitious project based on a remote sensing technique known as bistatic radar that aims to probe large portions of the Earth's surface in the quest to measure cosmic ray induced radio echoes. Together with the Telescope Array in radio-quiet western Utah, TARA's pilot receiver and transmitter stations were deployed in 2011. This initial deployment gave us insight into the detectability of air shower radar echoes. The receiver stations comprised an array of Log Periodic Dipole Antennas. An oscilloscope-based data acquisition system was implemented for noise calibration, including tracking galactic noise as the galactic plane migrates through the sky. That experience laid the foundation for upgrades, including the construction of a dedicated transmitter station in the summer of 2013 and deployment of additional remote receiver stations.

A prototype remote station was deployed in March of 2013, and for a period of one year collected invaluable data regarding power budgeting and the ambient noise conditions in the Utah desert. These results led to the eventual deployment of the first Remote Station in June of 2014 and was upgraded via the addition of a second station in November of the same year.

At the core of these stations, an FPGA-embedded system provides logic for triggering and storing raw data sampled at 200 MSa/s. These stations reduce costs relative to off-the-shelf commercial options and add stereoscopic measurement capabilities for UHECR events.

In mid-January of 2015 a Chirp Calibration Unit was installed, and the detection of transmitted chirps have demonstrated the working principle of the Remote Stations. Valuable insight has been gained for future improvements on these stations including improvement in timing resolution for stereoscopic measurements. Going forward, data taken for a live-time of the order of months may eventually provide sufficient statistics to answer some of the most intriguing questions in our Universe. Understanding the composition, anisotropy and energy of particles continuously bombarding Earth will ultimately lead to an understanding of the most violent processes in the Cosmos.

Astroparticle physics, at the intersection of astronomoy, cosmology and particle physics has a continuosly changing landscape. The TARA project implements a novel technique to detect cosmic ray chirps and similar techniques are being proposed to detect cosmic neutrinos [64]. The remote stations implementation for the detection of chirp signals may prove to be useful in similar applications.

References

[1] Hanlon, W., 2014. URL `http://www.physics.utah.edu/~whanlon/spectrum.html`.

[2] J.W. Cronin. The highest energy cosmic rays. *Nucl. Phys. Proc. Suppl.*, 138:465–491, 2005.

[3] Neto, J. (for the Pierre Auger Collaboration). Anisotropy studies with the pierre auger observatory. *J. Phys.: Conf. Ser.*, 409 012108, 2013.

[4] Aab, A. et al. Searches for anisotropies in the arrival directions of the highest energy cosmic rays searches for anisotropies in the arrival directions of the high energy cosmic rays detected by the pierre auger observatory. *arXiv:1411.6111 [astro-Ph.HE]*, 2014.

[5] Abbasi, R.U et al. Indications of intermediate-scale anisotropy of cosmic rays with energy greater than 57 eev in the northern sky measured with the surface detector of the telescope array experiment. *ApJ*, 790(2), 2014.

[6] Kachelreiss, M. Lecture notes on high energy cosmic rays. *arXiv:0801.4376 [astro-Ph]*, 2008.

[7] Stasielak, J. et al. Feasibility of radar detection of extensie air showers. *arXiv:1411.7295 [astro-ph.IM]*, 2014.

[8] Bugallo, M.F. et al. Mariachi : A multidisciplinary effort to bring science and engineering to the classroom. *IEEE International Conference on Acoustics, Speech and Signal Processing.*, pages 2661–2664, 2008.

[9] Abbasi, R.U et al. Telescope Array Radar (TARA) observatory for ultra-high energy cosmic rays. *Nucl. Inst. and Meth. in Phys. Research, A*, 767:322–338, 2014.

[10] G. Burke and A. Poggio. Numerical electromagnetic code (nec) method of moments, parts i, ii, iii. Technical report, Lawrence Livermore National Laboratory, NEC-1 (1977), NEC-2 (1981), NEC-3 (1983).

[11] Digilent. *Nexsys3*, 2014. URL `http://www.digilentinc.com/Data/Products/NEXYS3/Nexys3_rm_V2.pdf`.

[12] Hess, V. F. uber beobachtungen der durchdringenden strahlung bei sieben freiballonfahrten. *Physikalische Zeitschrift*, 13:1084, 1912.

[13] Smida, R. *Cosmic-Ray Physics with the Pierre Auger Observatory*. PhD thesis, Charles University in Prague, 2009.

[14] Millikan, R. A. and Cameron, G. H. High frequency rays of cosmic origin iii. measurements in snow-fed lakes at high altitudes. *Phys. Rev.*, 28(851), 1926.

[15] Hoerandel, J.R. Models of the knee in the energy spectrum of cosmic rays. *Astropart. Phys.*, 21: 241–265, 2004.

[16] Khan, E. et al. Photodisintegration of ultra-high-energy cosmic rays revisited. *Astropart. Phys.*, 23(2):191–201, 2005.

[17] Barnhill, D.S. *Composition Analysis of Ultrahigh Energy Cosmic Rays Using the Pierre Auger Composition Analysis of Ultra High Energy Cosmic Rays Using the Pierre Auger Observatory Surface Detector*. PhD thesis, UCLA, 2005.

[18] Greisen, K. End of the cosmic-ray spectrum? *Phys. Rev. Lett.*, 16(17):748–750, 1966.

[19] Zatespin, G. T. et al. Upper limit of the spectrum of cosmic rays. *J. of Exp. and Theor. Phys. Lett.*, 4:78–80, 1966.

[20] Stanev, T. *High Energy Cosmic Rays*. Springer, 2003.

[21] Bergstrom, L. and Goobar, A. *Cosmology and Particle Astrophysics*. Springer, 2006.

[22] Bird, D. J. et al. Evidence for correlated changes in the spectrum and composition at extremely high energies. *Phys. Rev. Lett.*, 71(21), 1993.

[23] Boghrat, P. *Search for Ultra High Energy Cosmic Ray Anisotropy with Auger*. PhD thesis, UCLA, 2007.

[24] Dolag, K. et al. Mapping deflections of extragalactic ultra-high energy cosmic rays in magneto-hydrodynamic simulations of the local universe. *JETP Lett.*, 79:583–587, 2004.

[25] Aglietta, M. et al. Anisotropy studies around the galactic centre at eev energies with the auger observatory. *Astropart. Phys.*, 27:244, 2007.

[26] Ajello, M. et al. The 60 month all-sky burst alert telescope survey of active galactic nucleus and the anisotropy of nearby agns. *ApJ*, 749(21), 2012.

[27] Kotera, K. and Olinto, A. The astrophysics of ultrahigh-energy cosmic rays. *Annu. Rev. Astron. Astrophys.*, 49:119–153, 2011.

[28] Apel, W.D et al. The spectrum of high-energy cosmic rays measured with KASKADE-Grande. *Astropart. Phys.*, 36:183–194, 2012.

[29] Abreu, P. et al. Measurement of the proton-air cross section at 57 tev with the pierre auger observatory. *Phys. Rev. Lett.*, 109, 2012.

[30] Abraham, J. et al. Measurement of the depth of maximum measurement of the depth of extensive air showers above 1018 ev. *Phys. Rev. Lett.*, 104, 2010.

[31] Abbasi, R.U et al. Study of ultra-high energy cosmic ray composition using telescope array's middle drum detector and surface array in hybrid mode. *arXiv:1408.1726 [astro-ph.HE]*, 2014.

[32] Lemoine, M and Waxman, E. Anisotropy vs chemical composition at ultra high energies. *J. Cosmol. Astropart.*, 11:9, 2009.

[33] Auger, P. et al. Extensive cosmic-ray showers. *Rev. Mod. Phys.*, 11:288–291, 1939.

[34] Gaisser, T.k. and Hillas, A.M. Reliability of the method of constant intensity cuts for reconstructing the average development of vertical showers. *15th Int. Cosmic Ray Conf.*, 8:353, 1977.

[35] Ostapchenko, S. Qgsjet - ii : towards reliable description of very high energy hadronic interactions. *Nucl. Phys. B - Proc. Suppl.*, 151(1):143–146, 2005.

[36] Heck, D. et al. CORSIKA : A monte carlo code to simlate extensive air showers. Technical report, Karlsruhe Institute of Technology, 1998.

[37] Brau, C. A. *Modern Problems In Classical Electrodynamics*. Oxford University Press, 2004.

[38] Takai, H. et al. Forward scattering radar for ultra high energy cosmic rays. In *32nd International Cosmic Ray Converence*, 2011.

[39] Gorham, P. On the possibility of radar echo detection of ultra-high energy cosmic ray- and neutrino-induced extensive air showers. *Astropart. Phys.*, 15:177–202, 2001.

[40] Vidmar, R.J. On the use of atmospheric pressure plasmas as electromagnetic reflectors and absorbers. *IEEE. Transactions On Plasma Science*, 18(4):733 – 741, 1990.

[41] Schneider, B.I and Brau, C. A. Two- and three-body electron attachment in air. *Journal of Physics B: Atomic and Molecular Physics*, 15(10):1601, 1982.

[42] Neunteufel, P. et al. Microwave emission due to molecular bremsstrahlung in non-thermal air shower plasmas. In *33rd International Cosmic Ray Conference*, 2013.

[43] Dyrud, Lars P et. al. The anamolous diffusion of meteor trails. *Geophysical Research Letters*, 28: 2775–2778, 2001.

[44] Blackett, P.M.S and Lovell, A.C.B. Radio echoes and cosmic ray showers. *Proceedings of the Royal Society A: Mathematical, Physical and Engineering Sciences*, 177(969):183, 1941.

[45] Lovell, F.R.S. The blackett-eckersley-lovell correspondence of world war ii and the origin of jodrell bank. *Rec. R. Soc. Lond.*, 47(1):119–131, 1993.

[46] Crispin, J. W. and Maffett, A. L. Radar cross - section estimation for simple shapes. *Proc. of IEEE*, 8:833–848, 1965.

[47] Bakunov, M.I. et al. Relativistic effects in radar detection of ionization fronts produced by ultra-high energy cosmic rays. *Astropart. Phys.*, 33:335–3040, 2010.

[48] Stasielak, J. et al. Enhancement of the radar signal of air showers due to time compression. *arXiv:1310.0743 [astro-ph.HE]*, 2013.

[49] Constantine A. Balanis. *Antenna Theory Analysis and Design*. Wiley - Interscience, 2005.

[50] W.C. Gibson. *The Method of Moments in Electromagnetics*. Chapman and Hall, 2008.

[51] J.D Kraus and R.J Marhefka. *Antennas*. McGraw - Hill, 2003.

[52] Hanson, J. *The Performance and Initial Results of the ARIANNA Prototype*. PhD thesis, University of California Irvine, 2013.

[53] G.A Dulk, et. al. Calibration of low-frequency radio telescopes using the galactic background radiation. *Astron. Atrophys.*, 365:294–300, 2001.

[54] H.V. Cane. Spectra of the non-thermal radio radiation from the galactic polar regions. *Mon. Not. R. Astron. Soc.*, 189, 1979.

[55] Zaino, J.C. et al. An fpga based adaptive computing implementation of chirp. In *Military and Aerospace Applications of Programmable Devices and Technologies (MAPLD)*, 1999.

[56] Envelope detector. URL `http://seniord.ee.iastate.edu/SSOL/RADAR/prjpln99/detector3.html`.

[57] Analog Devices. *AD80066*, Oct 2014. URL `http://www.analog.com/static/imported-files/data_sheets/AD80066.pdf`.

[58] Analog Devices. *AD9634*, Oct 2014. URL `http://www.analog.com/static/imported-files/data_sheets/AD9634.pdf`.

[59] Xilinx. *Spartan-6 FPGA SelectIO Resources*, 1.6 edition, Feb 2014. URL `http://www.xilinx.com/support/documentation/user_guides/ug381.pdf`.

[60] Xilinx. *Spartan-6 FPGA Block RAM Resources*, 1.5 edition, Jul 2011. URL `http://www.xilinx.com/support/documentation/user_guides/ug383.pdf`.

[61] Xilinx. *LogiCORE IP FIFO Generator*, 9.2 edition, Jul 2012. URL `http://www.xilinx.com/support/documentation/ip_documentation/fifo_generator/v9_2/pg057-fifo-generator.pdf`.

[62] i Lotus. *i-lotus M12M*, Feb 2008. URL `http://www.ilotus.com.sg/sites/all/themes/zeropoint/pdf/m12m/M12M%20Timing%20-%20TDS%20(Ver%201.0.0).pdf`.

[63] Lantronix xpico wi-fi pi plate for raspberry pi, Oct 2014. URL `http://www.lantronix.com/news/2014/10-08_lantronix-xpico-wi-fi-pi-plate-for-raspberry-pi-now-shipping-worldwide.html`.

[64] de Vries, et al. On the feasibility of RADAR detection of high-energy induced showers in ice. *Astropart. Phys.*, 60:25–31, 2015.

Appendix A

Schematics

CAM

Fig. A.1 shows the schematics of the power supply board for the CAM.

Triggering Board

Fig. A.2 shows the schematics of the Triggering board including the bandpass filters, envelope detectors and the ADC.

Fig A.3 shows the connections between the FPGA, SBC and the GPS and Triggering Board.

High Speed Board

To provide superior common-mode noise rejection differential signalling is used and the 12-bit words are transferred using a custom adapter (Fig. A.4) between the Evaluation Board's LVDS (Low Voltage Differential Signalling) parallel output port and the VHDC (Very High Density Cable) connector on the FPGA.

Chirp Calibration Unit (CCU)

To clibrate the remote station a chirp calibration unit was deployed at the station location. Fig. A.5 shows the control circuit for the chirp generator.

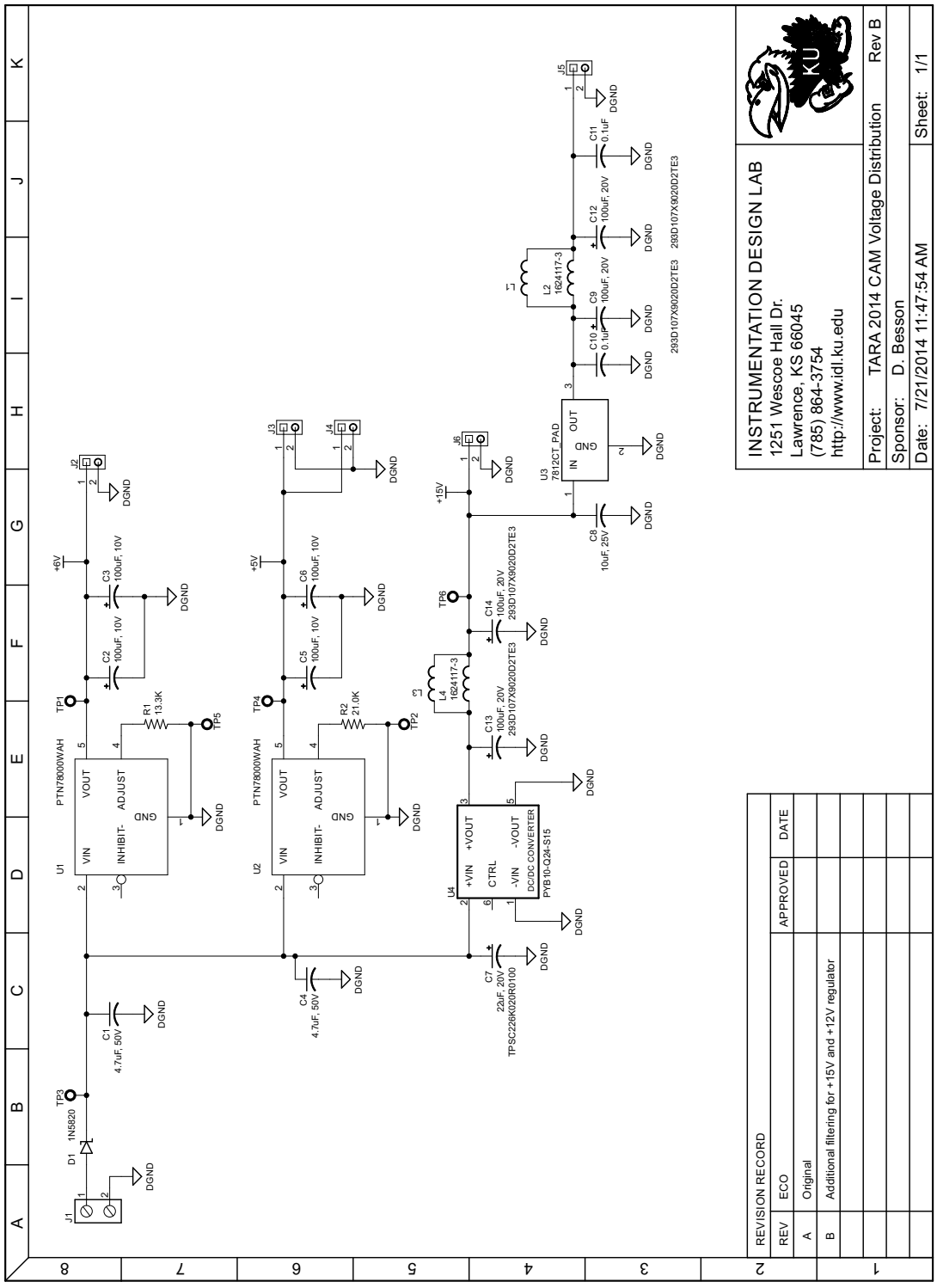

Fig. A.1 Details of the power supply board for the CAM. *Courtesy Rob Young, Instrumentation Design Lab, KU.*

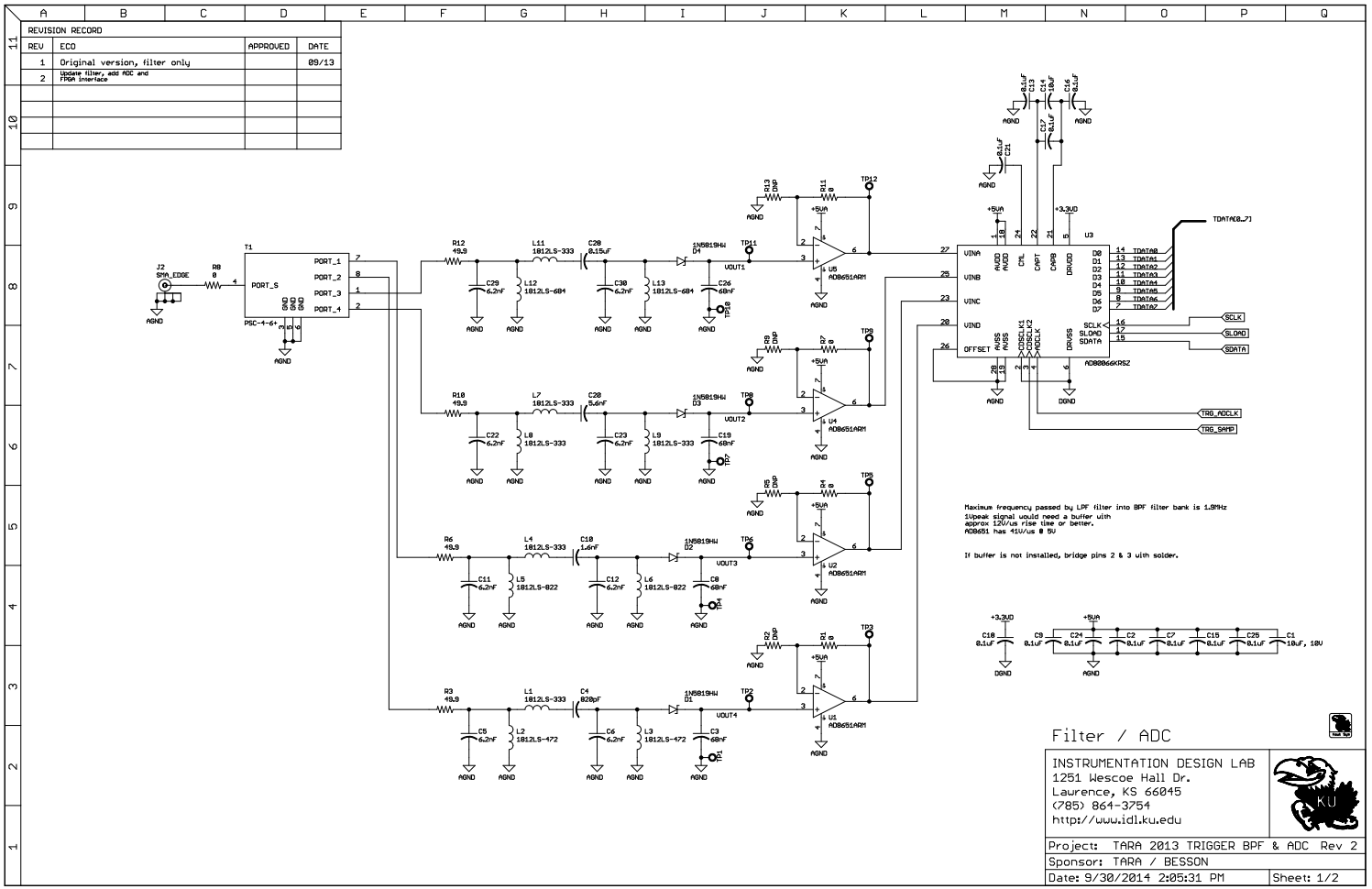

Fig. A.2 Details of the Band-Pass-Filters, Envelope Detectors and the ADC (AD 80066, Analog Devices). *Courtesy Rob Young, Instrumentation Design Lab, KU.*

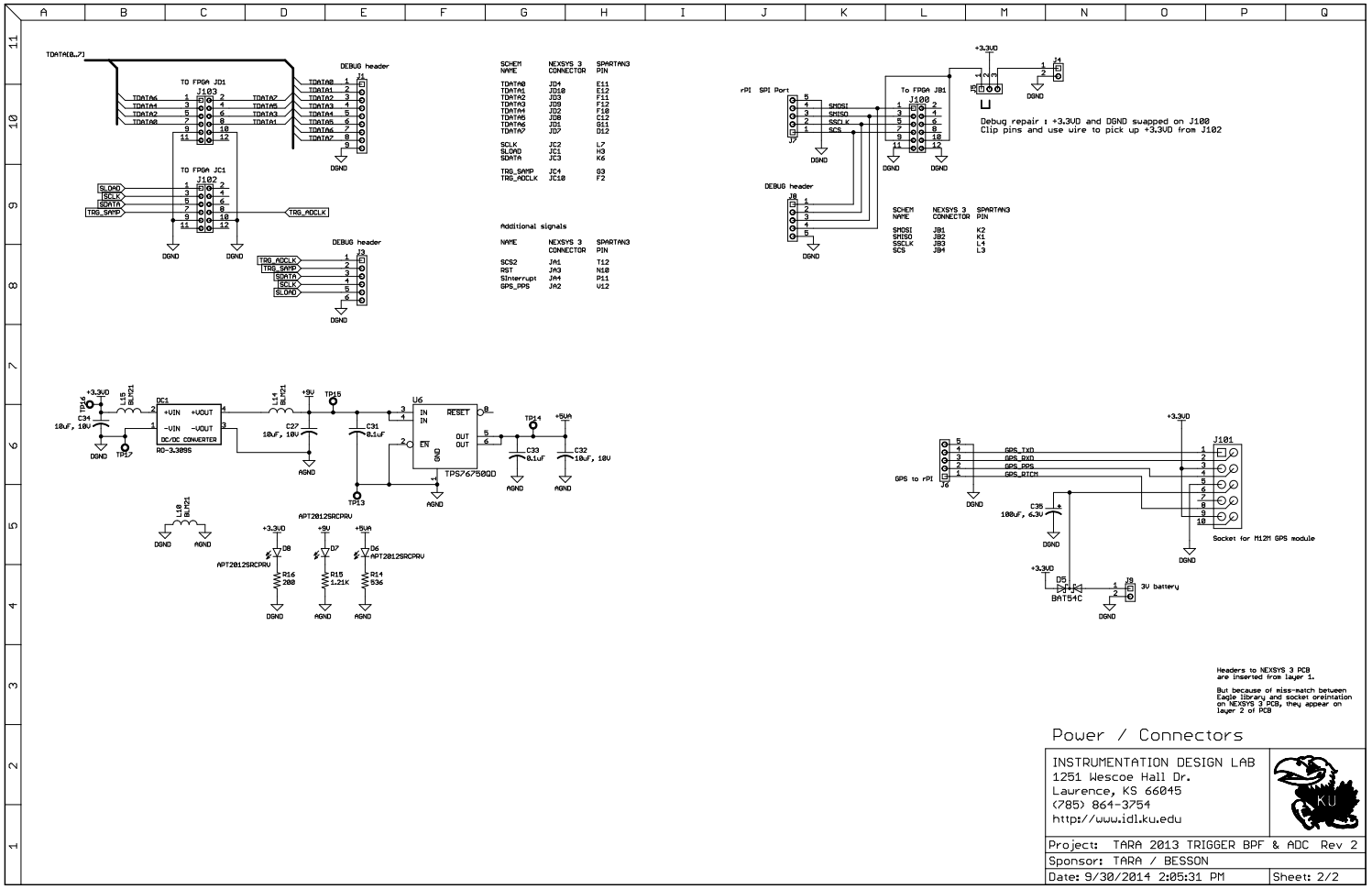

Fig. A.3 Details of the Triggering Board and connections to the FPGA and SBC. *Courtesy Rob Young, Instrumentation Design Lab, KU.*

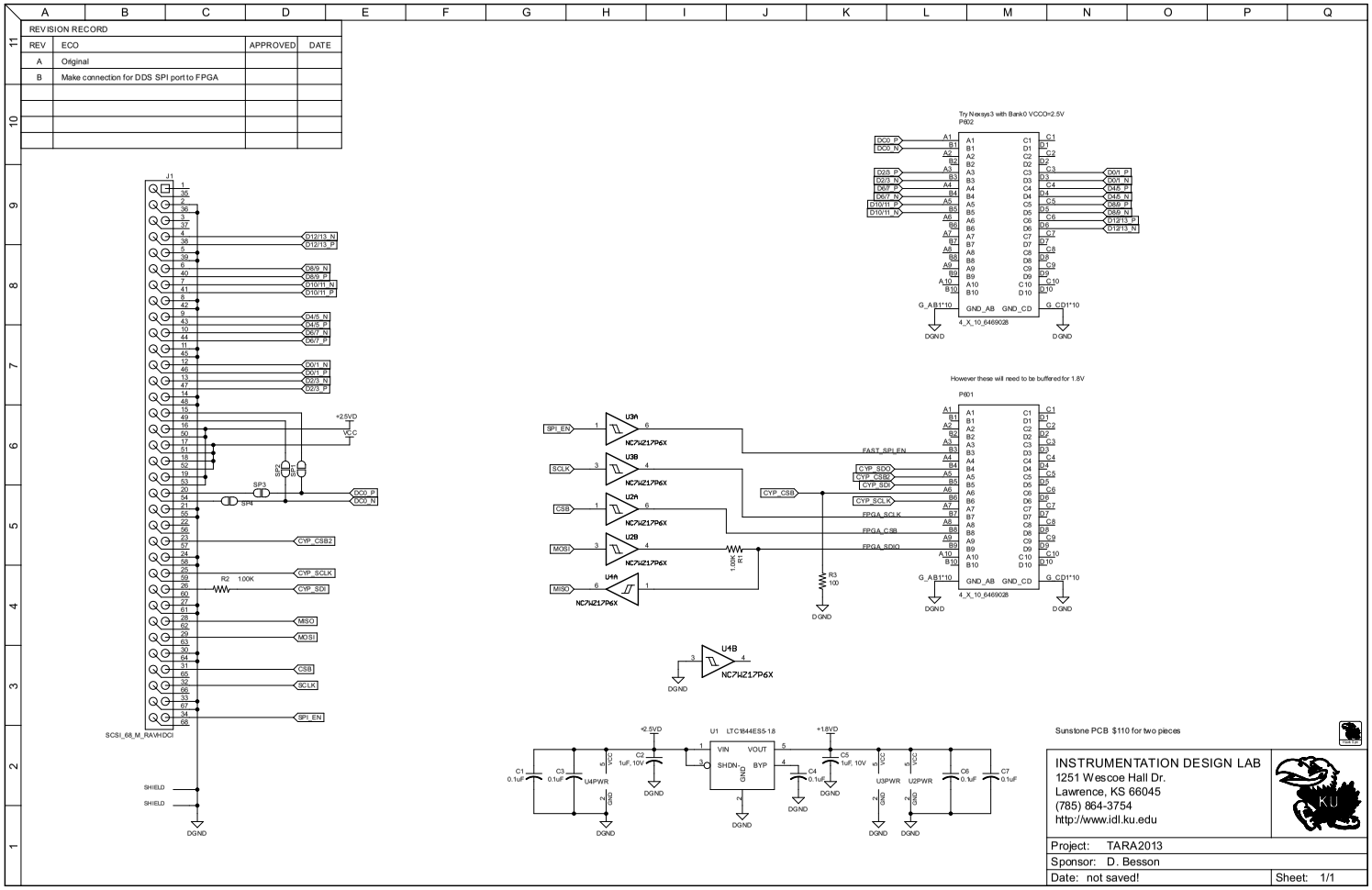

Fig. A.4 Adapter for the AD9634 Board and the FPGA. *Courtesy Rob Young, Instrumentation Design Lab, KU.*

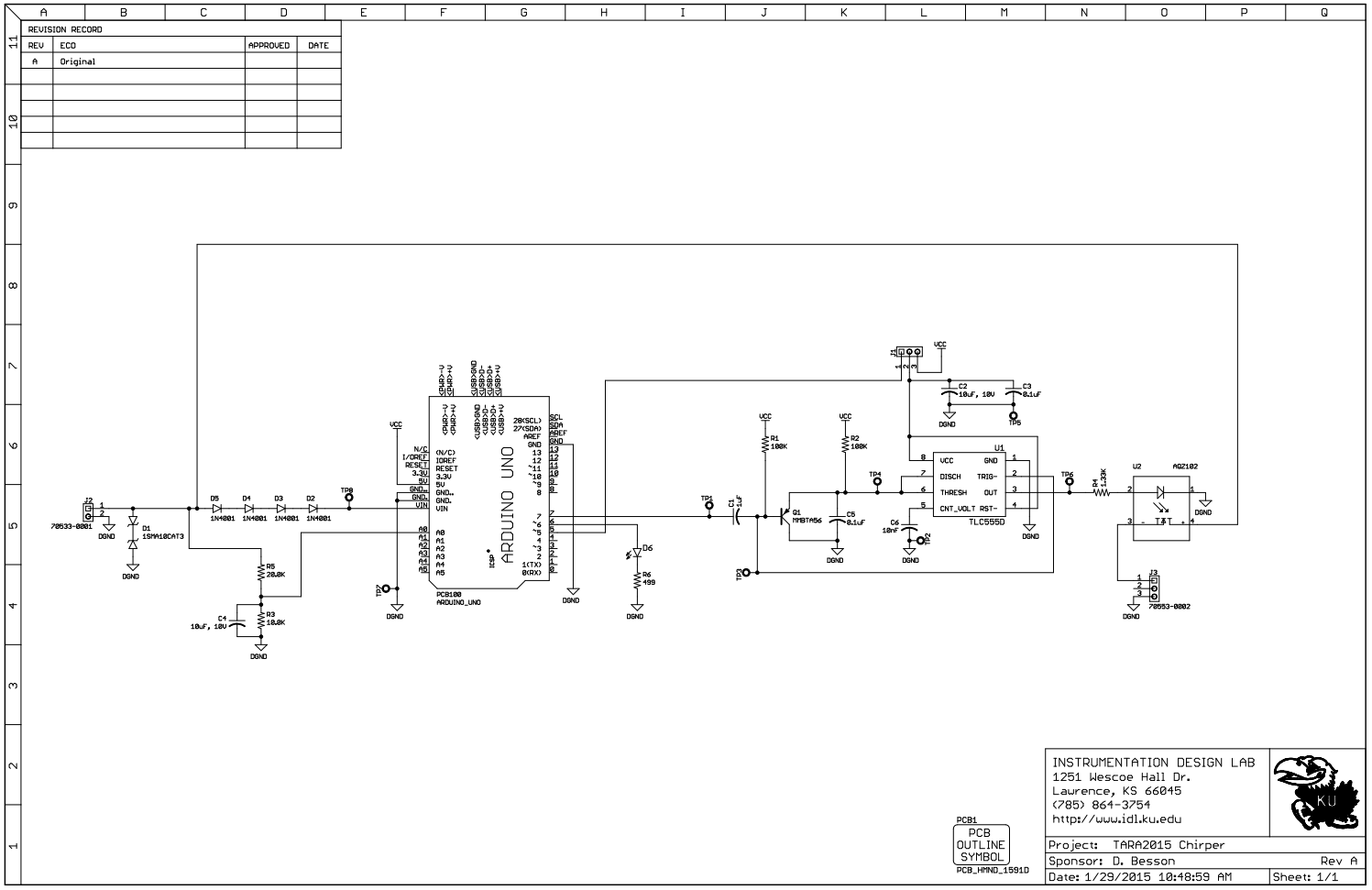

Fig. A.5 Control Circuit for the chirp generator. *Courtesy Rob Young, Instrumentation Design Lab, KU.*